

Rainfall variability in the Netherlands from radars, rain gauges, and disdrometers

Remco van de Beek

Thesis committee

Promotor

Prof. dr. ir. R. Uijlenhoet

Professor of Hydrology and Quantitative Water Management, Wageningen University

Co-promotor

Dr. ir. H. Leijnse

Senior researcher, Royal Netherlands Meteorological Institute, De Bilt

Other members

Prof. dr. A. Berne

EPF Lausanne, Switzerland

Prof. dr. ir. M.F.P. Bierkens

Utrecht University

Dr. I. Holleman

Radboud University Nijmegen

Prof. dr. A.A.M. Holtslag

Wageningen University

This research was conducted under the auspices of the Graduate School for Socio-Economic and Natural Sciences of the Environment (SENSE).

Rainfall variability in the Netherlands from radars, rain gauges, and disdrometers

Remco van de Beek

Thesis

submitted in fulfilment of the requirements for the degree of doctor
at Wageningen University

by the authority of the Rector Magnificus

Prof. dr. M.J. Kropff,

in the presence of the

Thesis Committee appointed by the Academic Board

to be defended in public

on Wednesday 12 June 2013

at 11 a.m. in the Aula.

van de Beek, C.Z.

Rainfall variability in the Netherlands from radars, rain gauges, and disdrometers. [Ph.D. thesis, Wageningen University, 2013, x+128 pp.]

In Dutch: Neerslagvariabiliteit in Nederland uit radars, regenmeters en disdrometers. [proefschrift, Wageningen Universiteit, 2013, x+128 pp.]

ISBN 978-94-6173-643-7

Abstract

Chapter 1. This thesis presents studies on the variability of precipitation in the Netherlands from datasets collected by radars, rain gauges and disdrometers. Accurate rainfall estimates are highly relevant in hydrology, meteorology and climatology as precipitation has a large impact on society. Precipitation has been studied extensively in the past, although it is impossible to describe all processes and behavior involved. This thesis attempts to add to the knowledge on precipitation. In the first chapter a short overview of rainfall variability at different scales is presented together with the most common instruments for measuring precipitation.

Chapter 2. The spatial variability of daily rainfall accumulations is studied. Ninety-day averaged semi-variograms are created based on a 30-year data set gathered by automatic stations operated by the Royal Netherlands Meteorological Institute (KNMI). This is complemented by a one-year dataset of 10 gauges within a 5 km radius around CESAR (Cabauw Experimental Site for Atmospheric Research) in the center of the Netherlands. It is shown that it is possible to derive an average semi-variogram that describes the climatology of daily precipitation for each day of the year.

Chapter 3. The study of chapter 2 is extended by investigating accumulation intervals shorter than daily scales. These are at 12, 8, 6, 4, 3, 2 and 1-hour accumulation intervals. It is shown that at shorter temporal scales the behavior of semi-variograms of precipitation still shows a clear seasonal trend. At hourly and two-hourly accumulation intervals the signal of the range becomes fairly constant during the summer due to the limited accumulation period, the frequent occurrence of convective precipitation, and measurement errors. This illustrates the lower limit of using cosine functions to describe variogram

parameters. By fitting a power-law function through the different cosine parameters it is possible to describe the semi-variance of precipitation at scales between 1 and 24 hours using a limited set of equations.

Chapter 4. Different sources of error affecting rainfall estimates by weather radar are identified. By focussing on precipitation near a C-band radar some of these sources are reduced, which allows to focus on a limited set of error sources. These are radar calibration, ground clutter, wet radome attenuation and variations in rain drop size distribution. An event that caused high precipitation amounts in a band along the center of the Netherlands and more than 50 mm near the radar between the 25th and the 27th of August 2010 is studied. Without any correction and by applying a standard Marshall-Palmer $Z - R$ relation the radar is found to underestimate by approximately 50% with respect to the rain gauge measurements. Using the sun for calibration a correction of 1 dB is applied. Clutter is corrected by subtracting a clear sky clutter map as this proves to provide better results than the standard doppler filter. Wet-radome attenuation is corrected by looking at the amount of attenuation at a known strong clutter pixel near the radar. Disdrometer data near the radar are used to derive accurate $Z - R$ relations specific to the precipitation of the event. These corrections combined provide very promising results with a slight overestimation of the quantitative precipitation estimates (QPE) from the radar by 5 to 8%.

Chapter 5. An extensive dataset of 195 precipitation events measured by an X-band radar (SOLIDAR) is used to study precipitation at a high spatial resolution of 120 m and a high temporal resolution of 16 s. This study shows the benefit of using such high resolution X-band radars over flat terrain. The errors in the radar measurements are first assessed and corrected as well as possible by considering different techniques. These errors are calibration, ground clutter and attenuation. Finally, five strongly different precipitation events are studied in detail to illustrate the strengths and weaknesses of the X-band weather radar.

Chapter 6 The variability and possible measurement methods of precipitation have been studied. It was shown that precipitation spatial and temporal variability has a clear statistical signal by analyzing variograms for different accumulation intervals. Weather radars were also shown to be able to give good estimates of precipitation at ground level as well as detailed information on the spatial variability. Some recommendations are given to perform follow up studies. For chapters 2 & 3 it is recommended to use a larger and more detailed dataset, which also incorporates Belgian and German data. This would allow the study of anisotropy in the semi-variograms as well as extending the analysis to accumulation times shorter than 1 hour and longer than 24 hours.

For chapter 4 it is recommended to study pixels located further away from the radar. While other error sources would become more pronounced it would be possible to study the applicability of the proposed corrections at longer ranges. Studying the wet-radome attenuation with several strong clutter pixels near the radar would allow the study of wind-effects on wet-radome attenuation, possibly allowing corrections using measurements of (Doppler) wind-speed and direction. Finally, in chapter 5 it is recommended to study the successor of SOLIDAR, IDRA, which is currently operational at CESAR. This radar is a polarimetric radar, allowing a more detailed study of precipitation together with the data from other instruments at this location and the C-band radar of KNMI, which is located close to this location at approximately 23 km.

Preface

As long as I can remember I have been interested in natural sciences. Going outside and enjoying nature and trying to understand processes driving our environment have always had a great attraction to me. During primary school and secondary school my interest kept growing due to the subjects geography and biology, but also due the many trips I made into nature to go birding with my father. With such a broad interest it was difficult to decide the focus of my study, but in the end I chose meteorology at Wageningen University. The processes driving weather and climate were very interesting to me and during this time I became ever more interested in remote sensing techniques. The idea of measuring weather at a local to global scale with different instruments was something that caught my attention. When Remko Uijlenhoet had a vacancy at the Hydrology and Quantitative Water Management Group at Wageningen University, where radar and rain gauge data were to be used in a study for a ground validation site for the upcoming Global Precipitation Measurement Mission (GPM), I was immediately very interested. The idea of working with ground based radar and the link with satellite measurements sparked my imagination. When I was selected for this project I was very happy to able to do this. In the course of the PhD study the topic did change due a delay in the installation of a new dual-pol X-band radar and also the uncertainty about the GPM project. The focus of the PhD moved from ground validation for satellite measurements to studying the space-time variability of precipitation in the Netherlands.

Many people have contributed in large and smaller ways to this thesis and I would like to thank everyone who made this thesis possible. First of all I would like to mention my promotor Remko Uijlenhoet. Remko, thank you for all the interesting discussions and suggestions over the years. You were also very patient when things sometimes did not go as quickly as hoped for! It has been a long road, but thanks to your support it was finally possible to give this

story a positive ending. Also my co-promotor Hidde Leijnse deserves a special thanks. When I joined the department you were finishing your PhD and during that time and since you have always been able to provide interesting views and helped me learn new things like radar theory and LaTeX. I would also like to give a special thanks to Paul Torfs. You have given much needed knowledge and suggestions for the statistical analysis of the different studies within this thesis. Especially the course on spatial statistics you prepared for the employees of the group using the book by Diggle and Ribeiro and applying the theory in chapters 2 and 3 was invaluable.

Others I would like to thank are Iwan Holleman, Hans Beekhuis and Aart Overeem from KNMI, who have contributed in many small ways to this thesis in the form of discussions and data you provided. These thanks also extend to Herman Russchenberg and Jordi Figueras i Ventura from TU Delft. Han Stricker also helped me greatly during the beginning of my PhD by providing interesting discussions. The rain gauge network that was started by Hanneke Schuurmans near CESAR was also invaluable for my thesis. My colleagues from the HWM and SEG groups who made my stay much more enjoyable obviously also deserve a special mention, like Shaakeel, Tessa, Ryan, Alexis, Ruud, Pieter, Anne, Claudia and everyone else! Also a special thanks to Daniel van Dijke and Robert Mureau from Meteo Consult for giving me the time to finish my PhD.

Finally a very special thanks to my wife Riejanne. While we only met during the later phase of my PhD thesis you have made it possible for me to finish it and gave me inspiration when I was struggling at times.

Remco van de Beek
Wageningen, 2013

Contents

1	Introduction	1
1.1	Background	1
1.1.1	Variability of precipitation	1
1.1.2	Instruments for measuring precipitation	3
1.1.3	Radars	6
1.1.4	Disdrometers	8
1.1.5	Microwave links	9
1.1.6	Satellite	10
1.2	Dutch precipitation research	11
1.3	Outline of the thesis	11
2	Climatology of daily rainfall semi-variance in The Netherlands	13
2.1	Summary	13
2.2	Introduction	14
2.3	Study area and data	15
2.3.1	KNMI station data	15
2.3.2	Dense rain gauge network	16
2.4	Theory	18
2.5	Methodology	20
2.6	Results and discussion	20
2.6.1	Climatological variation of rainfall	21
2.6.2	Variogram fitting on climatological data	22
2.6.3	Short range analysis	25
2.7	Conclusions and recommendations	27
3	Seasonal semi-variance of Dutch rainfall at hourly to daily scales	37
3.1	Summary	37

3.2	Introduction	38
3.3	Study area and data	39
3.4	Method	39
3.5	Results	43
3.5.1	Variation of rainfall at different temporal scales	43
3.5.2	Shape of the semi-variogram at different temporal scales	50
3.5.3	Decorrelation distance	55
3.6	Conclusions and recommendations	55
4	Close-range radar rainfall estimation and error analysis	57
4.1	Summary	57
4.2	Introduction	58
4.3	Instruments and data	60
4.4	Description of the rain event	62
4.5	Methodology and assessment	63
4.5.1	Calibration	63
4.5.2	Clutter correction	64
4.5.3	Wet radome attenuation	66
4.5.4	$Z - R$ relations	67
4.6	Discussion	71
4.7	Conclusions and recommendations	72
5	Performance of high-resolution X-band radar for rainfall measurement in The Netherlands	75
5.1	Summary	75
5.2	Introduction	76
5.3	Data and theory	78
5.3.1	Radar and gauge data	78
5.3.2	Rain rate estimation	80
5.4	Methodology and assessment	81
5.4.1	Radar calibration	81
5.4.2	Ground clutter correction	82
5.4.3	Derivation of $Z-R$ relations	86
5.4.4	Attenuation correction	89
5.5	Case studies	93
5.5.1	Event 1: light precipitation	93
5.5.2	Event 2: stratiform rainfall	96
5.5.3	Event 3: convective cells	96
5.5.4	Event 4: weak stratiform precipitation	99
5.5.5	Event 5: squall line	102
5.6	Summary and conclusions	104
6	Synthesis	107
6.1	Conclusion	107
6.2	Discussion and recommendations	109

CHAPTER 1

Introduction

1.1 Background

Knowledge of surface precipitation is important for society as inaccurate measurements and forecasts can mean risk to crops, livestock, property and even lives. Water quality and water shortage are always an issue for the quality of life, but also the effect of precipitation on floods and landslides is highly important. Therefore the study of precipitation is important in hydrology, meteorology and climatology. Traditionally rainfall has been measured with rain gauges, but more instruments have been developed this past century. Most notably these are ground-based radar, satellites, disdrometers and microwave links. This chapter gives some details on these systems, after a short discussion about the variability of precipitation and its importance, and concludes with an overview of the following chapters and research questions tackled in this thesis.

1.1.1 Variability of precipitation

Precipitation is highly variable, both in space and time. One can often notice that on a scale of only a few kilometers there has been precipitation at one location and none at another. This is also the case at both larger and smaller scales. Considering the Earth as a whole, the variability is clear when looking at the spatial distribution of precipitation. Fig. 1.1 shows this global rainfall climatology. It is clear that there are regions receiving more precipitation than others. Around the equator the highest precipitation amounts can be seen, associated with the Inter Tropical Convergence Zone (ITCZ). But also in the mid-latitude regions, where precipitation is mostly driven by frontal

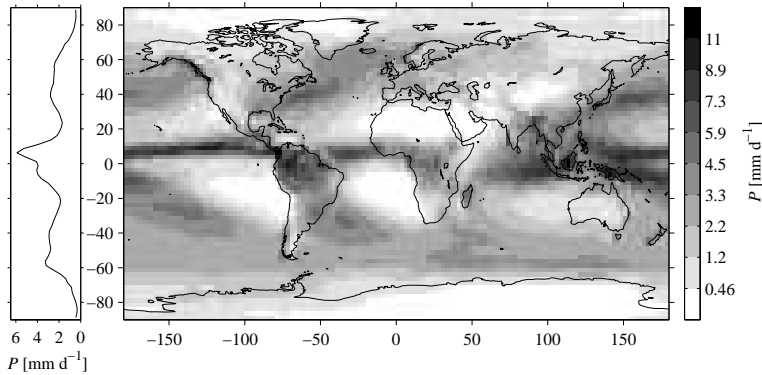


Figure 1.1: Global rainfall climatology for 1979-2008 measured by the Tropical Rainfall Measuring Mission (TRMM) with the inclusion of other sources (by the Global Precipitation Climatology Project (GPCP, v. 2.1)) (courtesy of Ryan Teuling).

systems, there are high precipitation accumulations. Dry areas are located in the subtropics where most deserts can be found, mostly due to subsidence in these regions. Arctic regions are also dry because the air is too cold to contain much water. At regional scales there are also clear differences between areas regarding precipitation amounts. Fig. 1.2 illustrates this variability for a case with very high precipitation in the eastern part of the Netherlands on 26 August 2010. While this event was very extreme for Dutch conditions, it is a good illustration of the large differences in precipitation that can occur over only short distances. Most people who live in areas where convective precipitation is common are familiar with this process as they will be aware that there are sometimes large amounts of precipitation at their homes, while only a few kilometers away it remained completely dry. This spatial variability at short ranges is also clear from Fig. 1.3 It is possible to go into even more detail and look at the distribution of individual droplets within the precipitation system. This distribution not only differs from rain event to rain event, but also within an event itself. Typical raindrop sizes are 0.1 to 6 mm, where most droplets are smaller than 3 mm. These variations of the drop size distribution (DSD) are important in accurate radar precipitation measurements and for understanding the physical processes behind precipitation formation and have been studied extensively (e.g. *Uijlenhoet, 1999; Berne and Uijlenhoet, 2005b*). While it is difficult to describe this variability at all spatial scales some authors have tried to capture it by using fractals (*Lovejoy and Schertzer, 1990*).

With current demands for water increasing due to more intensive agriculture and due to the growth of the human population, measuring and predicting (aspects of) these processes is very important. Accurate measurement of precipitation in terms of its intensity and location is important for both hydrolog-

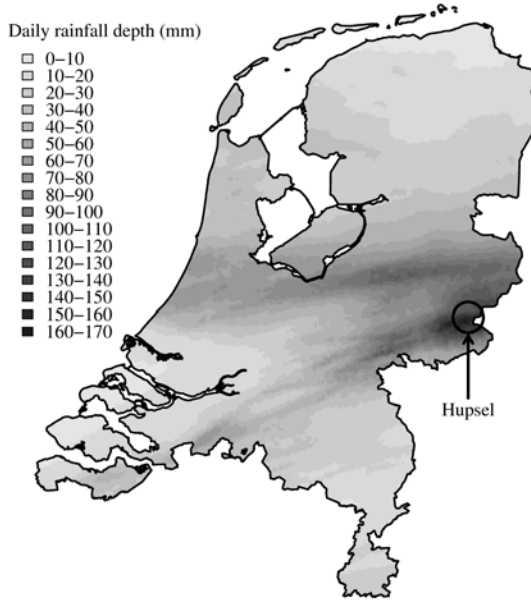


Figure 1.2: 24-Hour rain accumulation from a gauge-adjusted radar composite from 4:00 UTC on 26 August 2010 to 4:00 UTC on 27 August 2010, for The Netherlands from the KNMI C-band radar at De Bilt (courtesy of Aart Overeem).

ical research and operational water management, as well as weather prediction. Several instruments mentioned in this thesis are described shortly below.

1.1.2 Instruments for measuring precipitation

As mentioned before, precipitation is highly variable both in time and space. This makes it very challenging to study precipitation. Many instruments exist, from traditional rain gauges to more advanced systems like radar and disdrometers. The most important instruments are discussed below and the instruments that are used within this thesis are shown in Fig. 1.4)

Rain gauges

Rain gauges exist in different forms, but have generally been standardized into the shape of a cylinder that contains a funnel inside to concentrate precipitation that is collected. A cheap, but labor intensive, method of measuring the precipitation amount using a rain gauge is to manually measure the height of the collected water. This is usually done for gauges which only have to report infrequently, like once-a-day. In the Netherlands the Royal Netherlands Mete-

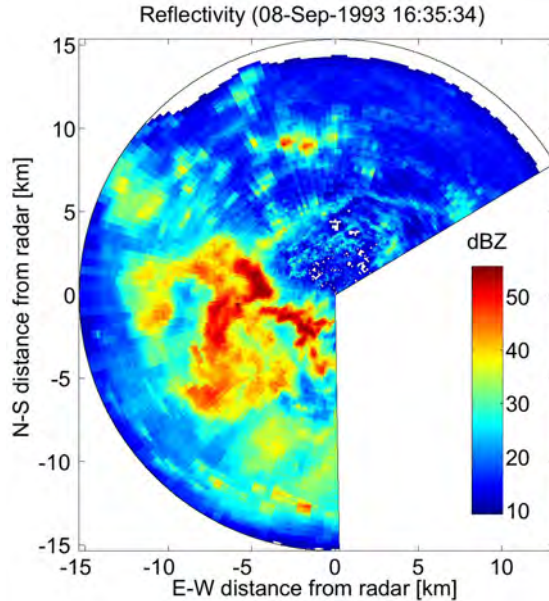


Figure 1.3: An example of the large spatial variability of rainfall measured by the X-band radar SOLIDAR on 8 September 1993 (courtesy of Remko Uijlenhoet).

orological Institute (KNMI) has around 325 volunteers that measure rainfall in this manner on a daily basis. Another method is the use of a tipping bucket. The funnel transports the collected water to a small bucket that tips at a certain weight. This allows measurements of precipitation at typical amounts of 0.2 mm. A disadvantage of this method is that a bucket might not be filled enough to tip during an event and will tip immediately at the start of a subsequent precipitation event. This can cause small errors in rainfall estimates. The most commonly used method at large automatic stations is to measure the precipitation with a float in the reservoir. This enables accurate measurements without the risk of inaccuracy that tipping-bucket gauges have. Many of these automatic gauges are also placed in a shallow pit to reduce the effect on wind on the precipitation being measured by the gauges. In the Netherlands KNMI operates a network of 32 automatic gauges besides the 325 manual gauges operated by volunteers.

The placement of a rain gauge is also important as objects in the vicinity can have an influence on the measured precipitation and effectively work as a (partial) barrier against rain. Especially in the prevailing wind direction no high objects like buildings and trees should be located near the rain gauge. In urban settings in particular it can be difficult to find a suitable location. Rain gauges do not only suffer from wind effects, but also from other sources of error

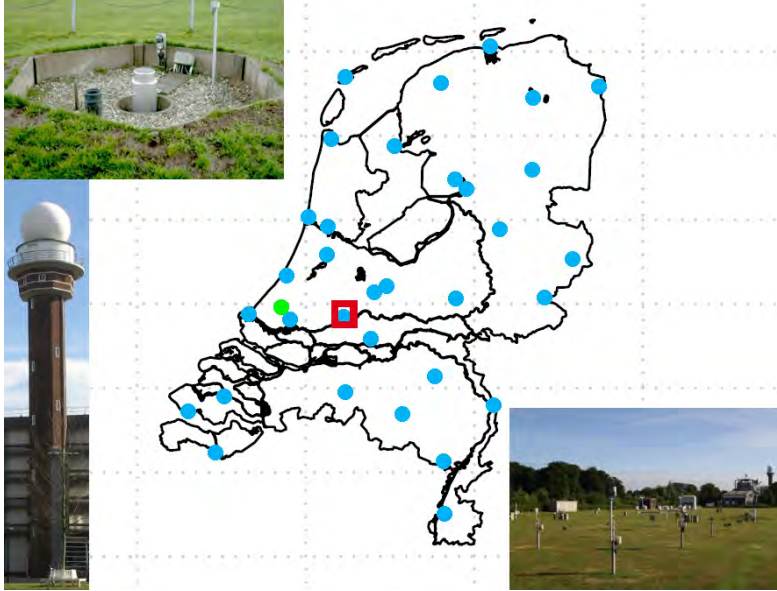


Figure 1.4: Locations of the instruments used in this study. The green dot near the coast is the location of the X-band radar SOLIDAR in Delft. The blue dots are locations of all automatic rain gauges operated by KNMI. The C-band radar and measurement field of KNMI are located at the lower-left blue dot of the two dots in the centre of the Netherlands at de Bilt (photos courtesy of KNMI). The red box just below indicates the locations of the dense rain gauge network.

(*Humphrey et al.*, 1997; *Calder and Kidd*, 1978; *Marsalek*, 1981; *Habib et al.*, 2001; *Ciach*, 2003; *Sieck et al.*, 2007). Dirt and insects can clog the funnel, which requires regular maintenance. Also frozen precipitation and rainfall near, or below, freezing level will cause delays in measured precipitation. While heated rain gauges solve this problem partially, it is more costly to operate such gauges and they still cannot completely remove the delay. Furthermore, heated gauges are likely to suffer more from evaporation losses. Also calibration errors can have a considerable influence and gauges should be well-calibrated. While a measurement by a rain gauge is not the absolute ground truth, it can be considered an accurate point measurement of precipitation. A network of rain gauges can give some spatial information of rainfall, but the required density would need to be very high in order to obtain detailed information on the spatial variability at small scales.



Figure 1.5: Example of an automatic rain gauge as operated by KNMI (courtesy of Aart Overeem).



Figure 1.6: Example of a manual rain gauge as used by the volunteer network of KNMI (courtesy of Aart Overeem).

1.1.3 Radars

While the theory to detect objects from electromagnetic waves has been around since the end of the 19th century, active interest in this subject came during the second world war (WWII). Radar (RADio Detection And Ranging) systems were developed at that time to detect incoming airplanes, but weather made the signal of airplanes more difficult to detect. After WWII

this led to research into using weather radar to detect precipitation. Nowadays these weather radars have become very important instruments in measuring the space-time variability of precipitation over large areas. Many densely populated parts of the world, like Europe and North America are covered with a dense network of weather radars. In the Netherlands KNMI operates 2 C-band radars, which cover the entire country and provide detailed information of precipitation at a 1 km resolution. The data these radars provide are used in many fields, like water management, weather research and hydrological and meteorological modeling. Other weather radars in the Netherlands are used for research purposes, like those operated by Delft University of Technology, IDRA (*Figueras i Ventura and Russchenberg, 2009*) and TARA (*Heijnen et al., 2000*).

The electromagnetic radiation is transmitted as pulses via the antenna of the weather radar. The wavelength of the transmitted signal is important for the detection of particles as the backscatter of the signal is dependent on the wavelength and the size of the droplets. Shorter wavelengths such as X-band (3 cm) have the advantage that the ratio of weather to clutter is higher than for longer wavelengths, and that such radar are often less expensive and smaller (shorter wavelengths require smaller antennas for similar beam widths). Longer wavelengths such as S-band (10 cm) and C-band (5-6 cm) suffer much less from attenuation (both wet radome and along the path) than shorter wavelengths. Hence, short-wavelength radars are generally used for local rainfall measurements, whereas long-wavelength radars are used for larger-scale rainfall monitoring.

Deriving precipitation from the received signal is complex as there are many possible sources of error (see Fig. 1.7). Attenuation along the path of the radar beam and attenuation due to precipitation on the radome itself can cause significant underestimation of precipitation when there is strong precipitation present. The radar signal can also hit non-meteorological objects (clutter), such as buildings and birds, but also the ground or mountains. Overshooting is another problem at longer ranges from the radar when the lowest scan level of the radar is at such a great height that precipitation below is not measured. This can lead to the false conclusion that no precipitation is present at that location. This problem as well as the problem of clutter is illustrated in Fig. 1.8, where the different scan levels are shown. The highest elevation will have the least problems with clutter due to hitting buildings as it scans high even close to the radar. The lower scan levels will have more problems with clutter and the lowest can be seen to move away from the earth with increasing range. As radar measures the reflectivity (Z) from a volume of air above the ground this has to be translated to precipitation at the ground (R). $Z - R$ relations are commonly used for this translation, where the Marshall-Palmer equation is the most common one. For more detail on radar theory see Chapters 2 and 3.

There are several techniques to address the problems mentioned above (e.g. *Hazenberg et al., 2011a*). The degree of success for these techniques is variable and often depends on the precipitation that is observed. Dual-polarization radars measure additional variables that can also be used to address some of

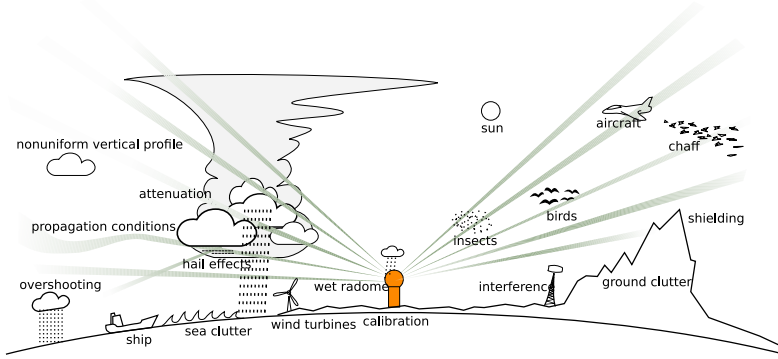


Figure 1.7: Illustration of error sources when measuring rainfall with radar (courtesy of Markus Peura, FMI).

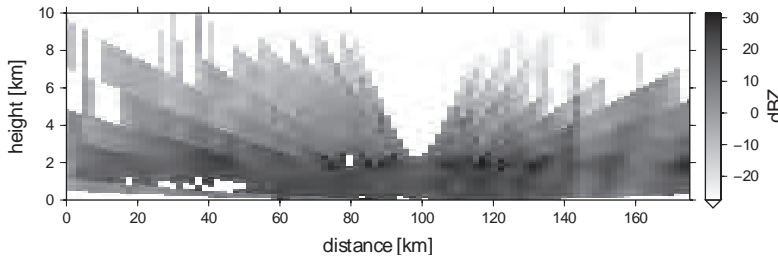


Figure 1.8: An example of the vertical reflectivity profile measured by a radar scanning at different elevations (courtesy of Pieter Hazenberg).

these issues. This will help increase the quality of radar rainfall estimates. Dual-polarization radars are currently being installed by operational weather services across Europe and North America.

1.1.4 Disdrometers

Disdrometers measure the drop size distribution and exist in many shapes. They can vary from systems measuring the impact of a drop on the instrument to systems that measure acoustically or with cameras and lasers which can also measure the fall velocities and shape of the droplets (e.g. *Joss and Waldvogel, 1977; Thurai and Bringi, 2005; Tokay et al., 2005; Minda and Tsuda, 2012*). The fact that these instruments measure drop size distributions makes them ideal for validation of radar reflectivity measurements and derivation of suitable $Z - R$ relations. A problem with these systems is that there can be large differences between the DSDs measured by different instruments at the same location. These are caused by differences in measuring techniques, but also in



Figure 1.9: A 2-D video disdrometer (middle, with processing unit and sonic anemometer, left) and an optical disdrometer (right) at Cabauw, The Netherlands (courtesy of Hidde Leijnse).

sampling uncertainty as only small volumes tend to be measured. TU Delft is investigating a low-cost acoustic disdrometer that listens to falling droplets. Especially for urban situations these might be ideal as a network of low-cost instruments which might offer great detail on precipitation in the area, especially if combined with a radar. More information on optical disdrometers can be found in Chapter 4.

1.1.5 Microwave links

Using microwave scintillometers to measure precipitation is also interesting as these instruments are usually employed to measure evapotranspiration. By analyzing path-integrated attenuation it is also possible to use these instruments to measure rainfall (*Leijnse et al.*, 2007b). Recently interest in the use of commercial microwave links has grown as they are widely distributed for cell-phone use (*Messer et al.*, 2006; *Leijnse et al.*, 2007a). Attenuation along the path is considered to be noise by operators of these links, but this “noise” can be used to measure precipitation in a similar manner as using the “noise” in scintillometry. With many links in densely populated areas of the world this is very interesting, especially in areas where there are limited funds available for rain gauge networks or radars. These instruments can also be very useful for catchment hydrology as they offer a path-averaged precipitation value instead of a rain gauge, which only provides information at a single location. An example of about 2000 commercial microwave links in the Netherlands is shown in Fig. 1.10. Microwave links are not discussed in this manuscript, but as they offer a complementary method for measuring precipitation they are mentioned in this introduction.

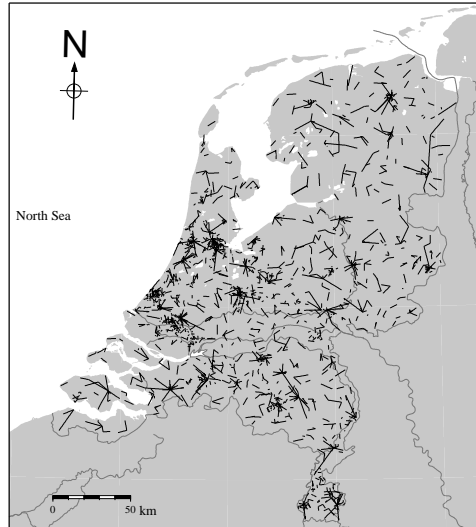


Figure 1.10: Part of the cellular communication microwave link network of one commercial provider in The Netherlands (courtesy of Aart Overeem).

1.1.6 Satellite

Large-scale precipitation is also studied with satellite-based instruments. While images from space lack the detail and also usually have larger quantitative errors than ground-based instruments they do provide insight on synoptic scale precipitation and are a way of getting an estimate of precipitation in areas too remote for ground-based instruments. Many satellites offer insight in the clouds and precipitation on earth by having passive radiometers and active radars on board. One of these satellites is MeteoSat with the SEVIRI instrument. MeteoSat has provided images of a large part of Europe and Africa since 1977 and provides images every 15 minutes, similar to GOES for America. During this time the satellite has been replaced by upgraded versions. While it is difficult to derive accurate precipitation from MeteoSat images there have been many studies (e.g. *Roebeling and Holleman, 2009; Chadwick et al., 2010; Kuhnlein et al., 2010*). The Tropical Rainfall Measurement Mission (TRMM) is designed to provide a 3-dimensional image of precipitation of the Earth between 35°S to 35°N . An example of the great detail that can be achieved on a global scale is shown in Fig. 1.11. Unlike MeteoSat the satellite is not geostationary and provides only high resolution data along its path with a return time of several days (*Iguchi et al., 2000; Huffman et al., 2007; Arias-Hidalgo et al., 2012*). The Global Precipitation Measurement mission is set to be launched in 2014 and is the successor of TRMM (*Kobayashi and Iguchi, 2003; Bidwell et al., 2004; Rose and Chandrasekar, 2006*).

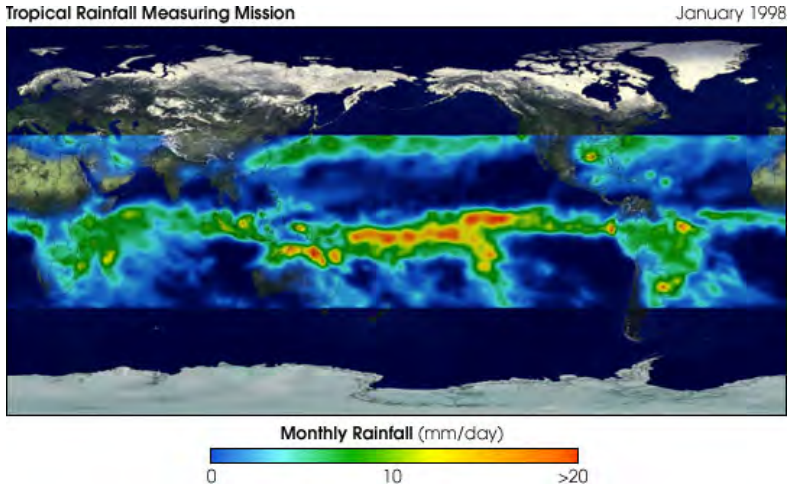


Figure 1.11: Average rainfall of January 1998 gathered by TRMM (source: <http://earthobservatory.nasa.gov/IOTD/view.php?id=1017>)

1.2 Dutch precipitation research

In the Netherlands there is a certain tradition of theses dealing with different aspects of precipitation. At Wageningen University theses on this topic can be found as early as the 1960s, for example by *van Montfort* (1966) and later by *Buishand* (1977); *Witter* (1984); *de Lima* (1998); *Uijlenhoet* (1999). This tradition has continued in the new millennium with *Leijnse* (2007); *Overeem* (2009) and work by *Hazenberg et al.* (2011a,b). Hydrological implications of the effect of precipitation variability across scales has been studied at Utrecht University by *Schuurmans*. In Delft precipitation has also been studied with radars since the last decade of the previous millennium (e.g. *Klaasen*, 1989; *Russchenberg*, 1992; *Unal*, 2009; *Figueroa i Ventura and Russchenberg*, 2009).

1.3 Outline of the thesis

Even though there is a long tradition of precipitation research there still exist many questions concerning precipitation. Based on the challenges mentioned above this thesis will focus on the spatial and temporal variability of rainfall rather than the meteorological processes. Several questions that have not been answered by previous studies are therefore:

- Is it possible to characterize rainfall variability in the Netherlands, based on limited rain gauge data?
- What is the best possible accuracy attainable with radar?

- Does high-resolution X-band radar offer additional insight in precipitation over more traditional rain gauge networks and operational radars?

These questions are investigated in the following chapters of this thesis. In Chapter 2 the daily behaviour of rainfall is studied by looking at the 90-day moving average semi-variance using rain gauge data from the automatic KNMI stations as well as a dense gauge network around the measurement site CESAR (Cabauw Experimental Site for Atmospheric Research, see e.g. *Leijnse et al.*, 2010). Chapter 3 expands on this study by looking at accumulation times between 1 and 24 hours. This makes it possible to describe the semi-variance of rainfall in the Netherlands with only a few parameters at these time accumulations. Rainfall in the Netherlands is studied with radar and compared to disdrometer and rain gauge data in Chapter 4. In Chapter 5, a large dataset with 195 rainfall events measured with a high resolution X-band radar is studied. Finally, in Section 6 the conclusions are presented together with an outlook for future studies.

CHAPTER 2

Climatology of daily rainfall semi-variance in The Netherlands

2.1 Summary

Rain gauges can offer high quality rainfall measurements at their locations. Networks of rain gauges can offer better insight into the space-time variability of rainfall, but they tend to be too widely spaced for accurate estimates between points. While remote sensing systems, such as radars and networks of microwave links, can offer good insight in the spatial variability of rainfall they tend to have more problems in identifying the correct rain amounts at the ground. A way to estimate the variability of rainfall between gauge points is to interpolate between them using fitted variograms. If a dense rain gauge network is lacking it is difficult to estimate variograms accurately. In this chapter a 30-year dataset of daily rain accumulations gathered at 29 automatic weather stations operated by KNMI (Royal Netherlands Meteorological Institute) and a one-year dataset of 10 gauges in a network with a radius of 5 km around CESAR (Cabauw Experimental Site for Atmospheric Research) are employed to estimate variograms. Fitted variogram parameters are shown to vary according to season, following simple cosine functions. Semi-variances at short ranges during winter and spring tend to be underestimated, but semi-variances during summer and autumn are well predicted.

This chapter has been published with minor modifications as: van de Beek, C. Z., Leijnse, Torfs, P. J. J. F. and Uijlenhoet, R. , 2011. *Climatology of daily rainfall semivariance in The Netherlands*, Hydrol. Earth Sys. Sci., 15, 171-183

2.2 Introduction

Rainfall is highly variable both in time and space and accurate measurements are important in hydrology (*Bell and Moore*, 2000; *Arnaud et al.*, 2002; *Tetzlaff and Uhlenbrook*, 2005). Especially in urban settings where the response time of runoff is typically very short these accurate estimates are needed (*Smith et al.*, 2002, 2005; *Vaes et al.*, 2005; *Olsson et al.*, 2009; *Villarini et al.*, 2010). There are several instruments available to measure these rainfall distributions. The traditional instrument to measure rainfall is the rain gauge. While rain gauges measure rain accurately and continuously at a point, they offer little information on rainfall between gauges. Rain gauges themselves are not fully accurate and are influenced by factors such as calibration accuracy, wind effects and sampling uncertainty, which also limits the accuracy for sampling intervals smaller than 10 minutes (*Humphrey et al.*, 1997; *Calder and Kidd*, 1978; *Marsalek*, 1981; *Habib et al.*, 2001; *Ciach*, 2003; *Sieck et al.*, 2007). Frozen precipitation like snow and hail also offers a problem as these hydro-meteors do not melt immediately and therefore will result in a lower precipitation rate estimate over a longer period than actually occurred.

Other measurements with instruments like microwave links (*Leijnse et al.*, 2007b) and disdrometers (*Joss and Waldvogel*, 1977) offer alternative methods for measuring rainfall, but are more expensive and do not measure the spatial variability for an entire catchment area. Weather radars are able to measure spatial variability of rainfall at different spatial resolutions depending on wavelength and antenna size and measure at typical intervals of 5 to 15 minutes for ground based systems and with an interval of 3 hours or more for satellites (e.g. *Uijlenhoet*, 2008). Quantifying these rainrate measurements is non-trivial as the reflected signal of a volume in the air has to be transformed into an accurate estimate of rainfall at the ground. It requires knowledge of the microstructure and the vertical variation of rainfall, which is generally not available. Furthermore, a good calibration of the radar system itself and correction of factors such as attenuation and ground clutter are important for accurate radar rainfall estimation (*Hitschfeld and Bordan*, 1954; *Marshall et al.*, 1955; *Marzoug and Amayenc*, 1994; *Delrieu et al.*, 1999; *Krajewski and Smith*, 2002; *Villarini and Krajewski*, 2010; *van de Beek et al.*, 2010).

There are many examples of studies into the optimal sampling density and interval for these instruments (*Villarini et al.*, 2008; *Villarini and Krajewski*, 2008; *Nour et al.*, 2006; *Cheng et al.*, 2008). The variability of rainfall both in space and time has also been studied extensively, mainly using rain gauge and radar data (*Ensor and Scott*, 2008; *Krajewski et al.*, 2000; *Berne et al.*, 2004c; *Knox and Anagnostou*, 2009; *Habib et al.*, 2009). Rainfall variability has also been investigated in the Netherlands (*Buishand and Velds*, 1980; *Witter*, 1984; *Schuurmans et al.*, 2007), where focus in the last few years has been on extremes for water management and possible changes in climate. *Buishand et al.* (2008), using 30 years of data of 32 rainguages in the province of Noord Holland, The Netherlands investigate the amount of daily rainfall for an extreme once-in-100-years event. This work is continued by *Buishand et al.*

(2009), using the daily rain sums of 141 stations in the Netherlands between 1951 and 2005 to find the regional rainfall differences using generalized extreme value distributions (GEV). They identify 4 different precipitation regimes in the Netherlands. *Overeem et al.* (2009) use the rainfall data of 12 stations to create a 514 year record. A GEV is fitted to this data for durations between 1 and 24 hours and used to construct depth-duration-frequency (DDF) curves. Using a bootstrap method the uncertainty of these DDFs is estimated.

The goal of this study is to produce a simple equation to estimate the daily rainfall variogram as a function of the time of year. This allows the creation of areal rainfall maps for hydrological modeling purposes at smaller catchment scales where often only one or very few gauges are available to estimate rainfall amount and distribution. For hydrological modeling variograms are often used in the creation of rainfall maps by interpolating sparse rain gauge data using kriging (*Creutin et al.*, 1986; *Krajewski*, 1987; *Papamichail and Metaxa*, 1996; *Nour et al.*, 2006; *Haberlandt*, 2007; *Kirstetter et al.*, 2010). Kriging of the data has the advantage that the associated variance for each estimated location can be obtained. The associated uncertainty of the estimated areal rainfall found from the kriging variance can be used as input in a hydrological model and offers a better understanding of the upper and lower margins of the estimated discharge. The estimated variograms also offer a way of generating random fields for research purposes (*Cressie*, 1993; *Diggle and Ribeiro Jr.*, 2007; *Li et al.*, 2008).

The data used in this study are 30 years of daily rainfall data as well as one year of high-resolution gauge network data. In Section 2.3 the data and study area are described. The theory is described in Section 2.4. Section 2.5 concerns the methods used to estimate the seasonal variograms and Section 2.6 describes the results. Finally Section 2.7 summarizes the study and offers recommendations for future work.

2.3 Study area and data

In the Netherlands the rain maximum typically occurs around November with a rain sum between 60 and 100 mm during this month. The minimum occurs around April with around 40-60 mm. The yearly rain sum lies around 800 mm. While the Netherlands is fairly small with a land surface area of less than 34.000 km² differences in yearly rainfall between locations can be up to 200 mm (source KNMI¹).

2.3.1 KNMI station data

Data from 33 automatic KNMI stations between January 1, 1979 and February 15, 2009 were considered for this study (top panel Fig. 2.1). They offer a good way to evaluate larger scale variation of rainfall. Their distribution is shown in Fig. 2.2, with an average inter-gauge distance of 120 km. One-day

¹<http://www.knmi.nl/klimatologie/normalen1971-2000/index.html>

rainfall accumulations are used for the climatological study in this chapter. The hourly accumulations are available with a volumetric resolution of 0.1 mm. Nonzero rainfall accumulations below 0.05 mm have been set to 0.05 mm in this dataset to indicate nonzero rain (this would otherwise be rounded to zero). While rounding these measured data to 0.05 mm might lead to some slight overestimations this was chosen to be preferable by the authors as now all rainfall is included. Data of the KNMI volunteer network with 329 locations of daily rainfall accumulations were also considered. Because of errors introduced by observers (*Daly et al.*, 2007), causing high variance for data pairs located close to each other, it was decided that this dataset was not suitable for this study. The accuracy of these gauges is described in *Wauben* (2006) and the history of each individual gauge can be found at the KNMI site at <http://www.knmi.nl/klimatologie/metadata>.

2.3.2 Dense rain gauge network

The second dataset was collected using a dense network of 30 tipping-bucket rain gauges around CESAR (Cabauw Experimental Site for Atmospheric Research) which were jointly operated by University of Utrecht and Wageningen University (*Schuurmans et al.*, 2007; *Leijnse et al.*, 2010). The gauges had a volumetric resolution of 0.2 mm and a time resolution of 0.5 sec and were placed within a 5 km radius around CESAR (bottom panel of Fig. 2.1). Of this dataset 10 gauges were selected as they operated well and continuously between March 2004 and March 2005. The data were converted to one day accumulations for this study by estimating the rain rate from the number of tips per day. Periods of 6 hours or longer without a tip were assumed to be dry. The resulting data are used for estimating the short range rainfall variation for the detailed one-year study.

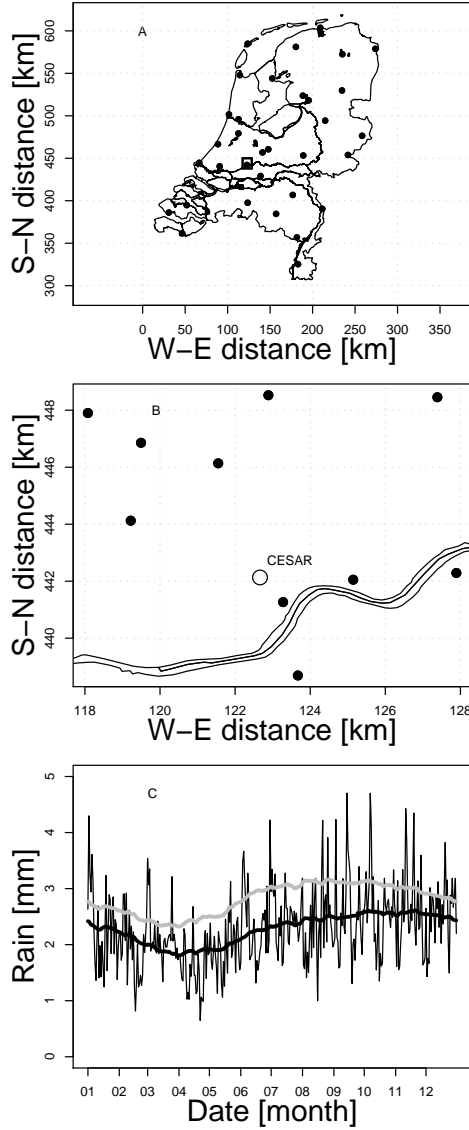


Figure 2.1: A) station locations of the 33 KNMI measurement stations. The square near the centre of the Netherlands is shown in B) and is a detail of the 10 selected gauges of the dense gauge network. C) The 30-year mean rainfall in the Netherlands, where the thin black line is the average rainfall for each day, the thick black line the 90-day moving average and the thick grey line the 90-day moving average for only rainfall events (i.e. with dry days excluded).

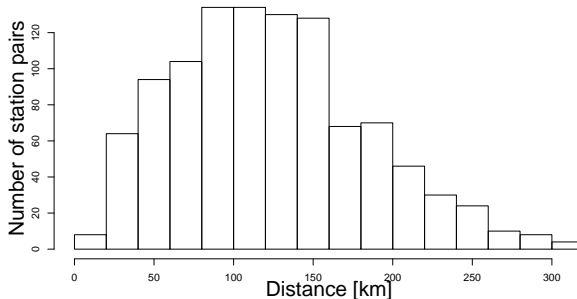


Figure 2.2: Histogram of the distance between the KNMI automatic rain gauges.

2.4 Theory

A standard method for evaluating rainfall variability is to estimate variograms. Assuming stationarity and isotropy of the rainfall field, which is not an unreasonable assumption on the daily scale, the experimental omnidirectional semi-variogram can be found by taking half the average of the squared difference between data pairs within the same distance interval (*Cressie*, 1993):

$$\hat{\gamma}(|h|) = \frac{1}{2n(|h|)} \sum_{i=1}^{n(|h|)} (z(x_i + h) - z(x_i))^2, \quad (2.1)$$

where x_i is the location of gauge i and $x_i + h$ the locations at distance h from location x_i . For a dataset with measurements at n locations this means there are $n(n-1)/2$ data pairs with different separation distances, i.e. 528 pairs for the nationwide network and 45 pairs for the dense network. Rainfall anisotropy has been studied extensively in the past (*Guillot and Lebel*, 1999; *Velasco-Forero et al.*, 2009; *Schleiss et al.*, 2009). While anisotropy is always an issue with rainfall the effects are reduced by the averaging over 90 days. Another reason is that we want to keep the number of parameters as low as possible to maintain a simple model. If too many parameters are included they might become interdependent and a sound statistical analysis would become highly complicated. For a sound analysis of possible anisotropy and stationarity a more extensive dataset would be needed and inclusion from the Belgian and German network might offer interesting future research.

As the empirical variogram values will not offer values for each distance h one of several possible models has to be fitted to estimate these semi-variances. While many types, like exponential, Gaussian or logarithmic exist (*Diggle and Ribeiro Jr.*, 2007) it was decided to take a simple spherical variogram as this model adequately fits the variogram values with only a few parameters, unlike

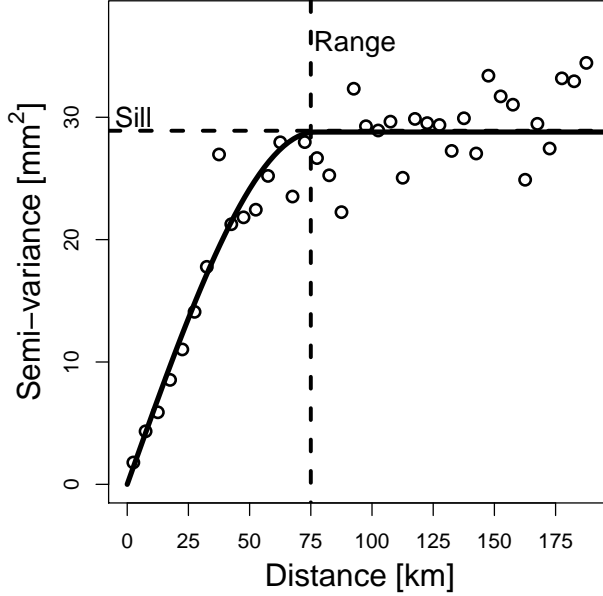


Figure 2.3: Example of variogram parameters based on actual data, where the circles represent the binned semi-variance. The solid line is the fitted spherical variogram. The horizontal dashed line is the sill and the vertical dashed line is the range.

more complex models where the parameters can become highly complicated to interpret (*Berne et al.*, 2004c):

$$\gamma(h) = \begin{cases} c_0 + c_1 \left(\frac{3}{2} \frac{h}{a} - \frac{1}{2} \left(\frac{h}{a} \right)^3 \right) & \text{if } h \leq a \\ c_0 + c_1 & \text{if } h > a \end{cases} \quad (2.2)$$

Here c_0 is the nugget (the variance at zero distance), c_1 is the sill (the maximum value of the fitted semi-variance function) and a is the range (distance at which data pairs are completely decorrelated). See Figure 2.3 for an illustration.

As the semi-variance for two gauges from the dense gauge network at a distance of 8 m using a 90-day moving window was found to be only 0.035 mm² with a standard deviation (σ) of 0.018 mm², the nugget was assumed negligible and therefore Equation (2.2) reduces to:

$$\gamma(h) = \begin{cases} c_1 \left(\frac{3}{2} \frac{h}{a} - \frac{1}{2} \left(\frac{h}{a} \right)^3 \right) & \text{if } h \leq a \\ c_1 & \text{if } h > a \end{cases} \quad (2.3)$$

which only depends on the sill and range. The spherical variogram near zero distance is approximately linear. This means that for $h \ll a$ the equation can

be reduced to:

$$\gamma(h) = \frac{3}{2} \frac{c_1}{a} h \quad (2.4)$$

2.5 Methodology

The data are analyzed by estimating the daily omnidirectional semi-variance and subsequently averaging these over 90-days using the fitting method described in Chapter 5 of *Diggle and Ribeiro Jr. (2007)*. The weights are equal for each day and the day of interest is taken at the center of the period. To find a signal in the fitted variogram parameters it is necessary to average over an optimal range of days to avoid the noise of day-to-day variations. It was decided to average over 90 days to avoid shorter periods without rainfall, e.g. early spring 2007 with a total of 45 dry days. In addition, as 90 days is the length of a season it is an appropriate length for the purpose of this study.

Even though other weights like a Gaussian or triangular distribution might be used, to keep the fit simple, the window has equal weights for the entire 90-day period, which is in line with the idea of this study to create a simple method of modeling daily variograms. The effect of using triangular weights has been tested and was found to have very little effect. An averaging window of 60 days was also tested and was found to differ very little from the 90-day averaging window.

Finally, the data are binned in distance classes with a 5 km class width for both faster fitting of the spherical variogram and easier interpretation of the figures. With the furthest gauge pair in the dataset at 315 km it was decided to set the maximum range at 200 km for fitting the spherical variogram. Cases where the range is apparently larger than this maximum distance occur mostly around November, when the variogram data tends to be nearly linear over the full domain from 0 to 315 km. In cases like this, where $|h|$ is always smaller than the estimated range of the variogram, Eq. 4 becomes valid.

In Section 2.6 the climatological data will be assessed to find the daily trend in the sill and range. To fit a cosine function to this trend spectral analysis is applied. A simple time-series of a cosine function could be expressed as:

$$x_t = x_0 + A \cos(2\pi f(t - t_0)) \quad (2.5)$$

Here x_0 is the offset, A is the amplitude, f is the frequency and t_0 defines the start day of the cosine function (*Shumway and Stoffer, 2006*).

2.6 Results and discussion

With rainfall being highly variable both in time and space it is difficult to model the process accurately. In this section it will be shown that there are stable factors in rainfall variability, which can be used for hydrological purposes. The climatological analysis is applied to the KNMI gauges for the 30-year period between January 1979 and February 2009.

Table 2.1: Parameters of the fitted cosine functions for mean, standard deviation (σ) and coefficient of variation (CV) of the daily rain sums of the KNMI stations between February 15, 1979 and February 15, 2009 using a 90 day moving averaging window.

	$1/f$	A	t_0	x_0
mean	365	0.30	109	2.8
σ	365	0.69	68	2.1
CV	365	0.48	54	1.7

2.6.1 Climatological variation of rainfall

While there can be a strong day-to-day fluctuation of rain, a seasonal trend can be found. This is shown in Fig. 2.4, where the variation of the daily rain accumulation is assessed by taking the average of the data from the 33 KNMI stations and using a 90-day averaging window. In Fig. 2.4a the mean rain sum can be seen to fluctuate strongly and it is difficult to find a clear trend in the data. While the seasonal signal is the strongest there are very strong deviations from the estimated cosine function and therefore the mean rain sum is difficult to capture in a single function.

For the standard deviation (σ) of rainfall between the stations the signal already becomes much clearer (see Fig. 2.4b). While there are still departures of more than a factor of two from the fitted cosine the seasonality is clear. This can be explained by the more convective type of rain during summer with more localized events and the more common stratiform rain type during winter months. The rainfall climate of the Netherlands is such that total rainfall amounts are approximately constant throughout the year. However, the spatial variation is governed by storm type, which does show clear temporal variation in the Netherlands. Finally, a good way to express the relative variation of rainfall is by dividing the standard deviation by the mean to find the coefficient of variation (see Fig. 2.4c). The fitted simple cosine function can be seen to follow the seasonal variation in the coefficient of variation (CV) very closely. The values found for the fitted functions for mean, σ and CV can be found in Table 2.1 with t expressed as Day of Year (DOY) and x_0 the mean of the data.

The amount of stations with no rainfall measured also has an impact on the statistical distribution of the data. In Fig. 2.4d the fraction of stations without rainfall is shown, again using a 90-day moving average. The lows in this figure coincide with the lows in the σ , as could be expected with lower values of σ corresponding to more widespread rain, leading to less zeros present in the data. Fig. 2.4e shows the 90-day moving mean with dry locations removed (as shown in Fig. 2.4a) divided by the moving mean including the stations with zero rainfall. Again the peaks can be found during the summer and lows during winter. With the more localized rainfall occurring during summer the effect of removing the zero rainfall locations from the data is larger during this season

than during winter. Due to this effect the mean during summer can be up to 1.8 times larger if no zeros are included, while the ratio during winter is fairly constant (around 1.2).

2.6.2 Variogram fitting on climatological data

With spherical variograms fitted to the 30-year climatological rain data as described in Section 2.4 it is possible to find the seasonal variation of sill and range. We will also investigate the root mean square errors between the 90-day averaged variograms and the corresponding fit. Again frequency analysis is applied to find the best fit for the cosine function to describe the seasonal variation using the rain data with dry locations excluded. This was also tested with dry locations included. While this gave slightly different values this effect was found to be negligible.

Seasonal range

As mentioned before, rainfall is strongly seasonal and this also applies to the range of the fitted variograms. The range reaches a minimum in July and a maximum in January (see Fig. 2.5a). Again this can be attributed to the prevailing rain types during winter and summer. During summer the rain tends to be convective, which means that the correlation quickly decreases with the distance between two points. In winter this changes with stratiform rain, where rain rates can be similar over long distances. There are cases where the fitted range is far beyond 200 km and thus even beyond the furthest data pair at 315 km and therefore not reliable. This causes the fitted variogram to be nearly linear up to 200 km distance, in line with what could be expected from Eq. 4. This is caused by the large-scale stratiform precipitation that is common during this time of the year. As the range at these times is far beyond the furthest data pair, because of a linear instead of a spherical relation, the estimation of the range and sill would add little meaning and therefore the maximum range was set to 300 km.

A square-root square-root (sqrt-sqrt) transform was applied to the fitted range values. There are numerous other possible transforms like logarithmic, logistic and Box-Cox (*Shumway and Stoffer, 2006; Hartwig and Dearing, 1979*), but the sqrt-sqrt transform was chosen to try to reduce the influence of extreme values for a better fit of the cosine function as well as making the resulting distribution more symmetrical (see Figs. 2.6a and b). The cutoff of the histograms at the right hand side is caused by the maximum range of 300 km. The resulting fit can be modeled as:

$$x_t = [x_0 + A \cos(2\pi f(t - t_0))]^4 \quad (2.6)$$

This model is the same as Equation (2.5) but transformed with a power 4 (the inverse sqrt-sqrt transform). This transform has only a slight effect for the range as can be seen in Fig. 2.6a, but it is applied so the results are in line with that of the sill, where the transform does have a large effect, as shown in

Section 2.6.2. While the fit is not perfect, the seasonal effect is followed quite well. Most of the strong differences occur in November when the variogram is more often linear than spherical. The values for this fit can be found in Table 2.2.

Another way to look at the fit is to take the average for each day of the year (DOY) of those 30 years. As shown in Figure 2.7a, this results again in a clear seasonal trend. The solid line is the average of the estimated ranges from the 90-day moving window spherical variograms, but with all ranges larger than 300 km removed. The dashed lines are the climatological fits through the 30 year data, which follows the average rather well. The exception to the smooth cosine of the climatological fit is around November and December, when the semi-variance tends to become more linear than spherical and the range therefore becomes larger than 300 km. The slight low here is due to the fact that when the range is linear beyond 300 km the data is filtered and remaining spherical fits tend to have fairly short ranges, which influences the average.

Seasonal sill

Like the range in the previous section, the seasonality is clearly apparent for the sill of the fitted variograms (Fig. 2.5b). The sill data were again sqrt-sqrt transformed and fitted to the cosine model of Equation (2.6). The corresponding values are found in Table 2.2.

Similar to the range in Figure 2.7a the average sill is also plotted as a function of the time of year. Fig. 2.7b shows the results, where the solid line is the sill (with all values where the range was more than 300 km removed) and the dashed lines are the climatological fits. Again the seasonality is clear. The sill reaches a maximum in August and a minimum in February. Where at first a low could be seen in the fitted cosine function of the range, there is now a peak in the sill. Again this can be attributed to the prevailing rain types during winter and summer. With convective rainfall in summer the variance between pairs will be high, but in winter, with similar rain rates over large distances, the daily rain sum will be quite similar, which results in a low variance. Unlike with the range exceptions do not noticeably occur when the fit is more linear than spherical around November. There is a shift of about 150 days between the fitted cosines of the sill and range. A shift of approximately half a year is to be expected, with the largest variance during late summer, when strong convective thunderstorms are most common resulting in a large sill and small range and the equal amounts of daily rain sums between pairs at longer distances in winter, resulting in a large range and a small sill. The fact that the shift is in fact only about 5 months can be partially explained by the transition period at the end of summer when the rain events become both larger in size and in amount. This causes both the sill and the range to increase. From September the scale of the rain events still grows, increasing the range, but the amounts of precipitation will start to decrease, lowering the sill.

Table 2.2: Parameters of the sqrt-sqrt transformed cosine functions of the sill, range and root mean square errors for the fitted spherical variograms using the daily rain sums of 33 KNMI stations with a 90-day moving average window.

	$1/f$	A	t_0	x_0
range	365	1.3	2	19.8
sill	365	0.3	217	1.8
RMSE	365	0.3	207	1.1

Seasonal root mean square error

The sum of squared errors (SSE) is the sum of the squared differences between the empirical semi-variogram values and the fitted spherical variogram. Taking the root of the mean of the SSE results in the root mean square error (RMSE). The RMSE is small for most of the year, but becomes large during summer, when measured amounts between gauges can strongly differ (Fig. 2.5c). The peaks occur mostly around August, but can be a month earlier or later. Again a cosine was fitted to the sqrt-sqrt transformed data and the corresponding parameter values can be found in Table 2.2.

Like the sill and range, the difference between the low values in winter and the high values in summer can be explained by the type of precipitation during these times. It follows the shape of the sill closely (see Figs. 2.7b and c). As the variability between gauges tends to be small during winter, the squared differences from the fitted variogram will not be high. In summer the opposite occurs, which results in the high RMSE values.

Quality of the seasonal fits

To assess the quality of the climatological models for range and sill these fits are compared with the actual range and sill values. This can be done by looking at anomalies. In Fig. 2.8 the climatological fits (the cosine functions fitted to the transformed range and sill values) are subtracted from the original fits (the range and sill values determined for each day separately), with ranges beyond 300 km removed, to find the anomalies for sill and range. For both the sill and range it is difficult to find a clear seasonal effect. In Fig. 2.9 the mean and standard deviation for each DOY over the 30 years shown in Fig. 2.8 are plotted. As can be seen in Fig. 2.8f the estimated range can differ up to 12% of the actual range, but the distribution is such that most values are concentrated around zero. For the sill the errors can be up to 14%, but here the distribution is nearly uniform.

To look in more detail at the difference between the actual range and sill values and the climatological fit the one-year period between March 2004 and March 2005 is evaluated. In addition to the 33 KNMI stations, 10 gauges from

the dense rain gauge network around Cabauw are employed. This year has a fairly high sill and range and illustrates a case where the spherical variogram parameters differ fairly strongly from the climatological fit.

As can be seen from the fit of the sill, using KNMI and UU-WUR data, in Fig. 2.10a, the climatological fit (dashed cosine) for this year is fairly accurate, although its estimated peak during summer is smaller than that of the actual sill for this year (solid black line). The peak of the actual sill, while similar in shape, is smaller than the estimated sill using only the KNMI data (grey solid line) as well. The difference in the estimated parameters is caused by the rain gauge network characteristics. This shows that the parameters are sensitive to the density and location of the data points. The exact sensitivity is beyond the scope of this thesis. Note, however, that for both range and sill the effect of network characteristics is smaller than of the year-to-year variations. The comparison of range signals shown in Fig. 2.10b leads to conclusions similar to those for the sill (Fig. 2.10a), but with larger overall differences. The actual range has a much greater amplitude than the climatological range and also has a less smooth signal than that of the sill. This again illustrates that the range is less stable than the sill.

Figure 2.11 illustrates 4 cases throughout the year. In spring (a) the climatological fits and the actual sill and range values are similar, but the climatologies overestimate both sill and range slightly. The fit at short range does not seem to be ideal either, as all points up to 50 km lie above the fitted curve. Applying some sort of nested variogram with one fitted up to 50 km and one beyond could result in a better fit (e.g. *Berne et al.*, 2004a). From this a better climatological fit might be estimated as well. The fits in summer (b) have a large variance and tend to have a fairly large scatter around the fit, resulting in a large RMSE (also see Figure 2.5c). Due to the large variability of summer rain, where it is possible to have both strongly localized convective cells and more large scale stratiform rain, the variance between data-pairs varies quite a lot. As described in Sections 2.6.2 and 2.6.2 this results in a large sill and a short range during summer. The exact timing of the maximum variance during summer varies from year to year and can even be absent or consist of several peaks.

Figure 2.11c illustrates the common problem of fitting rainfall variograms in the Netherlands around November, where often the fit to the data is nearly linear. This results in an estimated range far beyond the range of the furthest data-pair.

2.6.3 Short range analysis

For catchment hydrology in the Netherlands the relevant areas tend to be small and therefore an appropriate variogram at short ranges is important. As mentioned before, a lack of rain gauges for accurate estimates of catchment rainfall can be an important factor in hydrology and therefore it is important to find accurate variograms to interpolate between gauges or even extrapolate from a single gauge in a catchment.

Figure 2.12 illustrates the short range fit using 10 gauges from the dense rain gauge network around Cabauw mentioned in Section 2.3.2. As the semi-variance tends to be nearly linear up to this maximum distance of 10 km and the range of the variogram is far beyond this distance, the fit of the semi-variance illustrated in these figures is carried out through linear regression (see Eq. 2.4). In fitting the climatological variogram to the KNMI data the binning of data pairs was carried out using distance classes of 5 km. For this short range this bin size is set to 500 m. The top left panel shows the semi-variance in spring when rain variability is already increasing to the summer maximum. The dashed line is the linear fit to the data of only the 10 gauges around CESAR (UU-WUR), the dotted line is the climatological fit, the solid line is the fit based on the 33 KNMI gauges combined with the 10 UU-WUR gauges (KNMI-UU-WUR), and the dash-dotted line is the fit based on the 33 KNMI gauges only (KNMI). It is clear that the actual semi-variances are higher than those resulting from the different variogram models. This is the case for most of May and June 2004. As can be seen in the top left panel of Fig. 2.11 the semi-variances for the first 50 km are indeed estimated to be lower than the values found for the UU-WUR gauges. As an accurate estimate of the variance at short distances is especially important for the purpose of small catchment hydrology it is clear that the fit found for the KNMI and UU-WUR gauges combined is not perfect. The KNMI-UU-WUR fit does perform better than the KNMI fit, but the effect is small. As mentioned before, applying nested variograms could solve the problem by merging a variogram fitted up to 50 km and one beyond 50 km. For summer (top right panel) the slope of the actual fit and the fits found for UU-WUR, KNMI and KNMI-UU-WUR are very similar. While the RMSE is fairly large the fit of the longer range with only one spherical variogram appears to work rather well for the summer and autumn (bottom left panel). Finally, during winter the fit to the semi-variance is again larger than that of the other fits. Looking at the bottom right panel of Fig. 2.11, it can be concluded that this is caused by the same issue as was found for May and June 2004.

The results are summarized in Fig. 2.13 by estimating a linear slope for all fits for the first 10 km. Here the issues with differences between fitting at only short distances and fitting over longer distances become more clear. During winter and spring the semi-variances at short ranges are larger than KNMI-UU-WUR variogram fit estimates and during summer and fall the values are fairly similar. Further differences are difficult to correct for due to annual differences that cannot be taken into account using a seasonal fit. Even though there are these year-to-year differences it was shown in Sections 2.6.2 and 2.6.2 that the sill and range can be predicted well on average, with the exception of November, when the variogram tends to be linear.

2.7 Conclusions and recommendations

Variograms of daily rainfall are found to be strongly seasonal. Such seasonal fluctuations can be parameterized by very simple cosine functions. The average sill and range found from the fitted spherical variograms follow a cosine function over the entire year with the exception of November, where the range often exceeds 300 km. Year-to-year variations of the fitted spherical variogram parameters have been shown to exist, but they are found to be limited with respect to the amplitude of the seasonal signal. On average, the simple cosine parameterizations of the variogram sill and range have been shown to perform well.

For shorter ranges (up to 10 km) the climatological fit follows the seasonal trend well, but underestimates compared to the fit for the year between March 2004 and March 2005. The difference between the short-range fit and long-range fit up to 10 km for the studied year is small during summer and autumn, but becomes stronger during winter and spring. This problem is due to the year-to-year variability in semi-variance and a possibly inappropriate variogram model (linear for November) and transform. Most of the difference can be explained by daily fluctuations, as the long and short ranges are mostly similar except for the aforementioned problems of variogram fitting during winter and spring, which could be solved by a nested variogram. In conclusion, while the climatological fit in this case was underestimated for both long and short ranges, the semi-variance at short range could be estimated fairly well on average, as the climatological parameterization was shown to fit well for the 30 year data.

While the results for long range climatological variograms are promising, the case study of short-range climatological variograms reveals issues that need to be resolved. Some recommendations for continued research would be to:

- Use nested variograms for winter and spring periods;
- Test variogram shape and stability for other time scales;
- Evaluate the robustness of the climatological variogram by leaving some gauges out of the network and quantifying the differences (cross-validation), or alternatively comparing the estimated values with radar rainfall maps.

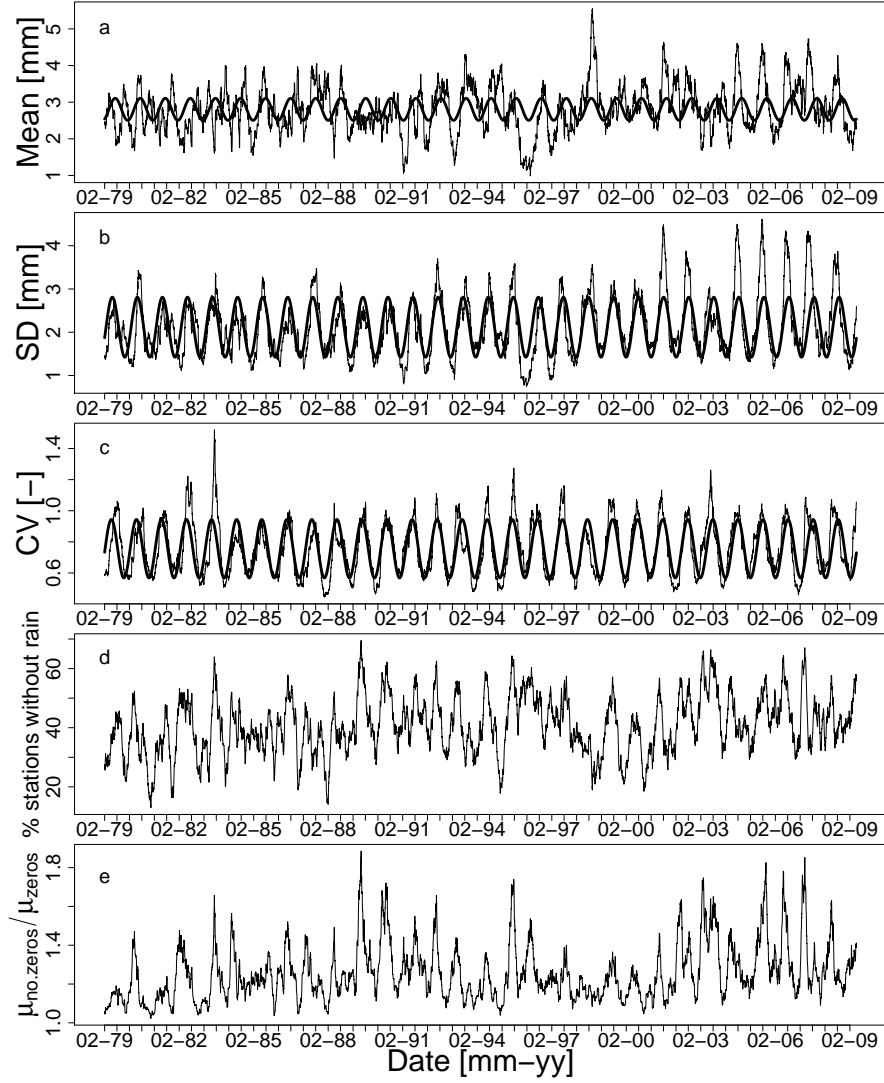


Figure 2.4: Temporal variation of rainfall spatial statistics, determined using a 90-day moving window. Panel a is the 90-day moving average of the daily rainfall sum. Panel b is the average standard deviation for a 90-day moving window. Panel c is the coefficient of variation. Bold lines are cosines fitted through the data. Panel d is the 90-day moving average of the percentage of dry stations. Panel e is the ratio of the mean without dry stations and the mean with dry stations included.

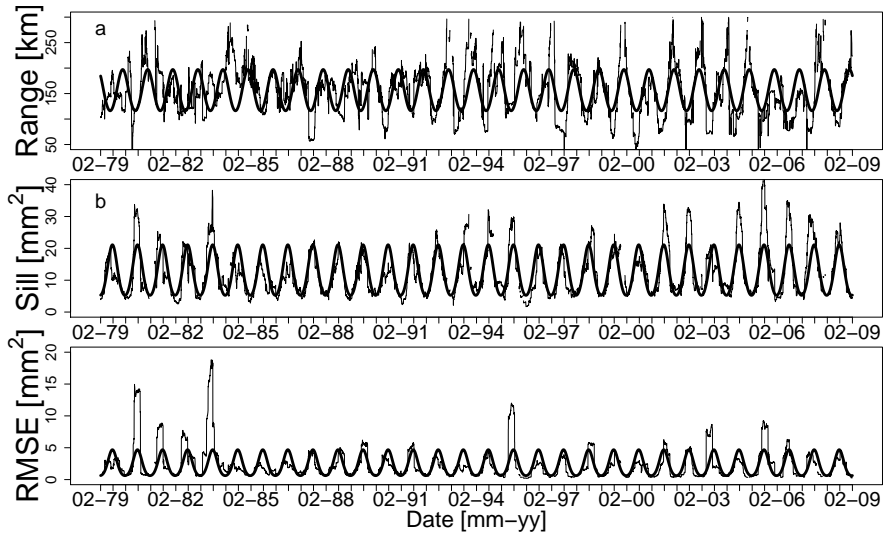


Figure 2.5: Variation of 90-day moving window variogram parameters range (a), sill (b) and root mean squared error (c) for 30 years of daily rainfall data. The thin lines are the values found for each daily average and the bold lines are the cosines fitted through the data.

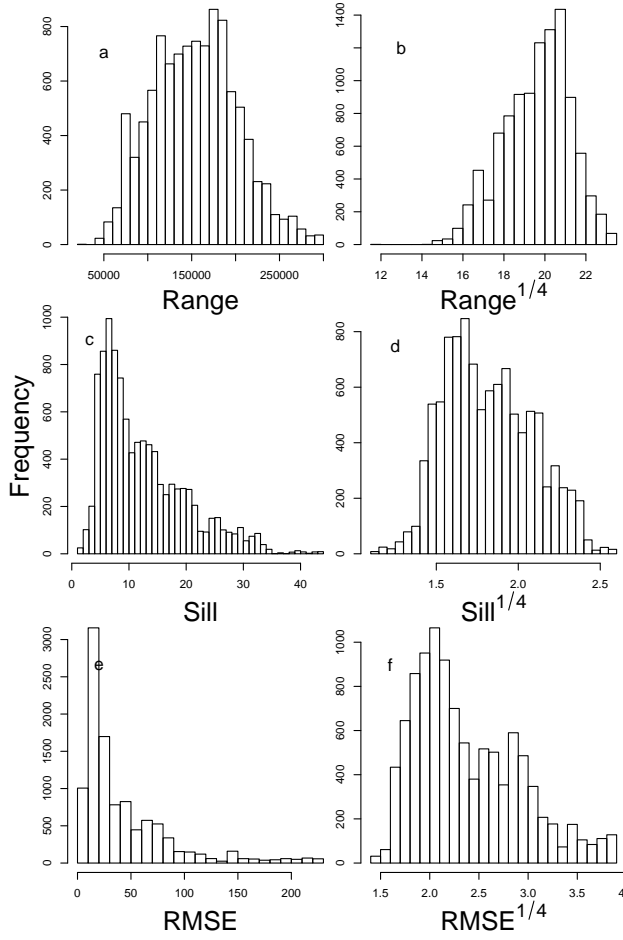


Figure 2.6: Histograms of the range, sill, and RMSE before (a, c, and e, respectively) and after (b, d, and f, respectively) a sqrt-sqrt transform.

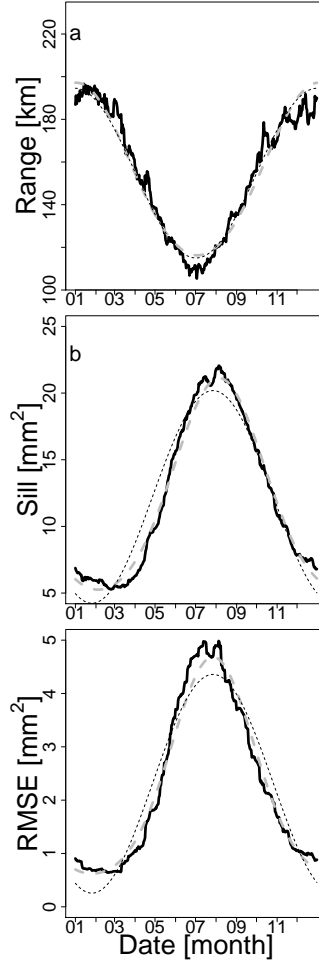


Figure 2.7: Average daily variation of the range (a), sill (b) and root mean square error (RMSE) (c) for each day of year. The solid lines are the estimated values, the black dashed lines the cosine functions fitted on the normal data and the grey dashed lines the cosine functions fitted on the sqrt-sqrt transformed data.

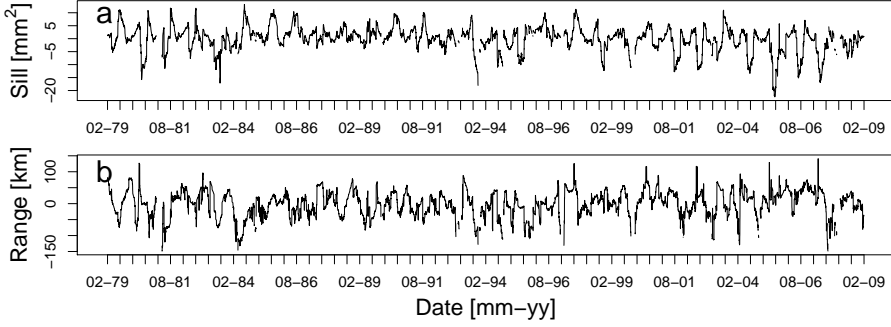


Figure 2.8: The difference of the climatological fitted cosine and the actual values resulting in the anomaly of sill (a) and range (b).

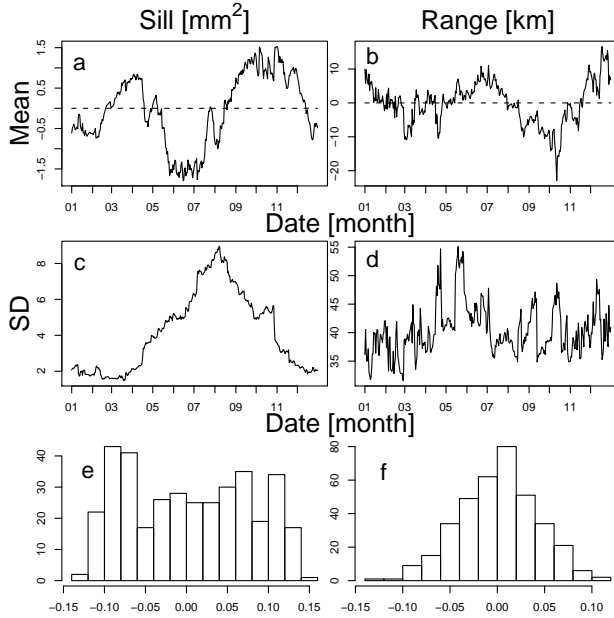


Figure 2.9: Mean (a and b), standard deviation (SD; c and d), and histograms (e and f) of the sill (a, c, and e) and range (b, d, and f). Mean and SD are shown as functions of the time of year.

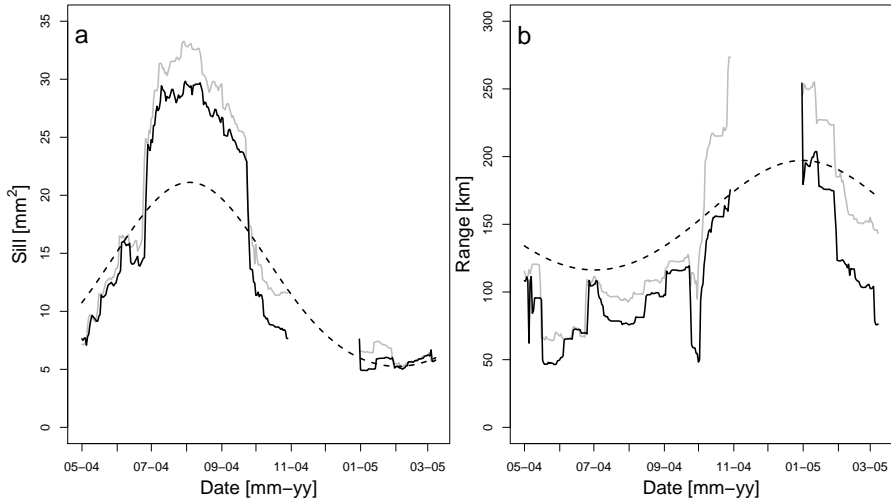


Figure 2.10: Parameters of the fitted semi-variograms between March 2004 and March 2005. Left panel is sill and right panel is range of the fitted variogram. The dashed cosines are the estimates from the climatological variogram, the solid black lines are the fits for each day using all KNMI and UU-WUR data, and the solid grey lines are the fits for each day only using the KNMI data.

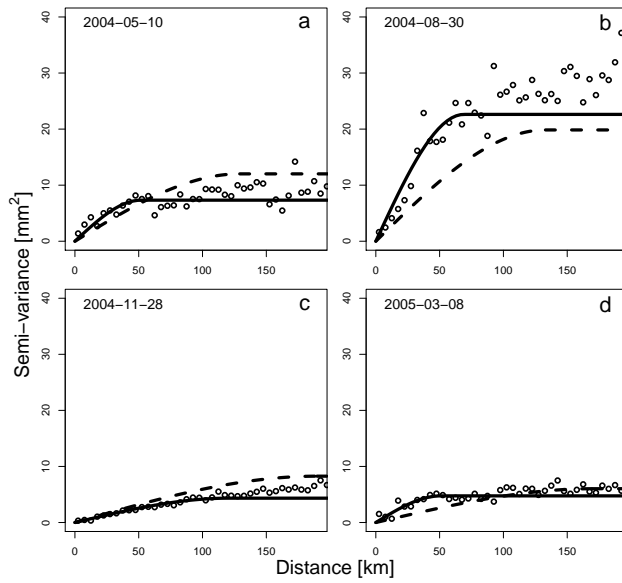


Figure 2.11: Example of fitted semi-variograms for four days between March 2004 and March 2005. The solid line is the fitted variogram and the dashed line is the climatological variogram.

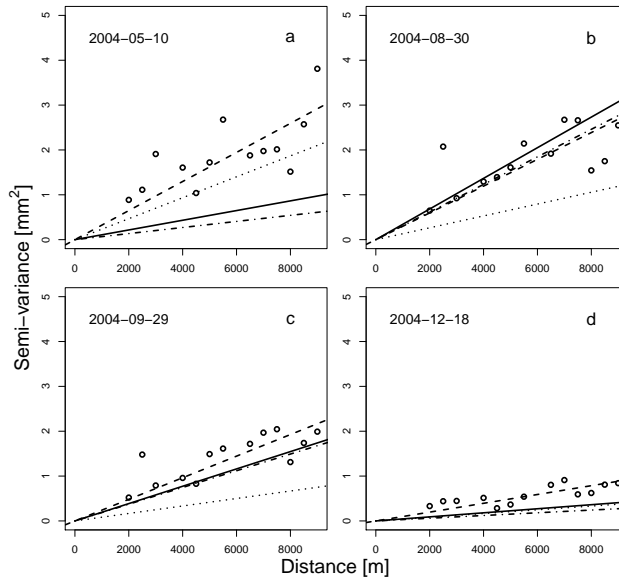


Figure 2.12: Four examples of fitted variograms using only 10 gauges of the dense rain gauge network between March 2004 and March 2005. The dashed lines are the actual fits (UU-WUR), the dash-dotted lines are the fits through the KNMI data (KNMI), the solid lines are the fits found in Section 2.6.2 from the combined KNMI and UU-WUR rain gauge data (KNMI-UU-WUR), and the dotted lines are the climatological fits.

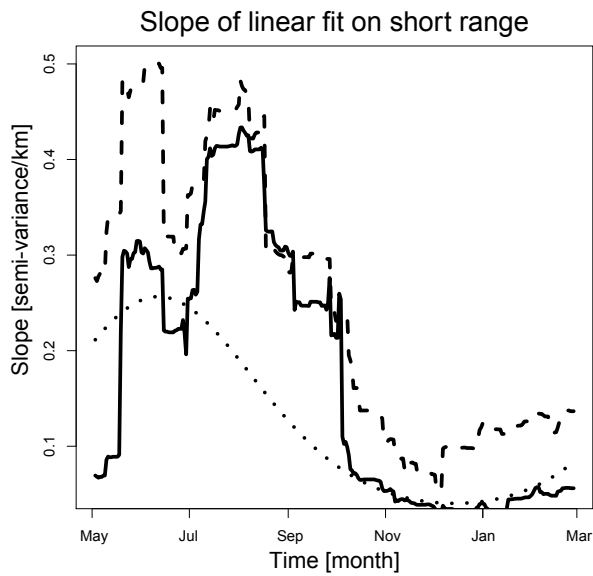


Figure 2.13: Slope of the first 10 kilometers of the variogram for the period between March 2004 and March 2005. The dashed line is the actual fit, the solid line is the fit found in Section 2.6.2 from the combined KNMI and UU-WUR rain gauge data and the dotted line the climatological fit.

CHAPTER 3

Seasonal semi-variance of Dutch rainfall at hourly to daily scales

3.1 Summary

Using 30 years (1979-2009) of data from 33 automatic rain gauges in the Netherlands, a study of the space-time variability of rainfall is performed. This study uses 90-day averaged semi-variograms to find seasonal signals in the fitted spherical semi-variogram parameters of rainfall rainrates in the Netherlands, for accumulation intervals between 1 and 24 hours. These signals can be well-described by simple cosine functions. The dependence of these cosine functions on the accumulation interval is modeled in two different ways: 1) power-law relations between the variogram parameters and the accumulation interval, and 2) power-law relations between the parameters of the cosine functions and the accumulation interval. For the first method the cosine function at the 24-hour accumulation interval is also needed. The second of these methods has more parameters, but is shown to model the temporal scaling best. The space-time scaling relations found in this chapter are compared to those found by others for similar and contrasting climates. Seasonality is shown to play an important role in determining rainfall and spatial variability.

This chapter has been published with minor modifications as: van de Beek, C. Z., Leijnse, Torfs, P. J. J. F. and Uijlenhoet, R., 2011. *Seasonal semi-variance of Dutch rainfall at hourly to daily scales*, Advances in Water Resources, 15, 171-183

3.2 Introduction

The main goal of this study is to describe rainfall spatial variation at different accumulation intervals (1 to 24 hours) using simple parameterizations. Accurate rainfall estimates are important in many disciplines such as hydrology, meteorology and climatology. Especially in catchment hydrology accurate estimates of rainfall with high spatial and temporal resolution are important for understanding catchment behavior and predicting floods. For the employed rainfall-runoff models a daily resolution of precipitation is often not enough. Especially for urban settings with fast response times a higher temporal resolution is required (*Chaubey et al.*, 1999; *Smith et al.*, 2002, 2005; *Aronica et al.*, 2005; *Vaes et al.*, 2005; *Olsson et al.*, 2009). Many modern instruments are, to a greater or lesser degree, able to measure rainfall both in space and time. Examples are disdrometers (*Joss and Waldvogel*, 1977) and microwave links (*Leijnse et al.*, 2007b), but most common are rain gauges and radar. Radar measurements can offer high resolution coverage of rainfall fields in both space and time. The resolution and quality of these measurements depend on the specifications of the system, like antenna size, wavelength, scanning strategy and polarimetric and doppler capabilities. However, there are limitations to radars, as they measure a reflected signal from a volume in the air, which needs to be translated to a rain rate at the ground. Also factors like ground clutter, attenuation and calibration degrade the accuracy of the estimated rain fields (*Marshall et al.*, 1955; *Brangi and Chandrasekar*, 2001; *Meischner*, 2004; *Chandrasekar and Lim*, 2008; *Uijlenhoet*, 2008; *van de Beek et al.*, 2010).

Traditionally rain has been measured by rain gauges. These instruments are still widely used, especially in areas where more expensive systems cannot be afforded. Rain gauges can measure accurately for a very small area, but give little information about the spatial variability. Unlike radars, which provide an image only once every scan with typical intervals of 5 to 15 minutes for ground-based and 3 or more hours for space-borne systems, modern gauges are able to measure rainfall continuously, although their measurements are usually accumulated to 10 minutes or longer intervals. While rain gauges are usually seen as "ground-truth", these instruments are far from perfect as they offer only point measurements, suffer from calibration errors, wind effects and sampling uncertainty. Still these instruments offer a fairly accurate and affordable way of measuring rainfall (*Humphrey et al.*, 1997; *Calder and Kidd*, 1978; *Marsalek*, 1981; *Habib et al.*, 2001; *Ciach*, 2003; *Sieck et al.*, 2007).

In this chapter we apply the same methodology to describe the seasonal variation of variogram parameters as was applied to daily rainfall accumulations in the previous chapter. Results from these analyses for sub-daily accumulation intervals (1-24 hours) are then used to derive simple relations for describing rainfall spatial variability as a function of both the accumulation interval and the time of year. Such parameterizations can be used in hydrology for purposes of conditional simulation and spatial interpolation. Other studies have focussed on the space-time variability of rainfall, but not on its seasonality.

In Section 3.3 the data and study area are described. The theory and

method are described in Section 3.4. Section 3.5 describes the results of the analysis of the scale-dependence of the semi-variance. Finally, Section 3.6 summarizes the study and offers recommendations for future work.

3.3 Study area and data

The Royal Netherlands Meteorological Institute (KNMI) operates 35 automatic rain gauges in the Netherlands (i.e. one gauge per 1000 km²). Originally the network consisted of mechanical pluviographs, but from the late 1970's onward they were replaced by electronic rain gauges. These rain gauges measure the amount of precipitation from the displacement of a float in the gauge reservoir. Thirty years of data from 33 of the automatic KNMI rain gauges were used for this study. The period between January 1, 1979 and February 15, 2009 was considered. The stations have a relatively uniform distribution over the Netherlands as can be seen in Fig. 3.1. The data are available in one-hour accumulations and were aggregated to intervals of 1, 2, 3, 4, 6, 8, 12 and 24 hours. These accumulations are converted to average rain rates, on which the analyses in the remainder of this chapter are carried out. The hourly accumulations are available with an accuracy of 0.1 mm. Non-zero rainfall accumulations below 0.05 mm have been set to 0.05 mm in this dataset to indicate nonzero rain (this would otherwise be rounded to zero). While this might give a slight overestimation for rainfall at very low intensities it allows for discrimination between dry and wet periods. The resulting distribution of distances between the 33 stations can be found in Fig. 3.2, showing a good coverage between 20 and 250 km and few station pairs beyond these ranges.

3.4 Method

Assuming intrinsic stationarity and isotropy the empirical semivariogram can be computed for each time step as follows:

$$\hat{\gamma}(h_i) = \frac{1}{2n_\gamma(h_i)} \sum_{j=1}^{N-1} \sum_{k=j+1}^N |z(x_j) - z(x_k)|^2 H\left(\frac{1}{2}\Delta h - ||x_j - x_k| - h_i|\right), \quad (3.1)$$

with

$$n_\gamma(h_i) = \sum_{j=1}^{N-1} \sum_{k=j+1}^N H\left(\frac{1}{2}\Delta h - ||x_j - x_k| - h_i|\right). \quad (3.2)$$

Here, h_i is the center of class i of inter-gauge distances (with class width Δh), x_j is the location of gauge j , N is the number of gauges, $z(x)$ is the rainfall intensity at location x , and $H(x)$ is the Heaviside function:

$$H(x) = \begin{cases} 1 & x \geq 0 \\ 0 & x < 0. \end{cases} \quad (3.3)$$

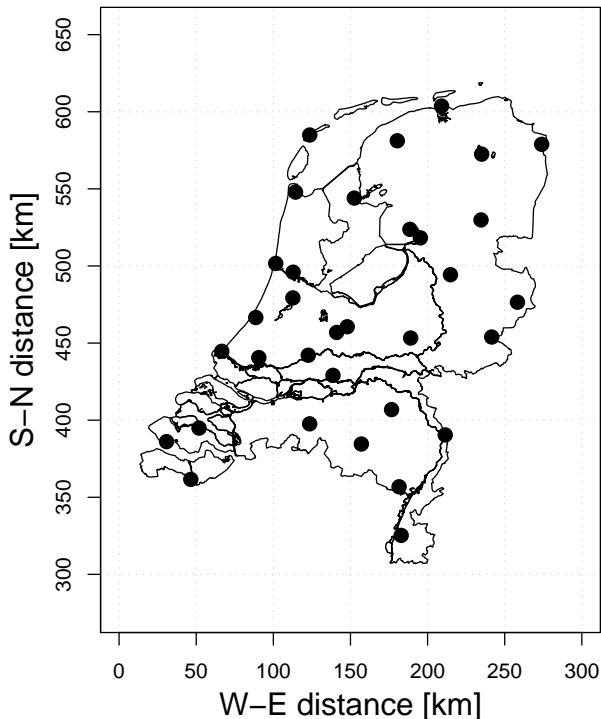


Figure 3.1: Locations of the KNMI automatic rain gauges.

Note that both $\hat{\gamma}$ and n_γ are functions of time (through $z(x, t)$ and $N(t)$). In this study, $\Delta h = 5$ km. As the Netherlands has very little orography, we feel that the assumption of intrinsic stationarity is reasonable. The assumption of isotropy is very difficult to test given the available dataset. This assumption was made for the sake of simplicity of the description of the spatial rainfall variability. An extensive study of the effect of our assumptions is difficult as the area and number of gauges are limited. Inclusion of data from surrounding countries may yield better insight. However, this is beyond the scope of the present study.

One of several variogram models can be fitted to the empirical variograms. Of these models a simple spherical variogram was selected as it describes most rainfall semi-variograms well, with parsimonious and easily interpretable parameters that have physical meaning (also see (Berne *et al.*, 2004c)).

$$\gamma(h) = \begin{cases} c_0 + c_1 \left(\frac{3}{2} \frac{h}{r} - \frac{1}{2} \left(\frac{h}{r} \right)^3 \right) & \text{if } 0 \leq h \leq r \\ c_0 + c_1 & \text{if } h > r \end{cases} \quad (3.4)$$

Here $c_0 + c_1$ is the sill, r is the range and c_0 is the nugget. The sill is the

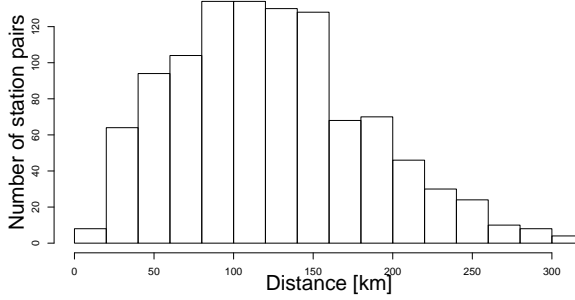


Figure 3.2: Histogram of inter-station distances of the selected 33 stations, using a bin width of 20 km.

maximum value of the fitted variogram and the range the distance at which this value is reached. The nugget is the variance at zero distance and is negligible for the dataset (see van de *van de Beek et al. (2011a)*). The equation can therefore be reduced to a function that only depends on sill and range:

$$\gamma(h) = \begin{cases} c_1 \left(\frac{3}{2} \frac{h}{r} - \frac{1}{2} \left(\frac{h}{r} \right)^3 \right) & \text{if } 0 \leq h \leq r \\ c_1 & \text{if } h > r \end{cases} \quad (3.5)$$

A moving window is applied to the empirical variogram, whereby weights are applied based on the number of available gauge pairs per time period per distance class

$$\hat{\gamma}_{\text{av}}(h_i, t_j) = \frac{1}{n_{\gamma, \text{av}}(h_i, t_j)} \sum_{k=-\frac{1}{2}\tau/\Delta t}^{\frac{1}{2}\tau/\Delta t} n_{\gamma}(h_i, t_{j+k}) \hat{\gamma}(h_i, t_{j+k}), \quad (3.6)$$

with

$$n_{\gamma, \text{av}}(h_i, t_j) = \sum_{k=-\frac{1}{2}\tau/\Delta t}^{\frac{1}{2}\tau/\Delta t} n_{\gamma}(h_i, t_{j+k}). \quad (3.7)$$

Here, τ is the averaging period and Δt ($= t_{j+1} - t_j$) is the time interval at which the data are available. For this study $\tau = 90$ days.

This averaging is done to reduce the noise related to the day-to-day variations of rainfall and to have more data available per distance bin. In addition, as there are dry periods over the entire Netherlands, this method ensures that no variograms corresponding to dry weather are included. The averaging window has equal weights for all 90 days. A triangular weighing function was

tested as well as a period of only 60 days. Both had little impact on the resulting semi-variograms compared to the 90-day window. Spherical variogram models were fitted to the averaged empirical semi-variograms using the method of maximum likelihood (see (*Diggle and Ribeiro Jr.*, 2007), Chapter 5), where the weight of the different classes of inter-gauge distance is determined by the amount of point pairs in the respective class. *Zimmerman and Zimmerman* (1991) showed that a likelihood based estimator is better for fitting the chosen parametric model to a semi-variogram than a least-squares estimator. A maximum range of 200 km was selected to use distance pairs for fitting, as the number of distance pairs decreases rapidly beyond 200 km (see Fig. 3.2). Around November the empirical variogram often becomes approximately linear for the entire 200 km and even up to the furthest distance pair at 315 km. This causes problems for fitting a spherical variogram as the estimated sill and range become interdependent (see van de (*van de Beek et al.*, 2011a)). For estimated ranges beyond 300 km it was therefore decided not to use these variogram parameters in subsequent analyses.

As a measure of the goodness-of-fit, we also compute the RMSE between the fitted spherical and averaged empirical variograms, where we take the number of data points into account (as was done in the fitting procedure)

$$\text{RMSE}(t_j) = \sqrt{\frac{\sum_{i=1}^{N_h} n_{\gamma, \text{av}}(h_i, t_j) (\hat{\gamma}_{\text{av}}(h_i, t_j) - \gamma(h_i))^2}{\sum_{i=1}^{N_h} n_{\gamma, \text{av}}(h_i, t_j)}}. \quad (3.8)$$

The resulting fluctuations of range and sill for each time interval over the 30 years of data can be fitted with a simple cosine function using spectral analysis. Such a cosine function can be expressed as:

$$y_t = x_0 + A \cos(2\pi f(t - t_0)) \quad (3.9)$$

Here x_0 is the offset, A is the amplitude, f is the frequency (1/day) and t_0 defines the start day of the cosine function (*Shumway and Stoffer*, 2006).

The sill, range and RMSE derived from the rainfall data in this study, are not symmetrically distributed, making Eq. (3.9) not sufficient to describe their variability. The sill, range and RMSE that were found from the modeled spherical semi-variograms therefore need to be transformed in this case, using a square root-square root (sqrt-sqrt) transform, to make them more symmetrically distributed. As was shown for the daily accumulations in (*van de Beek et al.*, 2011a), this transform describes the signal of the sill and range well. For shorter accumulation times it will also be shown in the next section. It is then possible to fit a cosine function to these transformed sill, range and RMSE. It should be noted that in this study the semi-variograms of the rain rates at different accumulation intervals [mm h^{-1}] are used, as opposed to the previous

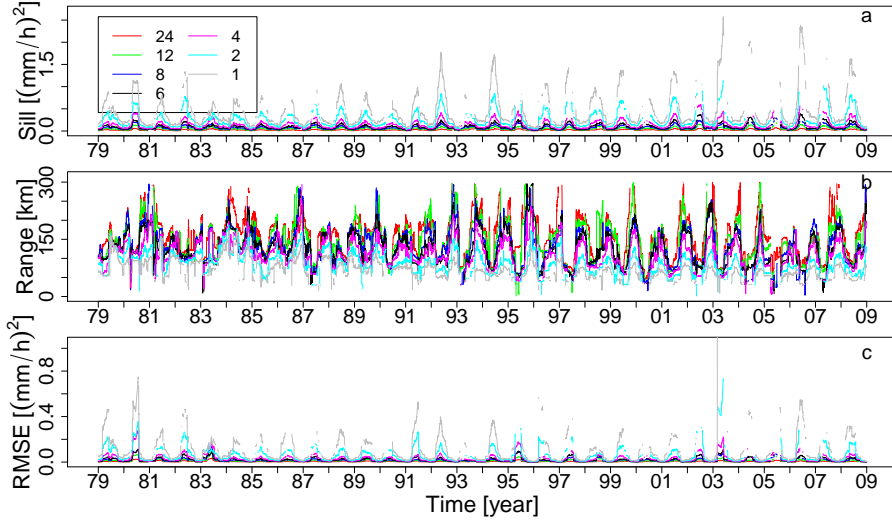


Figure 3.3: a) The seasonal fluctuation of the 90-day averaged sill between January 1st, 1979 and February 15th, 2009. The accumulation intervals indicated in the legend are given in hours. b) The same for the range. c) The same for the RMSE.

study (*van de Beek et al.*, 2011a), where the accumulations [mm] were considered. While accumulations will be mentioned throughout this thesis these mean the estimated average rain rates over a certain accumulation period.

This results in the following function that is similar to Eq. (3.9):

$$x_t^T = x_0 + A \cos(2\pi f(t - t_0)) \quad (3.10)$$

where x_t^T can be the transformed range, sill, or RMSE. However, the parameters of this function are highly difficult to interpret as they are applied to the transformed signals. Because the transformed sill, range, and RMSE have little physical meaning, a back-transformation with a power 4 has to be applied to the cosine to compare it to the actual values.

$$x_t = (x_0 + A \cos(2\pi f(t - t_0)))^4 \quad (3.11)$$

where x_t can be the range, sill, or RMSE.

3.5 Results

3.5.1 Variation of rainfall at different temporal scales

This section shows analyses of the semi-variance using the 30-year raingauge data at different temporal scales. As was shown in (*van de Beek et al.*, 2011a)

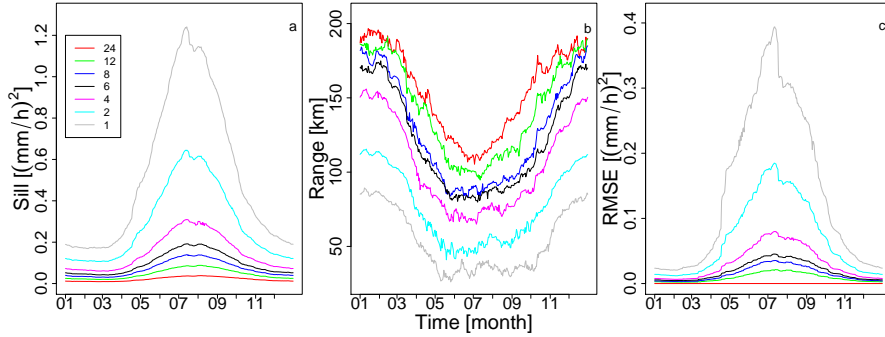


Figure 3.4: a) The seasonal fluctuation of the 90-day averaged sill between January 1st, 1979 and February 15th, 2009, averaged for each day of the year. The accumulation intervals indicated in the legend are given in hours. b) The same for the range. c) The same for the RMSE.

Table 3.1: Mean and standard deviation (sd) of the sill $[(\text{mm h}^{-1})^2]$, range [km] and RMSE $[(\text{mm h}^{-1})^2]$ for all accumulation intervals

	24	12	8	6	4	3	2	1
mean sill	0.02	0.05	0.07	0.10	0.15	0.20	0.29	0.53
sd sill	0.01	0.02	0.04	0.05	0.08	0.12	0.18	0.36
mean range	155	143	127	120	105	93	76	54
sd range	29	32	34	33	30	28	24	21
mean RMSE	0.00	0.00	0.02	0.02	0.03	0.04	0.07	0.14
sd RMSE	0.00	0.01	0.01	0.01	0.03	0.03	0.06	0.12

there is a strong seasonality in variogram parameters computed from daily rainfall accumulations. These analyses are extended in the present study to include shorter accumulation intervals. Note that unlike in *van de Beek et al. (2011a)*, where analyses were carried out on accumulations, the analyses presented in this chapter are carried out on rainfall intensities.

Seasonal sill and range

In Fig. 3.3 time series over 30 years of the sill, range, and RMSE of the fitted spherical semi-variograms at different temporal scales can be seen. As the rain rates at 24-hour accumulation will have the largest averaging time of the accumulation intervals considered here, it is expected that the sill is smallest for this accumulation interval. For the smallest accumulation interval of 1-hour that the maximum rain rate will be the highest. Because rainstorms move, rainfall accumulations become more “smeared” in space with increasing accumulation

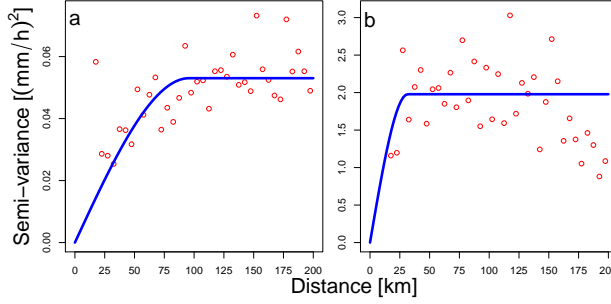


Figure 3.5: Variograms of rainfall intensity of a typical summer situation (on 24-08-2006) for daily (left) and hourly accumulations (right).

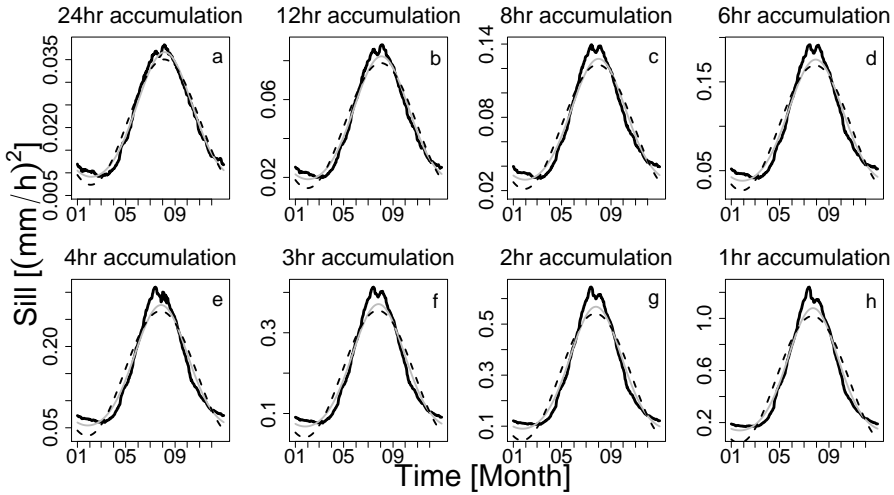


Figure 3.6: The individual fits of the sill for each time interval. The black lines are the estimated values, the dashed lines the fits to the untransformed values and the grey lines the fits to the sqrt-sqrt transformed values.

intervals, leading to longer ranges in fitted variograms. The seasonality that can be seen for the daily interval (*van de Beek et al.*, 2011a) is also apparent for shorter accumulation intervals. As expected, the sill attains larger values and the range attains lower values as the accumulation intervals become shorter. The sills in Fig. 3.3a show a seasonal trend, with high values in summer and low values in winter. This is expected as there will be more convective precipi-

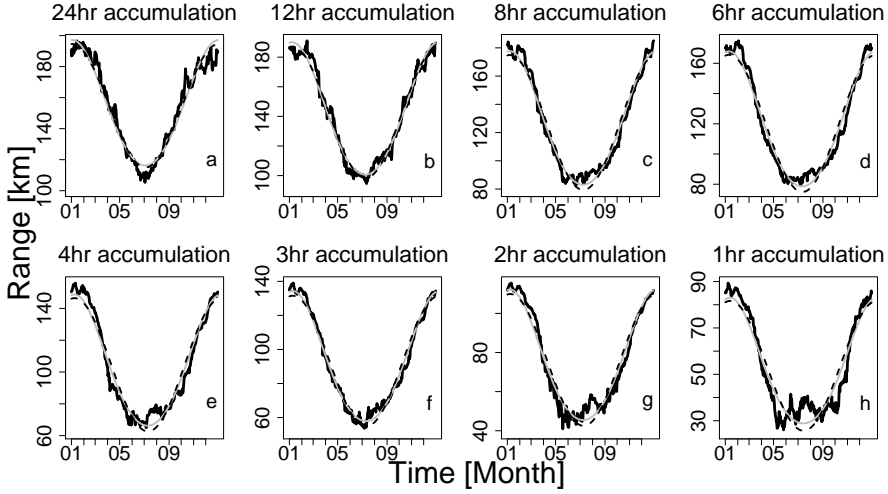


Figure 3.7: The individual fits of the range for each time interval. The black lines are the estimated values, the dashed lines the fits to the untransformed values and the grey lines the fits to the sqrt-sqrt transformed values.

tation during the summer with larger differences in rainfall amounts over short distances. During winter rainfall tends to be more stratiform, which results in lower and more spatially uniform rainfall accumulations. The seasonality of the range can be seen in Fig. 3.3b, but with a less smooth signal than for the sill, which will be illustrated in section 3.5.2. Maximum values of the range coincide with minimum values of the sill. This is to be expected as the precipitation in summer will have a very short decorrelation distance, whereas, during winter with stratiform rain, it will tend to be similar over large distances. Fig. 3.3c shows the RMSE which can be seen to be very similar in shape to the sill. This is logical as the RMSE is strongly influenced by the variability in the rain rate.

Thirty-year averages of the sill, range and RMSE have been computed for each day of the year (DOY), and are shown in Fig. 3.4. These graphs show the seasonal signal in more detail than Fig. 3.3. The sill follows a pattern during the year that resembles a cosine, but the shape is distorted, with narrow peaks and broad valleys, illustrating that a transform, such as the sqrt-sqrt transform, is necessary. High values of the sill are visible in August, during the most convective period of the year and low values are observed in March, when rainfall accumulations across the country tend to be similar. For longer time intervals the values of the sill become smaller, but the shape remains similar to the 1-hour sill. In Table 3.1 the mean and standard deviation are shown for the sill at each accumulation interval, based on the 30-year averages. The

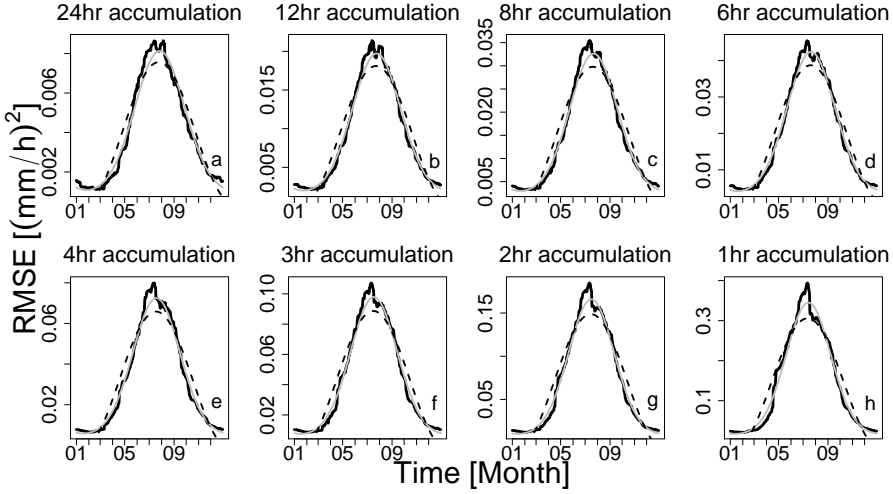


Figure 3.8: The individual fits of the RMSE for each time interval. The black lines are the estimated values, the dashed lines the fits to the untransformed values and the grey lines the fits to the sqrt-sqrt transformed values.

standard deviation (sd), which is a measure of the amplitude of the seasonality, can be seen to become proportionally larger for shorter accumulation intervals. The shape of the yearly trend of the range in Fig. 3.4b, while less smooth than the sill, again closely resembles a cosine-shape. Unlike for the sill, the influence of the accumulation period is mainly on the mean of the range throughout the year, while the effect on the amplitude of the seasonality (sd in Table 3.1) is much less. The signals are much closer to a real cosine than the sill, although at intervals shorter than 6 hours the range becomes difficult to estimate during summer. This is caused by the fact that the spherical variogram is not fully capable of describing the semi-variance at these shorter accumulation intervals. This is illustrated by an example of a typical summer day (24-8-2006) in Fig. 3.5. The maximum semi-variance is reached at a short range, as could be expected in convective situations. Especially for the 1-hour accumulations (Fig. 3.5b), the number of points in the part of the variogram with distance $<$ range is limited. This is mainly caused by the topology of the rain gauge network that is used in this study. The relative accuracy of the range parameter is hence limited for short ranges. The mean range can be seen to decrease for shorter accumulation intervals in Table. 3.1, which is exactly opposite to the sill. However, the standard deviation is largest at an 8-hour accumulation interval and decreases in both directions.

As the sill is the factor determining the limit and the range the distance at

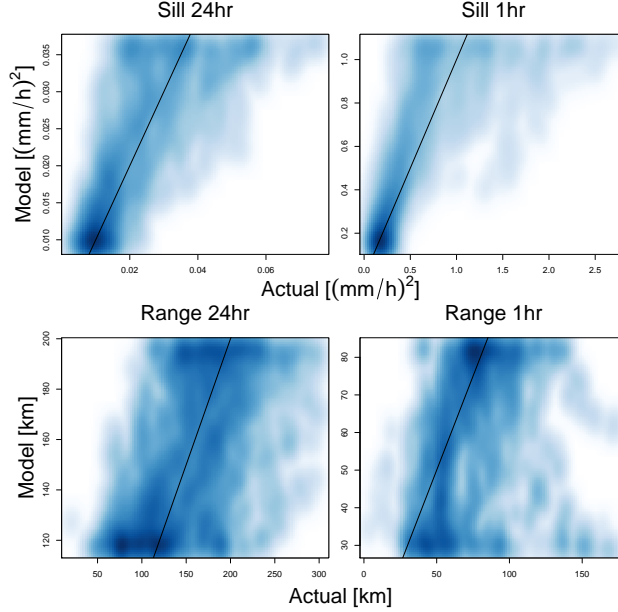


Figure 3.9: Scatterplot of the actual and modeled sill and range for the 30-year data. a) 24 hour accumulation of sill, b) 1 hour accumulation of sill, c) 24 hour accumulation of range, d) 1 hour accumulation of range. The black line is the diagonal line.

which this occurs the RMSE more closely resembles the sill as can be seen in Fig. 3.4c. The mean value of RMSE is nearly 5 times smaller than that of the sill at a 24-hour accumulation interval. This ratio increases to around 3 times smaller at the accumulation interval of 1-hour.

Cosine fit of sill and range

Similar to (*van de Beek et al.*, 2011a) a cosine function is fitted to the sill and range for each time interval, but now expressed in rain rates instead of accumulations. As the sill (Figs. 3.6 and 3.8) and, to a lesser degree, the range (Fig. 3.7) do not quite follow a cosine function, they are transformed using a sqrt-sqrt transform. This transform of the signal of the sill, range and RMSE resembles a cosine much more closely for daily intervals, as was already shown (*van de Beek et al.*, 2011a). A back-transform with a power 4 has to be applied to the cosine function fitted to the transformed signal (see Eq. 3.11) to estimate the actual sill, range and RMSE.

Unlike in the previous Figs. 3.3-3.5 of the sill, range and RMSE, where only the untransformed data were shown Figs. 3.6-3.8 show both the fitted untransformed data and the fitted back-transformed data. In each panel of Figs. 3.6,

Table 3.2: RMSE of the modeled sill $[(\text{mm h}^{-1})^2]$ and range [km] for both the untransformed and transformed variogram parameters seen in Figures 3.6 and 3.7.

	24	12	8	6	4	3	2	1
sill normal	0.00	0.01	0.01	0.01	0.03	0.03	0.06	0.11
sill transform	0.00	0.00	0.01	0.01	0.02	0.02	0.03	0.06
range normal	5.2	4.5	6.5	7.2	7.0	4.4	5.5	6.9
range transform	6.2	4.8	4.9	5.4	5.4	3.1	4.4	5.5

3.7 and 3.8 results for one accumulation interval are plotted, where the black line is the original signal, the blue line the cosine fitted to the untransformed signal (Eq. 3.9), and the red line the back-transformed cosine fitted to the transformed signal (Eq. 3.11), illustrating that the transform that was applied to daily accumulations also works for shorter time intervals. The fit to the sill in Fig. 3.6 is the best for the transformed signal (see Table 3.2). The cosine fitted to the untransformed signal also follows the estimated values well, but has trouble dealing with the asymmetry between the valley and peak, where the valley is much wider than the peak. The sqrt-sqrt transform solves a large part of this problem. The difference between actual sill values and fitted cosine (Eq. 3.11) is also expressed in a scatterplot (Figs. 3.9a and 3.9b). While differences can be quite large most values are close to the diagonal line. Table 3.2 shows the deviations of the modeled ranges and sills expressed as RMSE for each accumulation interval.

The range is more variable than the sill. The deviation from the fitted cosine is stronger and is illustrated in Fig. 3.9c and d. For the range in Fig. 3.7 the transform also has less effect than for the sill, as the signal is already close to a cosine function. With decreasing time intervals the effect becomes larger as the shape of the range signal changes. This is partly caused by the challenge of fitting a spherical variogram to the semi-variance during summer at shorter accumulation intervals mentioned in section 3.5.1. Even though the benefit of the transform for the range is less pronounced than for the sill it reduces the RMSE at accumulation intervals of 8 hours and less as can be seen in Table 3.2. The small difference between the fitted function and the original signal at the 24-hour interval in November-December is caused by the maximum range of 300 km. While some values are beyond this range the values were set to 300 km as the furthest distance pair is at 315 km space (Fig. 3.2). For shorter accumulation intervals this problem does not occur as the range does not reach 300 km anymore.

The shape of the RMSE looks, as mentioned before, similar to the sill and therefor the same applies for the RMSE concerning the fits. As can be seen in Fig. 3.8 the back-transformed cosine-fit of the RMSE follows the actual RMSE closer than the untransformed fit.

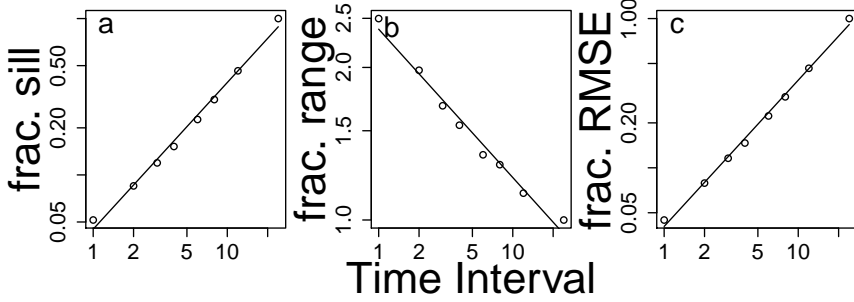


Figure 3.10: a) The mean ratio of the sill of the 24-hour accumulation and other accumulation intervals on logarithmic axes. b) Same but for the range. c) Same but for RMSE

3.5.2 Shape of the semi-variogram at different temporal scales

In this section the resulting fits found in Section 3.5.1 are compared to find common equations to estimate the semi-variance of rainfall at any temporal scale between 1 and 24 hours. In this section we explore two different methods to describe the dependence of the seasonal signal of the variogram parameters on the averaging interval. In Section 3.5.2, ratios of the sill and of the range at sub-daily averaging intervals (1-12 hr) versus the daily interval (24 hr) are considered. The dependence of these ratios on the averaging interval can then be used together with the results of (*van de Beek et al.*, 2011a) for the 24-hr averaging interval to extrapolate semi-variogram parameters for any sub-daily averaging interval. In Section 3.5.2, the parameters of the fitted cosine functions are described as functions of the averaging interval.

Power-law scaling in semi-variogram parameters

As is clear from Fig. 3.4 the seasonal signals of sill and range have similar shapes for all accumulation intervals. However, as was mentioned before, the sill becomes larger and the range becomes smaller for shorter accumulation intervals. As could be expected the mean of ratios changes accordingly with increasing accumulation interval. Fig. 3.10a, b and c show the temporal mean of the ratios of sill, range and RMSE for the 24-hour interval versus all other accumulation intervals, as a function of the accumulation interval, on a logarithmic scale. The mean values used for these analyses can be found in Table 3.1. These 24-hour means are divided subsequently by the means of all other time intervals, which results in a ratio for each time interval.

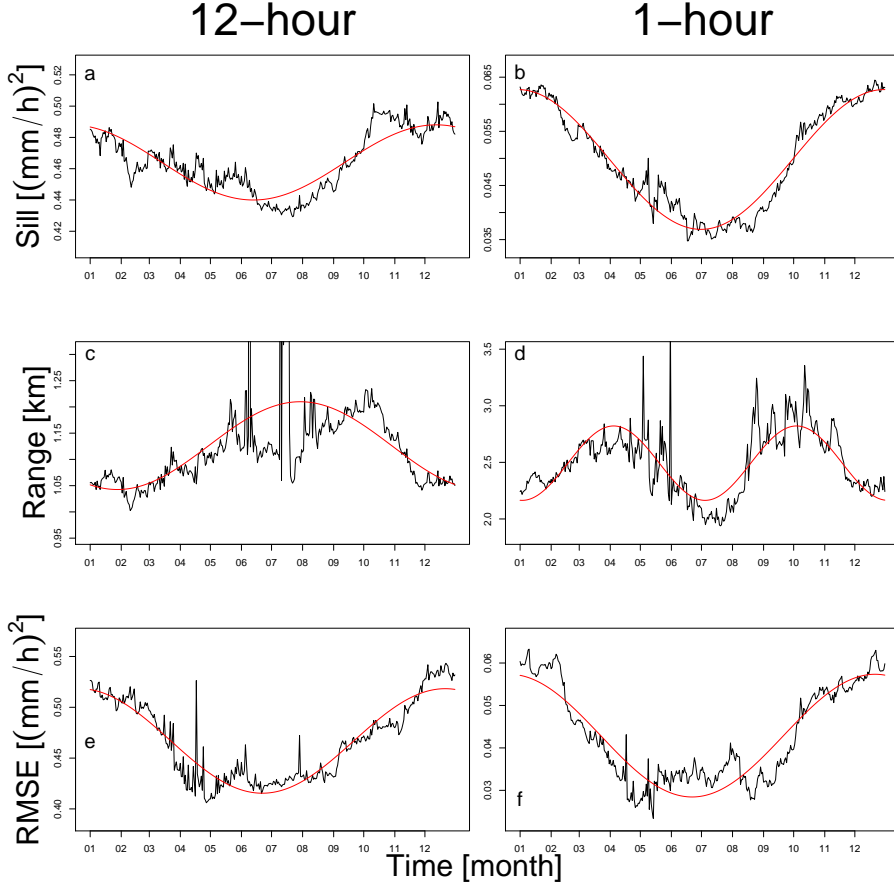


Figure 3.11: Example of the ratio of sills and ranges. a) ratio of daily to 12-hour sill, b) same as a) for 1-hour ratio, c) ratio of daily to 12-hour range, d) same as c) for 1-hour ratio, e) ratio of daily to 12-hour RMSE, f) same as d) for 1-hour ratio. The black lines are the ratios and the red lines the fitted cosines.

$$\text{ratio}_{(interval)} = \frac{\mu_{24hr}}{\mu_{interval}}. \quad (3.12)$$

It is clear from Fig. 3.12 that the relation between the mean variogram parameters and the accumulation interval should be a power law (i.e. a linear relation on logarithmic axes). The values for the parameters of the power-law function $y = ax^b$ can be found in Table 3.3 together with their standard errors, which are small.

As was shown by (*van de Beek et al.*, 2011a) the sill, range and RMSE of

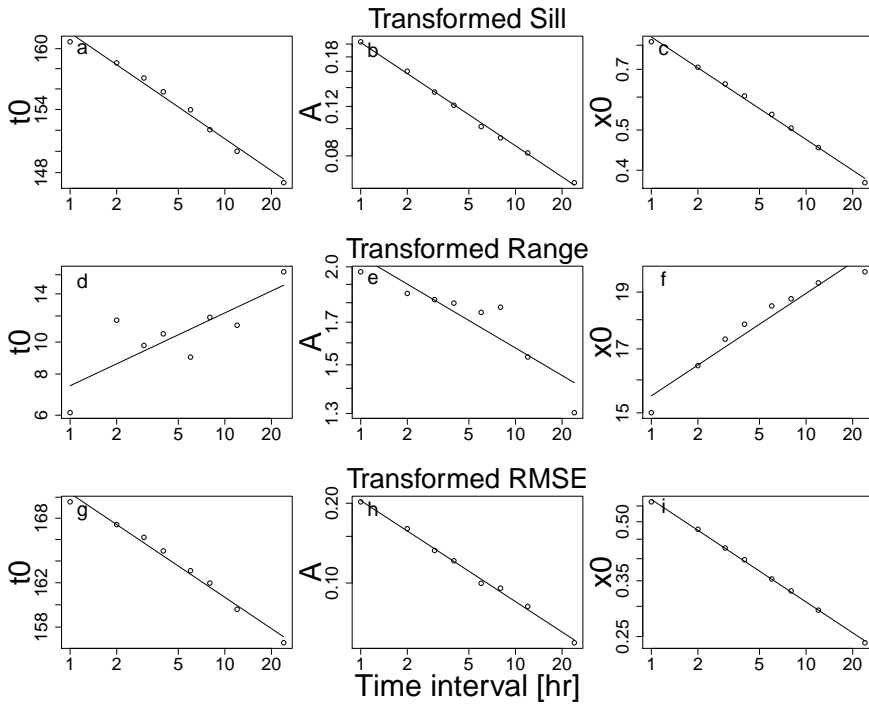


Figure 3.12: Parameters of the fitted cosine functions for the sill, range and RMSE, as functions of the temporal accumulation interval on a logarithmic axes.

Table 3.3: Parameters of the power-law function for the fits in Fig. 3.10, where the 30-year mean of the ratio of the 24-hour sill, range and RMSE with the mean sills, ranges and RMSEs for other time intervals are shown together with their standard error.

	a	b	$STEa$	$STEb$
Sill	0.04	0.94	0.003	0.03
Range	2.38	-0.29	0.03	0.02
RMSE	0.04	0.98	0.002	0.03

the spherical semi-variogram model fitted to the 24-hour accumulation can be described by only a few parameters, which can be seen in Table 3.4. Combining the data from both the fitted cosine for the 24-hour accumulation interval and the fitted power-laws allows for estimation of the semi-variance for each accumulation interval. While these power-laws are evident from log-log linear regressions of the ratios of the mean values against the corresponding interval

Table 3.4: Parameters of the sqrt-sqrt transformed cosine functions for the sill, range and root mean square error of the fitted spherical variograms of the daily rain accumulation of 33 KNMI stations using a 90-day moving average window.

	$1/f$	A	t_0	x_0
range	365	1.3	2	19.8
sill	365	0.3	217	1.8
RMSE	365	0.6	212	2.5

of accumulation (Fig. 3.10), the seasonal shape is more complicated. As can be seen in Fig. 3.11 the problem is illustrated by showing these ratios for each day of year (DOY). As can be seen in Fig. 3.11a and b this ratio of sills is not constant throughout the year. The ratios follow the cosine shapes fairly well and become smoother for shorter accumulation intervals. For the range, however, the signal is much less smooth. Also for smaller accumulation intervals the near constant values during summer yield a different shape than for the longer accumulation intervals. This causes a change of frequency in the cosine function, from once-per-year to twice-per-year. While it would certainly be possible to describe this behavior and the corresponding shape of the semi-variogram for each accumulation interval it would require a larger number of descriptive cosine and power-law functions.

Power-law scaling in cosine function parameters

An alternative way to describe the dependence on accumulation interval is to fit the changing individual parameters for each fitted cosine function. This allows the semi-variogram to be estimated (at any given day of year) for any sub-daily interval of accumulation. The values of the different parameters for the sill are shown in Fig. 3.12. Here the top three panels correspond to a cosine function fitted to the transformed sill. The relations between the A and x_0 on the one hand and the accumulation interval on the other can be seen to be well approximated by power-law relations, if sqrt-sqrt transformed values of the sill are used.

The variation of cosine parameters of the range with accumulation interval can be seen to be less smooth than that of the sill (see Fig. 3.12d-f). In Fig. 3.12e, A is not smooth either, with a deviation for the 6- and 8-hour accumulations from the fitted power-law equation. This is mainly caused by the earlier mentioned problem of the range being nearly constant for a large part of the summer as ranges are shortest. For the shortest time intervals a small increase in the range during the center of the summer period can even be seen. This causes the behaviour of the fitted cosine for intervals of 6-hours and shorter to be different from that at longer accumulation intervals. The signal of x_0 is far more stable and therefore this allows for easy fitting of a function for x_0 .

Table 3.5: Parameters of the power-law functions of the range, sill and RMSE for any time interval between 1 and 24 hours together with their standard errors obtained for the rain rate [mm h⁻¹].

Range				
parameter	a	b	STE a	STE b
t_0	7.37	0.22	0.98	0.07
A	2.06	-0.12	0.09	0.02
x_0	15.51	0.09	0.26	0.01
Sill				
parameter	a	b	STE a	STE b
t_0	162	-0.03	0.40	0.00
A	0.20	-0.37	0.00	0.01
x_0	0.84	-0.25	0.01	0.01
RMSE				
parameter	a	b	STE a	STE b
t_0	170	-0.03	0.38	0.00
A	0.21	-0.39	0.00	0.01
x_0	0.58	-0.28	0.00	0.00

The RMSE is very similar in shape to the sill and therefore the power-law fits are expected to be about as stable. While A for the RMSE deviates slightly more than that of the sill, the power-law fits for t_0 and x_0 are indeed quite good (see Fig. 3.12g-i). This allows again to fit a power-law function through each of the cosine function parameters.

Table 3.5 summarizes the parameters of the power-law fits for sill, range and RMSE, which allows for calculation of the semi-variance for each aggregation time and DOY. Here it is clear that the standard errors in the estimate are small for sill and RMSE, but for range they are larger. This can also be seen for t_0 , where the exponent b is as could be expected close to 0 for the sill and RMSE, but for the range the exponent is larger and most likely a result of larger uncertainty in the range. As the absolute value of t_0 can vary between 1 and 365 and might change on the basis of choosing a cosine or sine function it is sensitive to a power-law fit, where lower values have much greater impact than larger values. This is reflected in Fig. 3.12 where t_0 for the sill and RMSE have values around day 160 and the t_0 for the range is around day 10. This means that the relative difference for the range is larger. Therefore a fit based on a $t_0 = a + b \ln(\Delta t)$ relation might have been better, but a power-law relation still shows no real problem and is more in line with the fitted power-laws for A and x_0 .

Table 3.6: Decorrelation distances found for different time accumulations in different studies.

Paper	Location	Equation
<i>Lebel et al.</i> (1987)	Cevennes	$25\Delta t^{0.30}$
<i>Berne et al.</i> (2004c)	Marseille	$35\Delta t^{0.50}$
Hazenber, 2011, pers. comm.	Ourthe	$70\Delta t^{0.58}$
This chapter	Netherlands (winter)	$70\Delta t^{0.34}$
This chapter	Netherlands (summer)	$40\Delta t^{0.34}$

3.5.3 Decorrelation distance

The parameter values found in this work also allow an estimation of the decorrelation distance. The decorrelation distance is the range of the spherical variogram. The decorrelation distance for the Netherlands is found to be $r_{c,\Delta t} / r_{c,24} = (\Delta t / 24)^{0.34}$ (see Tables 3.1 and 3.3). During winter the $r_{c,24} = 200\text{km}$ and during summer this becomes 120km . This results in a decorrelation distance of $r_c = 70\Delta t^{0.34}$ for winter and $r_c = 40\Delta t^{0.34}$ for summer. These results can be compared to the decorrelation distance found in previous studies. *Lebel et al.* (1987), *Berne et al.* (2004c), and [Hazenber, 2011, pers. comm.] estimated the decorrelation distance as a function of the accumulation interval for different locations in Western Europe. These results are compared to those found in this chapter in Table 3.6.

As could be expected the values can differ with region, but the values found by Hazenber [2011, pers. comm.] for the Ourthe region correspond well with the winter values found for the Netherlands. The shorter decorrelation values found in the other two papers were to be expected as they were found in a more Mediterranean climate, therefore they correspond more with those of the summer situation in the Netherlands.

3.6 Conclusions and recommendations

This chapter has shown that there is a clear relation between seasonal variograms created from rainfall data with different temporal aggregation intervals. Power-law relations between time averages of ratios of variogram parameters for 24-hour and shorter accumulation intervals as functions of rain rates at different accumulation intervals are presented. However, these relations do not capture the seasonal variation of the variogram parameters. This problem is circumvented by describing the parameters of a fitted cosine function (A , t_0 , and x_0) for sill, range, and RMSE for different time intervals using power-law relations. The derived power-law relations for each cosine parameter describe the sill well for any time interval between 1 and 24 hours, but becomes increasingly inaccurate for shorter time intervals. For the range this is more difficult, as both the phase and the amplitude show a fair amount of scatter. With a

good fit through the mean, which is the most important factor for estimating the range, and fairly good fits for the phase and amplitude, the range can be estimated well too. Finally, the RMSE is slightly more difficult to estimate than the sill, but is still well described by power-law relations.

For future research it is recommended to investigate the diurnal change of the shape of the variograms as well. It is expected that the semi-variance will have a strong diurnal cycle during the summer when convective rain tends to fall during late afternoon and evening. Also extending this work in other parts of the world and to larger areas will yield more insight into how rainfall is correlated in space and time. The possible effects of anisotropy and stationarity should be investigated using more extensive (both in extent and density of data points) datasets.

Close-range radar rainfall estimation and error analysis

4.1 Summary

Quantitative precipitation estimation (QPE) using ground-based weather radar is affected by many sources of error. For non-polarimetric radars the most important of these are 1) radar calibration, 2) ground clutter, 3) wet radome attenuation, 4) rain induced attenuation, 5) vertical profile of reflectivity, 6) non-uniform beam filling, and 7) variations in rain drop size distribution. This study presents an attempt to separate and quantify these sources of error in flat terrain. For this purpose, QPE is performed very close to the radar (1-2 km) so that 4), 5), and 6) only play a minor role. Error source 7) can be corrected for because of the availability of two nearby disdrometers. A 3-day rainfall event (25-27 August 2010) that produced more than 50 mm of precipitation in De Bilt, The Netherlands is analyzed using both radar, rain gauge, and disdrometer data.

Without any correction it is found that the radar severely underestimates the total rain amount (by more than 50%). The calibration of the radar is operationally monitored by analyzing the received power from the sun. This turns out to cause 1 dB of underestimation. The clutter filter operationally applied by KNMI is found to filter precipitation as well, especially at near-zero Doppler velocities. An alternative simple clutter removal scheme is used by taking reflectivity values during clear sky situations (clutter map) and subtracting this during precipitation. This improved the rainfall estimation slightly. To investigate the effect of wet radome attenuation, stable returns from build-

ings close to the radar are analyzed. It is shown that this may have caused an underestimation up to 4 dB. Using a disdrometer to derive event-specific $Z - R$ relations, the effect of variability of drop size distributions is shown to cause further underestimation when applying a simple Marshall-Palmer $Z - R$ relation.

Correcting for all of these effects yields a good match between radar QPE and gauge measurements, with a difference of 5 to 8%. This shows that a standard radar rainfall product can be significantly improved near the radar by implementing some simple corrections.

4.2 Introduction

Rainfall is known to be highly variable, both in time and space. Traditional measurements by single rain gauges or networks only provide accurate information of the rainfall at their locations. While interpolation of these data is possible the spatial information is often too sparse for accurate meteorological and hydrological applications (*Berne et al.*, 2004b; *van de Beek et al.*, 2011a,b). While rain gauges are often seen as ‘ground truth’ these instruments also suffer from errors (*Marsalek*, 1981; *Sevruk and Nešpor*, 1998; *Habib et al.*, 2001; *Ciach*, 2003).

Radar, on the other hand, does provide far better coverage in space and often also in time. However, a problem with radar systems is the larger number of error sources, which makes quantitative estimations based solely on radar difficult, unless these error sources are correctly addressed. Error sources that can be identified are radar calibration, clutter, wet radome attenuation, rain-induced attenuation, vertical profile of reflectivity (VPR), non-uniform beam filling (e.g. *Battán*, 1973; *Fabry et al.*, 1992; *Andrieu et al.*, 1997), and errors in derived rain rate from the measured reflectivity due to uncertainties in the drop size distribution (DSD) (*Uijlenhoet et al.*, 2003). These variations in the error sources have been studied and described extensively in the past (e.g., *Zawadzki*, 1984; *Hazenberg et al.*, 2011a).

Clutter results from the main beam or side-lobes (partially) reflecting off objects like buildings or mountains and even insects and birds. Also atmospheric conditions can lead to anomalous propagation (anaprop) resulting in the beam being directed towards the earth’s surface. Close to the radar ground clutter from objects can lead to overestimation of rainfall reflectivities, however, the effect of anaprop is generally limited. In the past many clutter correction schemes have been developed, which reduce the impact of clutter with varying degrees of success (e.g., *Steiner and Smith*, 2002; *Holleman and Beekhuis*, 2005; *Berenguer et al.*, 2005a).

Attenuation of the transmitted signal during a rainfall event can lead to strong underestimation of the rainrate. The amount of attenuation along the path of the transmitted signal is strongly dependent on the rainrate as well as on the transmitted wavelength. X-band radars are relatively inexpensive and easy to install, but suffer quite strongly from attenuation (*van de Beek et al.*,

2010). Radars operating at longer wavelengths, like C-band and S-band, suffer less from attenuation. However, during intense precipitation events C-band radar data also tend to underestimate precipitation rate. Correction for rain-induced attenuation was first proposed by *Hitschfeld and Bordan* (1954). Since then other schemes have been developed that use a path-integrated attenuation constraint (e.g., *Marzoug and Amayenc*, 1994; *Delrieu et al.*, 1997; *Uijlenhoet and Berne*, 2008). Another source of attenuation is caused by precipitation on the radar radome resulting in a liquid film of water. This film attenuates the signal and its effect becomes more pronounced during stronger precipitation intensities. Wet radome attenuation is highly dependent on the wind direction and the state of the radome, as the attenuation depends on whether a film of water can form on the radome (*Germann*, 1999; *Kurri and Huuskonen*, 2008).

Vertical variations in rainfall structure as observed with radar give rise to the so-called vertical profile of reflectivity (VPR). The VPR has an important impact on the measurement characteristics of the radar. Especially for stratiform precipitation, the melting of snow flakes and ice crystals aloft results in relatively large droplets. Within this melting layer region, the returned radar signal intensifies (bright band) leading to an overestimation of the precipitation intensity (e.g., *Andrieu et al.*, 1995; *Vignal et al.*, 2000; *Delrieu et al.*, 2009). However, close to the surface, variations in the VPR tend to be limited. Therefore, close to the radar the effects of VPR can be assumed negligible.

Non-uniform beam filling can also cause significant errors. This effect of course depends on the size of the radar measurement volume and the spatial heterogeneity of the rainfall. Because the relation between radar reflectivity and rainfall intensity is non-linear and not unique (it depends on the drop size distribution), spatial rainfall variability within the radar measurement volume can cause errors (*Fabry et al.*, 1992; *Berne and Uijlenhoet*, 2005a). The same holds for the relation between radar reflectivity and specific attenuation. If correction for path attenuation is applied, this can also lead to errors (*Gosset and Zawadzki*, 2001).

Reflections from precipitation measured by the radar have to be converted to rain rates. This conversion from measured reflectivity values to rain rates at ground level can be quite challenging as rain is highly variable in terms of its drop size distribution (DSD) (e.g., *Yuter et al.*, 2006). The most common way is to convert reflectivity (Z) to rain rate (R) by using a power-law relation, the so-called $Z - R$ relation. This relation was first studied by Marshall and Palmer (*Marshall and Palmer*, 1948), which resulted in the Marshall-Palmer equation (*Marshall et al.*, 1955). To date, this relationship is mostly used to obtain rainfall intensities in stratiform precipitation. Other $Z - R$ relations have been derived as well, more suitable during different types of precipitation and for other locations (e.g., *Battan*, 1973; *Fulton et al.*, 1998; *Uijlenhoet*, 2001; *Uijlenhoet and Berne*, 2008). Optical disdrometers enable one to measure the actual drop size distributions (DSD), from which both Z and R can be inferred. As such, one can obtain the actual $Z - R$ relationship for the event of study at the location of the instrument (e.g., *Löffler-Mang and Joss*, 2000; *Berne and Uijlenhoet*, 2005b; *Hazenberger et al.*, 2011b).

This paper studies the possibilities of quantitative precipitation estimation (QPE) at close ranges for a C-band weather radar operated by the Royal Netherlands Meteorological Institute (KNMI) in the center of the Netherlands. At these distances the effects of VPR, rain-induced attenuation, and non-uniform beam filling are limited and can be ignored, enabling one to study the effects of radar calibration, clutter, wet-radome attenuation and $Z - R$ variability in more detail. Section 4.3 describes the instruments and the data used in this study. Section 4.4 describes the rain event that has been selected. The reflectivity correction methods and their effects are discussed in section 4.5. In section 4.5.4 different $Z - R$ relations are considered and discussed. Finally, in section 4.7 the conclusions and recommendations are presented

4.3 Instruments and data

The precipitation event analyzed in this paper was observed by the radar during the late afternoon on August 25 2010 and lasted for about 2 days. A number of rainfall measurement instruments were available, located at KNMI in de Bilt, the Netherlands, and are used in this paper. These are a rain gauge, two optical disdrometers and an operational C-band Doppler weather radar. The instruments are located on a field south of the radar at KNMI. The instrument locations as well as the radar distance bin that has been used for the comparison are shown in Fig. 4.1.

The employed rain gauge is an automatic gauge with a surface area of $400 \pm 5 \text{ cm}^2$ installed in a pit (*Wauben*, 2004, 2006). The height of the float is measured every 12 seconds with a resolution of 0.001 mm. The gauge can report the precipitation intensity in steps of 0.006 mm h^{-1} . The rain is accumulated and stored at 10 minute intervals, using guidelines set by *Sevruk and Zahlavova* (1994) and *WMO* (1996).

The disdrometers are an OTT Parsivel and a Thies Laser Precipitation Monitor (LPM). They both measure the size and velocity of droplets by the extinction caused by droplets passing through a sheet of light with a surface of around 50 cm^2 . The Parsivel measures particles from 0.2 to 25 mm diameter with velocities between 0.2 and 20 m s^{-1} . The LPM is able to measure particles between 0.16 and 8 mm in diameter and velocities between 0.2 and 20 mm s^{-1} . For both instruments the beam between transmitter and receiver has been oriented perpendicular to the prevailing Southwesterly wind direction in the Netherlands. The data from the disdrometers are logged every minute (*de Haij and Wauben*, 2010).

The radar operated by KNMI is a Doppler C-band radar from SELEX-SI (Meteor AC360). It is located at 52.108N, 5.178E on top of a tower at 44 m above sea level. It operates at 5.6 GHz (wavelength of 5.3 cm). The radar performs a full 14-elevation volume scan (0.3° , 0.4° , 0.8° , 1.1° , 2.0° , 3.0° , 4.5° , 6.0° , 8.0° , 10.0° , 12.0° , 15.0° , 20.0° , and 25.0°) every 5 minutes. The resolution is 1° in azimuth and 1 km in range for the lowest 5 elevations. Elevations 6-14 have a range resolution of 0.5 km. For details about the radar and the scan

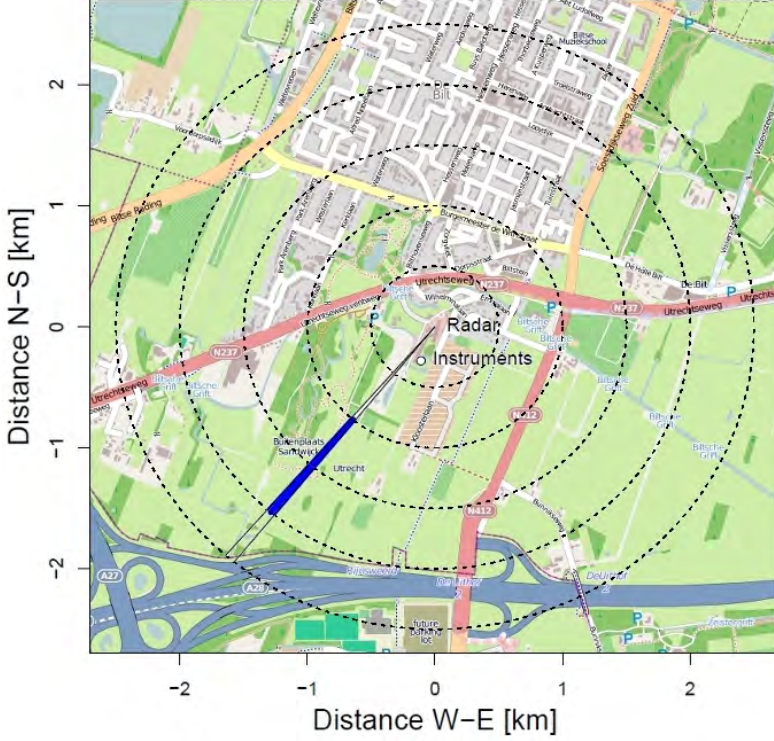


Figure 4.1: Locations of the rain gauge, disdrometers and radar at de Bilt. The blue section is the 1 to 2 km radar bin that is used in this study. Data by OpenStreetMap.org contributors under CC BY-SA 2.0 license.

schedule, see *Beekhuis and Holleman* (2008). For this study the first distance bin from 1 to 2 km at a direction of 230° with respect to the north is used. This bin is located a relatively close distance from the instrument, suffers little from clutter, and is not affected by the transmit/receive mode switching of the receiver (as opposed to the first range bin). In order to improve comparisons between all elevations, the two range bins between 1 and 2 km are averaged for elevations 6-14 to attain a 1 kilometer resolution at each elevation.

Another bin at 3 km from the radar in the same direction contains strong clutter due to several high buildings and is used for a wet radome correction as will be explained in the next sections.

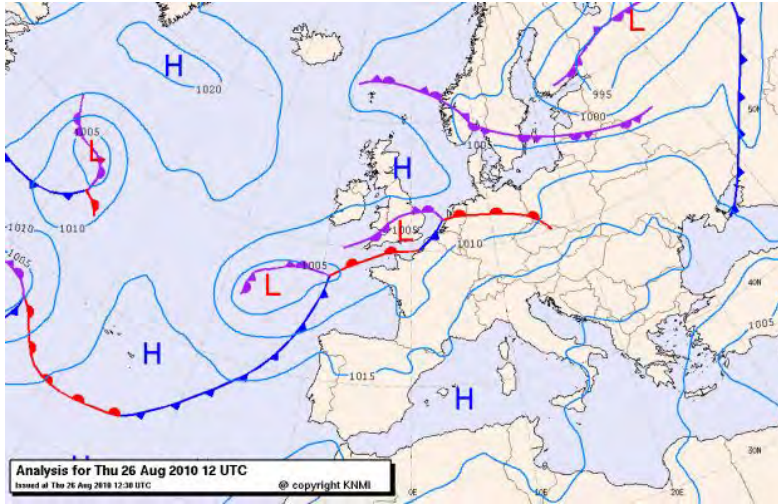


Figure 4.2: Synoptic situation for 26 August 2010 12 UTC (source: KNMI).

Table 4.1: Daily precipitation sum and duration between 25 and 27 August. The total precipitation is slightly larger than measured for this event as the duration of the event starts in the afternoon of the 25th and is not an accumulation of the full day.

	De Bilt		Hupsel	
	mm	duration	mm	duration
25 Aug	6.4	5.7	1.6	3.0
26 Aug	50.6	18.3	142.3	19.5
27 Aug	3.0	5.5	14.6	4.5
total	60.0	29.5	158.5	27.0

4.4 Description of the rain event

Between 25 and 27 August 2010 a narrow band of low pressure passed over the Netherlands from the direction of the English Channel towards southern Denmark between high pressure zones over southern Europe and Scotland. During 26 August the triple point remained near the southern coast of the Netherlands for most of the day with the warm front moving very slowly northward. This caused large temperature differences in the Netherlands between the north, with cold air, and in the south, with warmer air behind the warm front. During the afternoon of the 26th the low pressure zone began moving eastwards leading to quieter weather (see Fig. 4.2).

During the passage of these low pressure areas a mesoscale convective sys-

tem containing large fields of alternatively stratiform and convective precipitation passed over the Netherlands. This lead to both large precipitation amounts and long durations for most of the Netherlands. Table 4.1 illustrates the amounts and durations for de Bilt, where the radar and instruments are located, and for Hupsel, located in the east of the Netherlands. At Hupsel an extremely large amount of precipitation of over 140 mm within 24 hours was measured for this event (see *Brauer et al.*, 2011). At de Bilt the precipitation sum was less, but still considerable, with 50.6 mm over a period of 18.3 hours of continuous rain.

The time series of precipitation is shown in the left panel of Fig. 4.3 and in Fig. 4.4. There is no precipitation until the late afternoon on the 25th. A long period of rain can be seen to occur over De Bilt with low to moderate rain rates (episode 1 in Fig. 4.3). The highest intensity core passes mostly south of the radar and is not analyzed in this study. After a short dry period more precipitation passes over the radar with variable intensities. This period has been subdivided into two phases. First with moderate intensities of around 5 mm h^{-1} (episode 2 in Fig. 4.3), and second one containing heavier rainfall rates up to 25 mm h^{-1} (episode 3 in Fig. 4.3). The large peak in episode 4 was the edge of an active squall line that began to form south of the radar and was advected eastwards, which caused high precipitation sums near Hupsel (*Brauer et al.*, 2011). For episodes 5 to 8 rain intensities decreased within the trailing part of the squall line, resulting in sporadic rainfall measurements observed close to the radar.

The total accumulations are shown in the right-hand panel of Fig. 4.3. The two disdrometers and gauge are closely correlated, but the radar clearly underestimates rainfall accumulations. In the next section possible error sources are identified and corrected as good as possible.

4.5 Methodology and assessment

In this section various error sources and their impact on the measurements by the radar are studied. As described in the introduction the identified sources of error are rain-induced attenuation, VPR, calibration, ground clutter, and wet radome attenuation. However, by focusing on the measurement possibilities close to the radar, the impact of rain-induced attenuation and VPR are expected to be negligible. Therefore, in the current section more specifically the effects of corrections for calibration, clutter and wet-radome attenuation are analyzed.

4.5.1 Calibration

The first error source that can have an impact on the rainfall measurement capabilities of the radar is the absolute calibration (*Ulbrich and Lee*, 1999; *Serran et al.*, 2000). Both the sensitivity of the receiver and the alignment of the radar can be monitored by using the sun. The emitted signal from the sun is easily

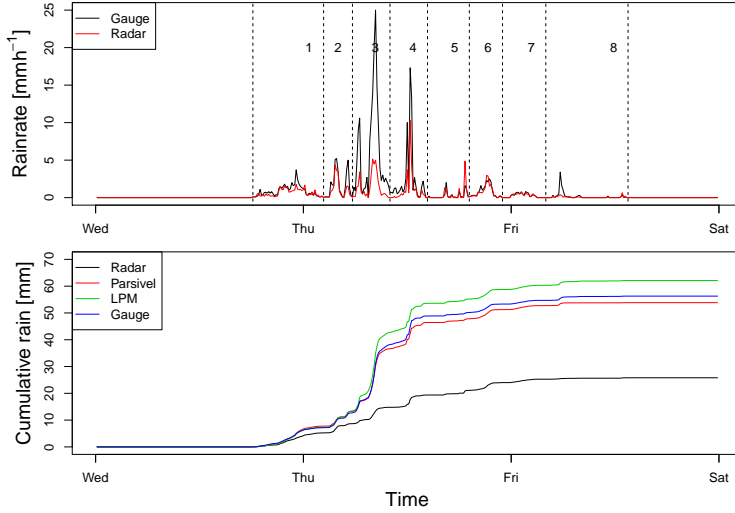


Figure 4.3: Left panel: time series of the rain event with the rain rate from the rain gauge in black and in red the rain rate derived from the radar reflectivity using the Marshall-Palmer $Z - R$ (MP) relation. The vertical dashed lines divide the event into 8 different episodes. Right panel: Cumulative sum of rainfall from the four instruments before any correction of the radar and using the MP relation

detectable by the radar as it is constant over all range bins. This signal can then be used to monitor the absolute calibration of the radar. This method is used operationally by KNMI (*Holleman and Beekhuis, 2004*). Analyses show that the overall calibration was too low and resulted in an underestimation by the radar of up to one dB for the event studied here. Therefore, the volumetric radar data are incremented by 1 dB to account for the impact of radar calibration errors.

4.5.2 Clutter correction

Clutter is operationally removed using a Doppler filter. Unfortunately, this automatic procedure can cause part of the precipitation to be filtered as well (e.g. *Hubbert et al., 2009*), which can lead to an underestimation of rainfall intensities as measured by the radar. An alternative simple method which can be applied to identify and correct for clutter is to determine the average reflectivity signal before precipitation occurs and to subtract this from the signal during rain events. This method (clutter map) will not remove all clutter, however, it also leads to less precipitation to be identified as clutter.

Fig. 4.5 illustrates the effect of the operational clutter removal scheme and

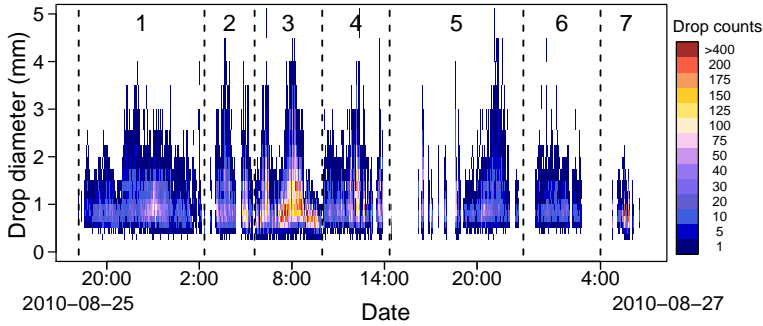


Figure 4.4: DSD during the rain event. The black dashed lines illustrate the identified rain episodes of the event.

the simple static clutter removal method. In the top-left panel the raw uncorrected reflectivity values are shown in black. As can be seen the reflectivity values are around 15.6 dBZ during clear sky situations (dashed red line). Subtraction of the mean value of Z (i.e. not dBZ) from the uncorrected reflectivity results in the simple static clutter removal (blue line). This has the greatest impact for low reflectivities, with none or very little rain. In the top-right panel of Fig. 4.5 the cumulative rainfall sums are shown for both rain gauge and radar rainfall (using the M-P relation) data. Radar accumulations are shown without clutter correction, and after applying either a Doppler (operational) or static clutter correction method (all after application of the 1 dB calibration correction). As expected, the uncorrected radar reflectivities are highest as no clutter has been removed. Of the two clutter correction schemes, the Doppler scheme clearly removes part of the rainfall, whereas the static scheme is more conservative. Therefore, the static clutter correction scheme is used in the remainder of this paper.

In the bottom panel of Fig. 4.5 the time series of the Doppler and static clutter corrected radar derived rain rates are shown together with those of the rain gauge. As expected, the static clutter corrected time series shows higher peaks than those of the Doppler corrected time series and is generally closer to the rain gauge measurements. The small dip that is present in the peak of the Doppler corrected rain rate with very heavy rain in episode 4 of Fig. 4.5 disappears in the static clutter corrected time series. This is a good illustration of the Doppler clutter removal scheme being too sensitive at times. There are a few exceptions to the underestimation by the radar, most notably the two highest peaks in episode 5 where the radar actually overestimates the rain rate compared to the rain gauge. A possible cause might be that the studied range bin lies further south than the other instruments, located at the measurement field of KNMI, and most of the strongest precipitation passed just south of the radar, especially during the formation of the squall line at the end of the rain event.

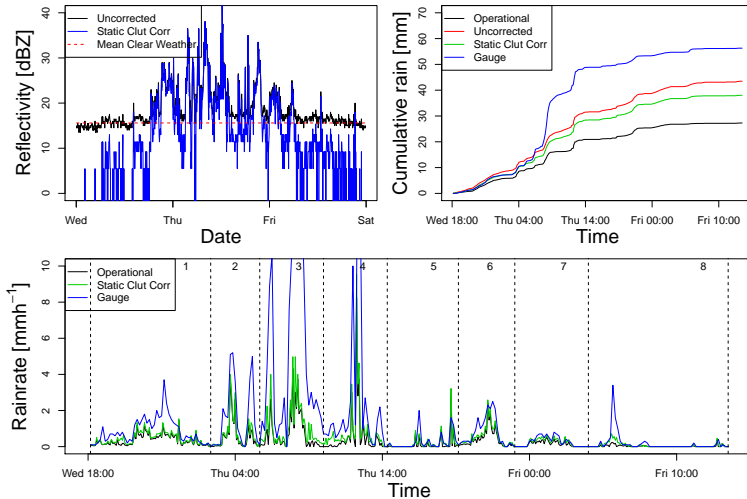


Figure 4.5: Top left panel: Reflectivity of the studied range bin between 1 and 2 km from the radar of the uncorrected reflectivity (black) and the static clutter corrected reflectivity (blue). Here the red dashed line is the average reflectivity when there is no rain. Top right panel: The cumulative rain sums for the rain gauge (blue) and the Doppler clutter corrected (black), together with the uncorrected (red) and the static clutter corrected reflectivity (green) using the Marshall-Palmer $Z - R$ relation with 1 dB added to compensate for calibration errors. Bottom panel: Time series of the rain gauge, Doppler clutter corrected and the static clutter corrected rain rates.

4.5.3 Wet radome attenuation

Since this paper deals with radar rainfall estimation at close ranges, for such events it is highly likely to rain on the radar as well. The resulting formation of a thin layer of water on top of the radome causes significant attenuation of the transmitted signal, which needs to be corrected. To perform this correction, usage is made of the strong clutter pixel observed close to the radar. Due to its proximity the rain-induced attenuation is assumed negligible. Drops in the measured reflectivity value of this static clutter pixel during a precipitation event are assumed to result from the wetting of the radome. While the wetting of the clutter object and precipitation at the clutter location also influences the measured reflectivity, these factors are assumed to be much smaller than the effect of the wetting of the radome.

Fig. 4.6 presents the impact of wet radome attenuation on the measurement capabilities of the radar. The top left panel shows the measured reflectivity from the clutter pixel at a range between 3 and 4 km from the radar. The

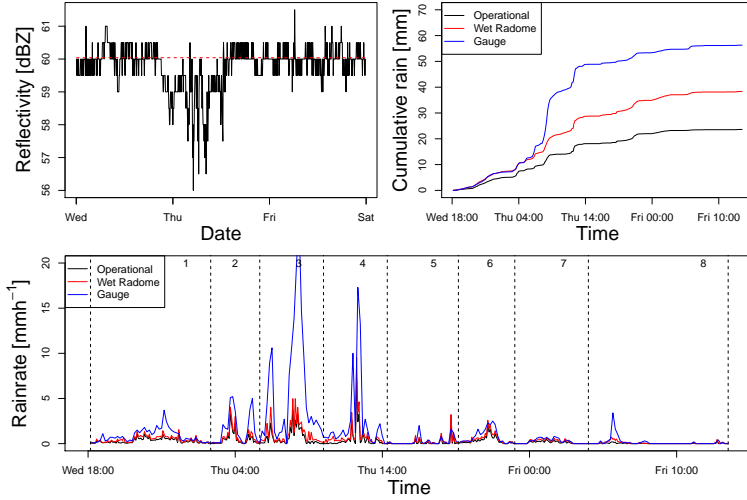


Figure 4.6: Top-left panel: Reflectivity of a strongly reflective clutter pixel near the radar. Here the red dashed line is the average reflectivity when there is no rain. Top right panel: The cumulative rain for the rain gauge (blue), the Doppler clutter corrected (black) and the wet-radome attenuation corrected rain rate using the Marshall-Palmer $Z - R$ relation using the static clutter and calibration corrected data (red). Bottom panel: Time series of the rain gauge, KNMI clutter corrected and the wet-radome attenuation corrected rain rates.

dashed red line presents the average reflectivity during dry periods. The reflectivity can be seen to fluctuate by about 0.5 dB around this mean reflectivity, however a larger drop in measured reflectivity values can be observed at the onset of the event in the late afternoon on 25 August. The difference between the average dry and observed reflectivity values is assumed to represent the impact of wet radome attenuation, which reaches its greatest value during the peak of very heavy rainfall. After having corrected for calibration error and clutter, impact of wet-radome attenuation correction is shown in the top right panel. As could be expected the correction of the attenuated radar reflectivity results in a larger estimated rain rate, closer to that of the rain gauge.

4.5.4 $Z - R$ relations

The corrections discussed in Section 4.5 enhance the radar reflectivity estimates. Figure 4.7 compares the reflectivity measurements of the radar to those inferred from the disdrometer. The corrections clearly have a positive impact, especially for high values of reflectivity (left panel of Fig. 4.7). If the MP $Z - R$

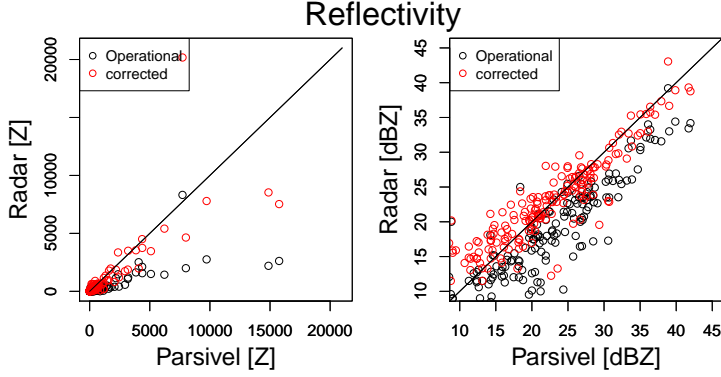


Figure 4.7: Left panel: Reflectivity (Z) measured by the radar and derived from the Parsivel where the black circles are the operationally corrected values and the red circles the fully corrected data described in this paper. Right panel: same as left panel but on a logarithmic scale.

relation is used, the accumulated rainfall increases from 25.8 mm for the uncorrected data to 47.1 mm after applying the corrections for calibration error, ground clutter and wet-radome attenuation (see Fig. 4.6). While this is still below the accumulated rain sum of 56.3 mm for the rain gauge the net effect is considerable. Since the current precipitation event was highly variable in space and time, the applied M-P relationship is expected not to be suitable since it is representative for stratiform precipitation conditions. Therefore, further improvements in the quality of the rainfall estimates by radar can be obtained using the $Z-R$ relationship inferred from the disdrometer measurements. However, a $Z-R$ relation inferred from the disdrometers can be expected to be different than one found from the radar at the same time due to differences in sampling. The disdrometers measure Z over an average of one minute over a small surface at 500 m from the radar. The radar measures the reflectivity of a volume in the air at a distance of 1 to 2 km instantaneously.

$Z-R$ relation derivation

Both the radar reflectivity Z [$\text{mm}^6 \text{m}^{-3}$] and the precipitation intensity R [mm h^{-1}] can be expressed as integral variables of the raindrop size distribution $N(D)$ [$\text{mm}^{-1} \text{m}^{-3}$], where

$$Z = \frac{10^6 \lambda^4}{\pi^5 |K|^2} \int_0^\infty \sigma_B(D) N(D) dD, \quad (4.1)$$

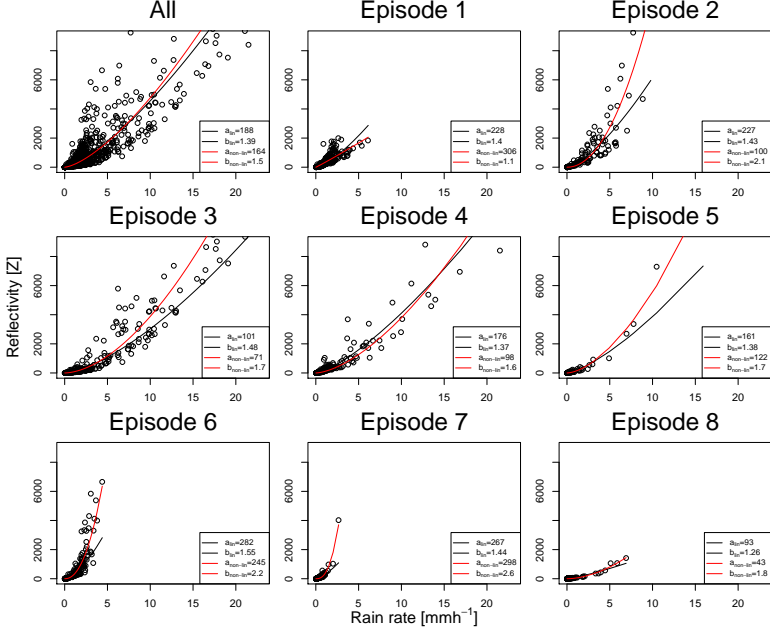


Figure 4.8: $Z - R$ relations derived from the one-minute data of the Parsivel for the different rainfall episodes distinguished in Fig. 4.3 using linear regression on the logarithmic values (black curves) and non-linear regression (red curves).

and

$$R = 6\pi \times 10^{-4} \int_0^{\infty} D^3 v(D) N(D) dD. \quad (4.2)$$

Here, λ [cm] is the wavelength at which the radar operates, σ_B [cm²] is the backscattering cross-section (usually expressed as the sixth moment of the diameter D^6), and v [m s⁻¹] is the terminal raindrop fall velocity. As such, both Z and R are functions of the DSD.

However in practice, the relation between radar reflectivity and rainfall intensity is expressed as a power-law function *Battan* (1973):

$$Z = aR^b \quad (4.3)$$

The most commonly used expression of such $Z - R$ power-law is the Marshall-Palmer relation with $a = 200$ and $b = 1.6$ (*Marshall et al.*, 1955) for stratiform precipitation. This power-law function is applied by many weather services

even though the drop size distribution can vary greatly per event. The presence of 2 disdrometers near the C-band radar at KNMI offers a way of deriving $Z - R$ relations for the rainfall event studied here as they can both provide Z and R values. The Parsivel is analyzed in more detail as it produces rain accumulations closer to the rain gauge measurements than the LPM.

In Fig. 4.8 the $Z - R$ relationships which are obtained from the one-minute disdrometer data for each of the identified episodes are presented. Two different fits have been performed. First linear regression was applied on $\log(Z)$ and $\log(R)$, while as a second approach the fit was obtained using a non-linear power-law fit through Z and R . The former procedure tends to give more weight to smaller rainfall intensities. As expected and seen from the figures, the applied fitting technique has a large impact on the estimated values of a and b . As non-linear fits do not give such large weight to low values, their estimates of a and b are used in the remainder of this study. The $Z - R$ relation varies greatly between episodes. During episode 1 a clear split in data points is visible suggesting that two $Z - R$ relations would perform better. However, from in depth analysis of both the radar CAPPI images as well as the DSD data (see Fig. 4.4), it is difficult to distinguish this split. Therefore, this episode is treated as a single intra event period. The other episodes all behave more uniform, even though some episodes show more scatter than others.

The non-linear power-law fits, together with the Marshall-Palmer $Z - R$ relation are shown in the left panel of Fig. 4.9. For the current rainfall event, the optimal $Z - R$ relationship varies considerably between the different episodes. As expected, the Marshall-Palmer relation is not representative for any of the eight episodes, leading to an underestimation of the rain rate. Especially the $Z - R$ relations found for episodes 3 and 4 are very similar and give much higher rain rate estimates than MP. As these two episodes contain the rain with the highest intensities this has a strong effect on the total accumulated rainfall. Only during three episodes the Marshall-Palmer relationship overestimates the amount of rainfall. Episodes 6 and 7 produce much less rain than would be expected using the Marshall-Palmer relation (MP), while episode 2 yields slightly less rain compared to MP for higher reflectivities. These fits illustrate the high variability of precipitation in time. The Marshall-Palmer relation is derived for stratiform situations. When looking in more detail within a single precipitation event this relation can be found to vary considerably, especially when it evolves from stratiform to convective precipitation.

Application of $Z - R$ relations

The results of applying the derived $Z - R$ relations are shown in the right panel of Fig. 4.9. In this figure three different approaches have been applied. First, the Marshall-Palmer relationship is used (similar to figure 4.6). As a second approach, the event based $Z - R$ relation obtained from all Z and R data collected by the Parsivel during this event (Figure 4.8 topleft). Using a single representative $Z - R$ relationship leads to considerably more precipitation (59.6 mm) than MP (47.1 mm). This increase in precipitation leads to an

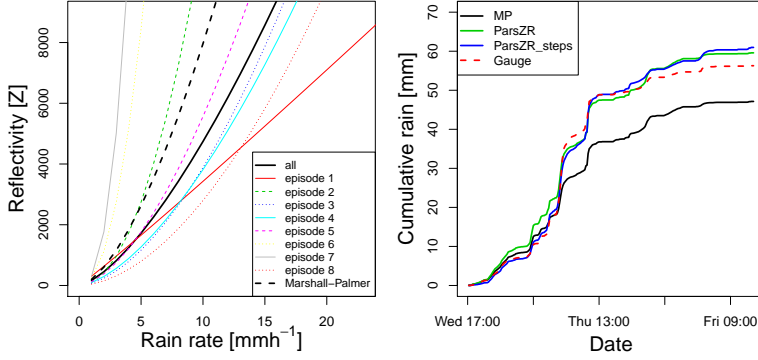


Figure 4.9: Left panel: All non-linear fits together with the Marshall-Palmer $Z - R$ relation. Right panel: Accumulated rain for different $Z - R$ relations applied to reflectivity data that are corrected for calibration, static clutter, and wet radome attenuation.

overestimation of about 6% in total accumulation as compared to the nearby rain gauge. As a third procedure, the eight individual, optimal intra-event power-law relationships were applied as well. This leads to a total precipitation accumulation of 61.0 mm. This final method gives an estimate of the total rainfall, which is 1.8% lower than that measured by the LPM and 8.3% higher than found by the rain gauge.

4.6 Discussion

Table 4.2 illustrates some statistics of possible combinations of corrections. The sum is the accumulated rain sum found from the different radar corrections. The bias is found from the average of the difference between the 10-minute rain accumulation from the rain gauge minus that found from the radar. The standard deviation (SD) is found from this same difference as used for the bias. Finally the percentage is the relative difference of the estimated rain sums compared to the rain gauge (56.3 mm). From this table it can be observed that the operational product (applied MP and Doppler corrected clutter filter) gives rise to a large underestimation by the radar and the worst performance. Not performing any kind of clutter correction, leads to better results as compared to the operational product, both in total rainfall, standard deviation as well as bias. If a wet-radome correction is applied to the static clutter corrected images all statistics improve and the difference between rain gauge and radar decreases from 38.8 to 16.3%. By converting the corrected reflectivity data using the Parsivel inferred $Z - R$ relation further improvements in the quality of the radar product are obtained. Now the differences become very small,

Table 4.2: Rainfall sum [mm] from the radar together with bias [mm h⁻¹], standard deviation (SD) [mm h⁻¹] and percentage from the relative difference between the rain gauge and the radar for different correction combinations from the 10-minute averaged rain sums. Here ‘Operational’ means the Operational Doppler clutter corrected data, ‘raw’ means the uncorrected data and ‘static’ the static clutter corrected data and ‘wet’ the wet-radome corrected data. ‘MP’ is the rain rate derived using the Marshall-Palmer equation. ‘Pars’ means rain rate derived using the $Z - R$ relation found from all data of the Parsivel. Finally ‘Pars-steps’ is the same, but for all episodes of the event the derived $Z - R$ values are used.

	Sum	Bias	SD	%
MP Operational	25.8	0.07	0.29	-54.1
MP raw	39.0	0.04	0.27	-30.8
MP static	34.5	0.05	0.27	-38.8
MP wet+static	47.1	0.02	0.21	-16.3
ParsZR wet+static	59.6	-0.01	0.18	5.9
ParsZR-steps wet+static	61.0	-0.01	0.16	8.3

both in terms of bias and standard deviation. This is also apparent from the difference in rainfall accumulations. While the radar now slightly overestimates the gauge this value is much closer to the rainfall accumulation than when using MP. Finally, the use of a different Parsivel-derived $Z - R$ relation for each episode gives a larger overestimation compared to the rain gauge, but the standard deviation is smaller. The final results for both correction methods based on the Parsivel-derived $Z - R$ relations are comparable to the rain gauge and LPM. As the measurement of the radar is a reflectivity of a volume, which is compared to a point measurement at the ground, it was to be expected that final values would not be a perfect match.

4.7 Conclusions and recommendations

In the current study, close-range quantitative precipitation estimation (QPE) by radar was analyzed. By focusing specifically on regions close to the radar, the effect of rain-induced attenuation, VPR, and non-uniform beam filling are expected to be small, allowing to focus on errors due to calibration, clutter, and wet radome attenuation, as well as $Z - R$ variability, specifically. It was found that for this event the operational clutter corrected radar product underestimated the rainfall accumulation by 54.1% compared to the rain gauge using a standard Marshall-Palmer $Z - R$ relation (MP). The operational Doppler clutter filter used by KNMI is shown to filter some of the rain as well. By correcting radar volume data for clutter using a simple static clutter filter the results improve and the underestimation reduces to 38.8% using MP. Further improvement is obtained when the data are corrected for wet radome atten-

uation by using a stable clutter target close to the radar as reference. These two corrections together with a correction for calibration error give an optimal estimated reflectivity from the radar. Applying MP this resulted in a 16.3% underestimation compared to the rain gauge.

Finally, the $Z - R$ relation was analyzed to investigate if this could improve results. This was done by fitting a power-law function using Z and R values obtained from the Parsivel disdrometer and applying this to the fully corrected radar reflectivities. This resulted in a slight overestimation of 5.9%. Additionally, the event was split up in 8 different episodes based on DSD-data and radar images. A dedicated $Z - R$ relation was derived for each episode, again based on the Parsivel data. Applying these $Z - R$ relations to the fully corrected radar reflectivity data gave a slightly larger overestimation compared to the rain gauge, even though it was still slightly below the measurement from the LPM. The standard deviation of the difference between gauge and radar, found by using a different $Z - R$ relation for each episode, is slightly lower than when applying a single $Z - R$ relation for the entire event.

From these results it can be concluded that a standard radar rainfall product can be greatly improved near the radar by making use of some simple correction techniques. It is shown that using a Doppler clutter filter on all radar pixels causes significant underestimation. An operational algorithm that is more selective in clutter filtering (e.g. CMD, see *Hubbert et al.*, 2009) will likely reduce this problem. The technique used to correct for the wet-radome attenuation can be applied to an entire radar image as long as there is a strong clutter bin near the radar so only attenuation due to wetting of the radome is an issue and not along the path. In a follow-up study it would be interesting to find how much the entire image would benefit from the use of a wet-radome attenuation correction.

Having a disdrometer available to derive $Z - R$ relations for each (part of a) rain event can also improve rain rate estimates from the radar near the disdrometer. While these $Z - R$ relations might be applied to an entire radar image, the benefit of using this compared to a standard Marshall-Palmer $Z - R$ relation or one found from a climatological average using DSD data within the radar area is questionable. Another interesting follow-up study would be to investigate the effect of using a $Z - R$ relation derived from the disdrometer to an entire radar image. The further the distance from the disdrometer the less representative the $Z - R$ relation derived from the disdrometer would become. This correlation would be also of interest to establish for different precipitation types.

Performance of high-resolution X-band radar for rainfall measurement in The Netherlands

5.1 Summary

This study presents an analysis of 195 rainfall events gathered with the X-band weather radar SOLIDAR and a tipping bucket rain gauge network near Delft, The Netherlands, between May 1993 and April 1994. The aim of this chapter is to present a thorough analysis of a climatological dataset using a high spatial (120 m) and temporal (16 s) resolution X-band radar. This makes it a study of the potential for high-resolution rainfall measurements with non-polarimetric X-band radar over flat terrain. An appropriate radar reflectivity - rain rate relation is derived from measurements of raindrop size distributions and compared with radar - rain gauge data. The radar calibration is assessed using a long-term comparison of rain gauge measurements with corresponding radar reflectivities as well as by analyzing the evolution of the stability of ground clutter areas over time. Three different methods for ground clutter correction as well as the effectiveness of forward and backward attenuation correction algorithms have been studied. Five individual rainfall events are discussed in detail to illustrate the strengths and weaknesses of high-resolution X-band radar and the effectiveness of the presented correction methods. X-band radar is found to be able to measure the space-time variation of rainfall

This chapter has been published with minor modifications as: van de Beek, C. Z., Leijse, H., Stricker, J. N. M., Uijlenhoet, R. and Russchenberg, H. W. J., 2010. *Performance of high-resolution X-band radar for rainfall measurement in The Netherlands*, Hydrol. Earth Sys. Sci., 14, 1-17.

at high resolution, far greater than what can be achieved by rain gauge networks or a typical operational C-band weather radar. On the other hand, SOLIDAR can suffer from receiver saturation, wet radome attenuation as well as signal loss along the path. During very strong convective situations the signal can even be lost completely. In combination with several rain gauges for quality control, high resolution X-band radar is considered to be suitable for rainfall monitoring over relatively small (urban) catchments. These results offer great prospects for the new high resolution polarimetric doppler X-band radar IDRA.

5.2 Introduction

Accurate measurement of precipitation in terms of its intensity and location is important for both hydrological research and operational water management. The more traditional method of measuring rainfall with rain gauges is less expensive than weather radar, but only provides point measurements and offers limited information on spatial rainfall variability (e.g., *Ciach*, 2003; *Ciach and Krajewski*, 2006). Other instruments such as disdrometers (*Joss and Waldvogel*, 1969) and microwave links (*Leijnse et al.*, 2007a,b) provide more insight in the microstructure and the spatial average, respectively, of precipitation. However, these instruments cannot capture the spatial variability of rainfall over larger areas such as river catchments. Radar systems offer a way of measuring areal precipitation with both a high spatial and temporal resolution and therefore currently offer the best solution to measure this spatial variability.

The spatial resolution offered by radar systems can range from tens of meters for ground-based research radars up to several kilometers for space-borne systems, whereas the temporal resolution can range from seconds to days. C-band and S-band radars are more commonly used for operational precipitation measurements as these systems do not suffer as strongly from attenuation as radar systems with shorter wavelengths. Although X-band radars suffer more strongly from attenuation, they have the advantage of being able to measure at high spatial resolutions with only small antennas. This makes X-band radar an affordable system for measuring rainfall at high spatial and temporal resolutions over distances where attenuation is not yet a major factor (e.g., *Berne and Uijlenhoet*, 2006; *Uijlenhoet and Berne*, 2008). As a result, this type of radar has recently received more attention in disciplines such as meteorology, (urban) hydrology and quantitative water management. While many radar systems only measure reflectivity, a growing number is capable of doppler and polarimetric measurements allowing far greater insight into precipitation (*Bringing and Chandrasekar*, 2001).

Before data gathered by radar systems can be routinely used for hydrologic applications it is necessary to correct for different types of error sources, which have been studied extensively in the past (e.g., *Zawadzki*, 1984; *Austin*, 1987; *Joss and Lee*, 1995; *Sánchez-Diezma et al.*, 2001). The main error sources that need to be addressed are possible calibration errors, ground clutter and the effects of attenuation. While there are other possible error sources, e.g. Verti-

cal Profile of Reflectivity and bright band, they are negligible for this weather radar as it measures close to the ground (less than 500 m). The conversion from measured reflectivity values (Z) to rain rates at ground level (R) is another important step before radar data can actually be employed for research purposes or in operational hydrologic models. The most important ingredient of this conversion is a power-law Z - R relation (e.g., *Marshall and Palmer*, 1948; *Marshall et al.*, 1955), with coefficients that depend on the type of rainfall and the climatic setting (*Battán*, 1973; *Uijlenhoet*, 2001, 2008).

After identifying and correcting for a possible drift in radar calibration, non-precipitating echoes (so-called clutter) need to be identified and removed from the radar image. In this study a non-polarimetric radar (measuring reflectivities only) was employed, making the detection of ground clutter quite difficult. With modern-day polarimetric and/or doppler radar systems (e.g., *Brangi and Chandrasekar*, 2001; *Meischner*, 2004) identifying clutter has become easier, although a complete correction is still not trivial to achieve. Several methods have been proposed over the years to identify and correct for ground clutter. While none can fully remove the effects of clutter, it can be greatly reduced (e.g., *Steiner and Smith*, 2002; *Berenguer et al.*, 2005b; *Unal*, 2009).

At the wavelength at which X-band radars operate attenuation is another major factor causing erroneous rainfall estimates. This was already recognized in the early days of weather radar (e.g., *Ryde*, 1946; *Atlas and Banks*, 1951). Attenuation occurs both due to rainfall on the radar (wet radome attenuation) and along the beam path (Path Integrated Attenuation, PIA). The first method of correcting for attenuation was proposed by *Hitschfeld and Bordan* (1954) and is now generally known as the Hitschfeld-Bordan forward correction scheme. Due to the reduced cost of S- or C-band weather radars attention was moved from X-band to these systems during the 1970s and 1980s. However, with the launch of the TRMM satellite (*Simpson et al.*, 1988) in 1997 and the CASA project, where a complementary X-band radar network is being proposed (*Chandrasekar and Lim*, 2008), better attenuation correction schemes have become of major interest and new research into X-band radar has begun. Where *Hitschfeld and Bordan* (1954) proposed a simple forward scheme to correct for attenuation, more sophisticated backward methods, which use a Path Integrated Attenuation constraint, have been developed since (e.g., *Marzoug and Amayenc*, 1994; *Delrieu et al.*, 1997).

With the recent installation of a new X-band radar, IDRA (*Figueras i Ventura and Russchenberg*, 2007, 2008), at the Cabauw Experimental Site for Atmospheric Research (CESAR) in The Netherlands (*Russchenberg et al.*, 2005; *Apituley et al.*, 2008), this study presents the analysis of a multi-year data set gathered with its predecessor, SOLIDAR. The aim is to find the strengths and weaknesses of X-band radar under conditions typical for The Netherlands using a large dataset consisting of 195 events and try to deal with the weaknesses in a straightforward way. Even though the proposed methodology is applied to an X-band radar over a surface with little height differences, it is generally applicable to any (non-polarimetric) radar system with minor modifications. This can also be considered an exploratory study for future research into the

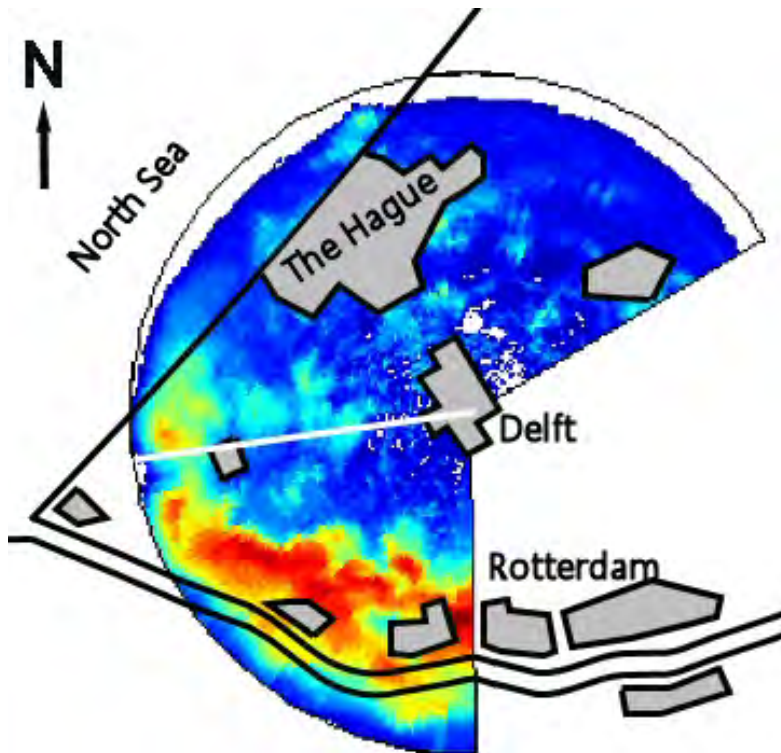


Figure 5.1: Range and coverage of SOLIDAR. The white line indicates the line array of rain gauges, located from 3.75 to 10 km from the radar. Along this path the only significant clutter is present just beyond 6 km, where the beam encounters buildings and greenhouses.

use of X-band radar for ground validation of the upcoming Global Precipitation Mission (GPM) (*Stephens and Kummerov*, 2007) in The Netherlands.

5.3 Data and theory

5.3.1 Radar and gauge data

This study employs data gathered by the X-band FM-CW (Frequency Modulated – Continuous Wave) Solid-State Weather Surveillance Radar, SOLIDAR, which was located on top of the Electrical Engineering building of Delft University of Technology (*Ligthart and Nieuwkerk*, 1990). The data gathered for the purpose of this study were collected over a six year period, from January 1991 until August 1997 (*Uijlenhoet et al.*, 1997). SOLIDAR received a major upgrade in the Winter of 1992–1993. The retrieval algorithm was improved and an additional 8 dB was added to radar reflectivity maps thus greatly improving

Table 5.1: SOLIDAR specifications after processing (from *Ligthart and Nieuwkerk, 1990*).

Characteristic	Value
Centre frequency	9.467 GHz
Beam width	2.8°
Angular resolution	1.875°
Covered sector	240°
Maximum range	15.36 km
Range resolution	120 m
Antenna revolution time	~16 s
Height of radar site	92 m

the quality of the acquired data.

As shown in Table 5.1, the radar had a range resolution of 30 m, which needed to be degraded to 120 m during pre-processing due to data storage constraints. It operated at a single elevation of 1.7° and had a maximum range of 15.36 km at an angular resolution of 1.875°. The temporal resolution was just under 16 s. Due to the location of a second radar on the roof of the same building SOLIDAR could not cover a full 360° circle. This is the cause of the 120° gap which can be seen southeast of the radar in Fig. 5.1.

The instrument was originally designed to measure rain rates of 1 mm h^{-1} up to 100 mm h^{-1} . There is a considerable amount of low intensity clutter present in the data below the 1 mm h^{-1} ($\sim 22.3 \text{ dBZ}$) threshold, but also several individual locations with reflectivities of up to 60 dBZ ($\sim 150 \text{ mm h}^{-1}$), of which the strongest is found nearly due north at 9 km distance. Little information about upgrades and calibration is available, which implies that possible calibration errors have to be found using the available reflectivity data, an assessment of which will be shown in the next section.

The rain gauges in the area covered by the radar were located nearly due west of SOLIDAR, in a line array of 3.75 km up to 10 km from the radar (see Fig. 5.1). The distances of the individual gauges were 3750 m, 5450 m, 6267 m, 7450 m, 8006 m, 8006 m, 8050 m, 8864 m, and 9550 m from the radar. The rain gauges were standard tipping-bucket gauges with a volume resolution of 0.2 mm. These gauges were operated from March 1991 until April 1994. During this time period between one and nine gauges were operational simultaneously.

Motivated by the radar upgrade in the winter of 1992–1993 and the availability of rain gauge measurements until April 1994, the available radar and rain gauge data in the intermediate period have been selected for analysis here, resulting in a dataset of approximately one year of measurements. The storage of the radar data was limited to only reflectivity maps of precipitation events (based on 4 criteria) due to limited storage space. These criteria were based on both the measurements of SOLIDAR and those of 2 radiometers and

4 automatic rain gauges (not belonging to the line array). The criteria where (*Ligthart and Nieuwkerk, 1990*):

1. On a clear day the radiometers yield a noise temperature of around 40 K and during heavy rain 250 K. A threshold of 82 K was set for the detection of rain.
2. One or more of the four rain gauges measure at least a rain rate of 2 mm h^{-1} over a 1-min period.
3. Within the map at least one pixel exceeds a reflectivity value corresponding to 10 mm h^{-1} .
4. At least 5500 of the 16 384 pixels of the entire map exceed a reflectivity corresponding to a 2 mm h^{-1} threshold.

Of these stored data only events with more than 30 min of continuous radar images were selected for this study. These combined selection criteria yielded a total of 195 rainfall events. A visual inspection of these events based on both strength and shape of the measured reflectivity patterns led to a further subdivision of these data into 30 stratiform events, 23 strongly convective events, and a third category of 142 unidentified events.

Finally, a dataset of 446 raindrop size distributions gathered by *Wessels (1972)* in the period between 3 January, 1968 and 13 March, 1969 in The Bilt, The Netherlands has been used to derive relations between reflectivity, rain rate, and attenuation. The Drop Size Distribution (DSD) data was collected using a filter paper technique with an exposure surface of 20 cm^2 . The exposure time was dependent on the period over which Wessels judged the rain to be constant, i.e. rain drop size distribution and intensity. The resulting time intervals are between 1 and 50 min.

5.3.2 Rain rate estimation

To relate the reflectivity (Z) [$\text{mm}^6 \text{ m}^{-3}$] measured by SOLIDAR to the rain rate at the ground (R) [mm h^{-1}] radar theory has to be applied (*Battan, 1973*). The mean power P_r [W] received from reflections by raindrops at a range r [km] can be expressed as

$$\overline{P_r} = C \frac{|K|^2}{r^2} Z_A(r), \quad (5.1)$$

where C is the radar constant, which is a function of radar attributes such as the transmitted wavelength and antenna characteristics, and $|K|^2$ is a coefficient related to the dielectric constant of water (which is approximately 0.93). The attenuated reflectivity Z_A [$\text{mm}^6 \text{ m}^{-3}$] can be expressed as

$$Z_A(r) = Z(r) \exp \left[-\frac{2 \ln(10)}{10} \int_0^r k(s) ds \right], \quad (5.2)$$

where Z [$\text{mm}^6 \text{m}^{-3}$] is the unattenuated reflectivity, and k [dB km^{-1}] the specific, one-way, attenuation. For rain rate retrieval from incoherent, single frequency, non-polarimetric radar measurements, the values of Z , k , and R can be expressed as integrals over the raindrop size distribution $N(D)$ [$\text{mm}^{-1} \text{m}^{-3}$] according to

$$Z = \frac{10^6 \lambda^4}{\pi^5 |K|^2} \int_0^\infty \sigma_B(D) N(D) dD, \quad (5.3)$$

$$k = \frac{1}{\ln 10} \int_0^\infty \sigma_E(D) N(D) dD, \quad (5.4)$$

$$R = 6\pi \times 10^{-4} \int_0^\infty D^3 v(D) N(D) dD, \quad (5.5)$$

where λ [cm] is the wavelength at which the radar operates, σ_B [cm^2] and σ_E [cm^2] are the backscattering and extinction cross-sections, and v [m s^{-1}] is the terminal fall velocity of raindrops.

Using the parameterization proposed by *Beard* (1976) for the raindrop terminal fall velocities and the Mie scattering theory for spherical particles (*van de Hulst*, 1957), values of Z , k and R can be computed from a raindrop size distribution dataset.

5.4 Methodology and assessment

Like any other (X-band) weather radar SOLIDAR may suffer from a possible calibration drift, ground clutter, and wet-radome induced and path-integrated attenuation. Also a conversion from measured reflectivities aloft to rain rates at ground level has to be applied. To assess their impact in terms of rainfall measurement uncertainty and discuss possible correction procedures, each of these issues will be analyzed in more detail in this section. Section 5.5 will illustrate these issues by means of several case studies.

5.4.1 Radar calibration

Many techniques for radar calibration exist (*Stratmann et al.*, 1971; *Joss and Lee*, 1995; *Atlas*, 2002) and have also been described for space-borne and polarimetric radars (*Gage et al.*, 2000; *Gorgucci et al.*, 1992). As original calibration reports are not available for this radar, a possible drift in calibration can be inferred from a long-term comparison of the accumulated rainfall from the radar and the nearest gauge for a large number of events. Figure 5.2 shows the results for cases with more than 1 mm event total for the dataset described in Section 5.3, resulting in 95 events. Here the radar rain rate estimates have been calculated using the theoretical Z - R relation that will be derived in Section 5.4.3. As can be seen in Fig. 5.2b there is no clear trend in the radar

event sums compared to that measured by the gauge, although there are more cases with underestimation than overestimation by the radar. Overestimation by the radar mainly occurs for low rainfall intensities. For intensities exceeding 2 mm h^{-1} the radar underestimates rainfall in nearly all cases.

Another way of finding a possible trend in radar calibration is to look at the average reflectivity of an area affected by strong ground clutter (Fig. 5.3). For this purpose the strongest clutter area in the radar image (nearly due north of the radar at 9 km) was selected. The analysis was limited to all radar images during the period between May 1993 and October 1996 for which more than 2 min of continuous reflectivity data were available. The selected area consists of the 9 pixels in the center this ground clutter area. The data in Fig. 5.3 also seem to suggest a seasonal trend in reflectivity with the highest values around September and lowest around March. As only 3 years of data is available such a seasonal effect is highly uncertain and is therefore ignored for the remainder of this article. As can be seen in Fig. 5.3, the linear regression line through the dots suggests a gradual change in the level of reflectivity over time,

$$\text{dBZ} = 42.86 - 0.0083 \times t, \quad (5.6)$$

where the first term is the offset for the first measurement day on 15 May, 1993, and the second term the decrease in reflectivity level per day beyond this date. Based on this fit, that is based on three and half years of data, the reflectivity data of the 195 events between May 1993 and May 1994 were corrected. Figure 5.2c illustrates the result of this correction applied to the analysis shown previously in Fig. 5.2b. The data now seems to be overcorrected with a slight upward trend even though there is now as much radar overestimation as underestimation. The fact that this correction seems too strong for application during the period of the 195 selected events suggests that the calibration monitoring only occurred until early 1994 and that afterwards calibration drift set in. Hence, while a calibration drift was found, based on the overcompensation shown in Fig. 5.2c it was decided not to apply any correction to the reflectivity data for the 195 selected events.

5.4.2 Ground clutter correction

The next step in creating hydrologically useful rainfall maps is to correct the original data for clutter. Ground clutter occurs when the radar beam is reflected by objects on the ground such as buildings, trees, or mountains. Other types of clutter, such as sea clutter and reflections caused by swarms of insects, birds or airplanes, are also possible. One approach to identify clutter in the reflectivity data is to create a static map of areas where clutter is most prevalent. Another is to create a more dynamic map which identifies clutter from image to image. The problems of ground clutter in reflectivity maps and the associated identification and correction schemes have been extensively described (Aoyagi, 1983; Andrieu *et al.*, 1997; Creutin *et al.*, 1997; Steiner and Smith, 2002; Siggia and Passarelli, 2004; Berenguer *et al.*, 2005b). The more advanced techniques using doppler or polarimetric radar data cannot be applied on the

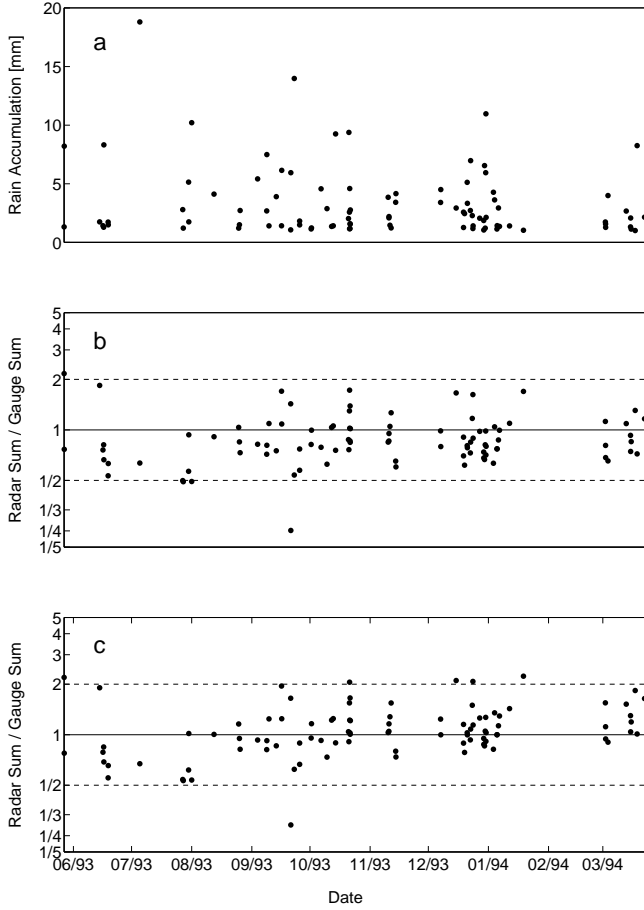


Figure 5.2: **a)** Rainfall accumulations larger than 1 mm of the gauge nearest to the radar (95 events in total). **b)** Ratios of the rainfall accumulations of the radar and the nearest gauge for the same events as in **a)** (the dashed lines indicate a factor 2 over- or underestimation). **c)** Same as **b)** after correction for possible calibration drift.

data gathered by SOLIDAR as only the reflectivity data is available. In this study the ground clutter is therefore identified by creating a static clutter map on a polar grid based on the exceedance of a threshold value for more than 90% of the time for dry events. The selected threshold is 22.3 dBZ, which corresponds to the 1 mm h^{-1} originally given as the minimum detectable signal level for SOLIDAR (*Ligthart and Nieuwkerk, 1990*). Based on this clutter map three correction methods are tested: nearest neighbour, inverse distance, and

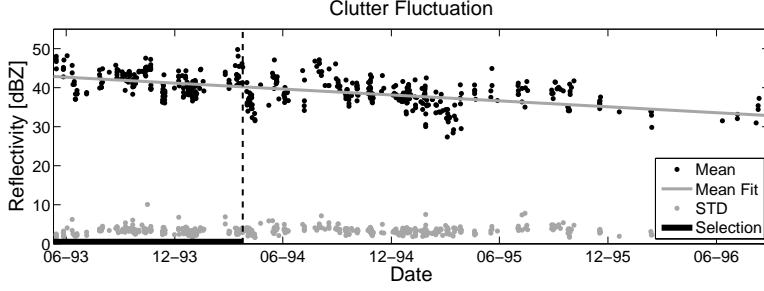


Figure 5.3: The average radar reflectivity and standard deviation of the center 9 pixels of the strongest clutter area (nearly due north of the radar) for all events containing more than 2 min of continuous data between 5 May 1993 and 2 October 1996. Black dots represent the average values per event before correcting for calibration drift. Gray dots are the standard deviations (STD) for the clutter area. The black line is the linear fit through the average values. The period indicated by “Selection” corresponds to the events selected for the radar – rain gauge comparison (Fig. 5.2).

tracking. The methods are applied on a polar grid as the local deformation of the polar grid with respect to the Cartesian grid is minor even though the sizes of the pixels vary with distance on a polar grid. Due to the large amount of data the authors chose to apply the corrections on the polar grid to reduce computer processing time.

The nearest neighbour method compares the identified clutter map to the current radar image with the reflectivity in Z [$\text{mm}^6 \text{m}^{-3}$]. At each location marked as clutter the surrounding pixels that have not been marked as clutter are averaged and taken as value for the clutter location. If the window is not large enough to contain non-clutter pixels the range is extended until 70% of the outer edge of the window contains non-clutter pixels. While the 70% is a fairly arbitrary value it was found to perform well for after testing several cases.

The second method of clutter correction applies the inverse distance method to the clutter area using all points not marked as clutter as reference, using the following equation:

$$Z_i = \frac{\sum_{k=1}^N d_k^{-p} Z_k}{\sum_{k=1}^N d_k^{-p}}, \quad (5.7)$$

where Z_i is reflectivity of the clutter pixel that needs to be corrected, k is the index of the pixel at a distance d_k from the clutter pixel, and p determines the strength of the weights. In this manner each known (precipitation) pixel value is given a weight based on the inverse of the distance to the location of the

unknown (clutter) pixel value. The power p can be given any (positive) value, with larger values giving more weight to values closer to the location of interest. For this study a value of 2 was chosen to give some weight to values closer to the pixel of interest and still not be so large as to approach the nearest neighbor method. The maximum range was set to include only pixels in a range of up to 2 km. This range was chosen to be large enough to ensure that non-clutter reference pixels were included even for larger clutter areas.

For the final method of clutter correction the movement of precipitation is tracked for each pixel. The tracking is done by taking a 5×5 pixel box with the pixel of interest as the center pixel. This window is then moved along a larger 19×19 pixel window in the previous image and the sum of the squared differences for each location is calculated. This results in a 15×15 pixel field with estimated sums of the squared differences. With the selected window size precipitation with a velocity of up to $\sim 190 \text{ km h}^{-1}$ will be included. Therefore it is highly unlikely that any pixel, correctly identified as precipitation, will not be present in the selected window. The shift between the pixel of interest and the pixel with the lowest value of the sum of squared differences for the estimated 15×15 field is then assumed to be the movement for this pixel. As this system is not completely robust, the most common movement in a 5×5 pixel window around the clutter pixel is taken as the true movement for this window. Using this movement the precipitation value from the previous image is used to replace the clutter-affected pixel in the current image.

By marking random pixels as if they represent clutter the effectiveness of the three clutter correction methods can be tested. The test sizes are 1×1 , 3×3 and 5×5 pixels. Figures 5.4 and 5.5 show 9 scatter plots of the corrected reflectivities for the 3 presented correction methods and 3 different clutter area sizes (applied to all cases, representing a total of 51 559 images). From these plots it is clear that the nearest neighbor method gives the best results. The inverse distance method performs worse with larger scatter and lower fitted slope. Finally the tracking method also has a larger amount of scatter along the fitted line than the nearest neighbor method, but does have a fit that remains closer to the 1:1 line even for larger clutter areas.

Similar conclusions can be drawn on the basis of the statistics corresponding to these plots, as shown in Table 5.2. Here the bias represents the mean difference and the RMSE the root mean square difference between the estimated and the measured values. Table 5.2 shows that the bias is lowest for the nearest neighbour method for a clutter area size of one pixel. For larger areas the tracking method actually results in a smaller bias. As mentioned before, this can be seen from the linear fit through the data in Fig. 5.4. The fit remains closer to the 1:1 line for the tracking method for increasing clutter area sizes, even though the scatter is larger for the tracking and the inverse distance methods as compared to the nearest neighbour method. This is also clear from the RMSE-values shown in Table 5.2. The nearest neighbour method has the smallest RMSE for all clutter area sizes, but it increases more rapidly than that of the other two methods. From these results it can be concluded that in general the nearest neighbour method performs better for small clutter areas,

whereas the tracking method might perform better for clutter areas larger than the tested 5×5 pixel area.

Figure 5.5 shows the same results as Fig. 5.4, but the reflectivities have now been converted to rain rates. As expected, the results are similar, although the difference between the linear fits for the nearest neighbor and tracking methods are more pronounced. This is mainly because the logarithmic dBZ-scale has been converted to a linear R -scale, giving increased weight to higher values. Because most clutter areas present in the SOLIDAR images are smaller than 25 pixels, as well as for reasons of computational ease, the nearest neighbor method has been applied in the remainder of this chapter. An example is shown in Fig. 5.6, where Fig. 5.6a is the image before applying the nearest neighbor correction and Fig. 5.6b the image after correction. While some clutter is still visible, the nearest neighbor method has been able to remove most of the clutter. Figure 5.6c and d will be discussed in Section 5.4.4.

5.4.3 Derivation of Z - R relations

The conversion from a reflectivity of a volume in the air, Z , measured by a radar to a rain rate estimate at the ground, R , is difficult. As mentioned in the introduction many studies have been performed to find an answer to this problem (*Marshall and Palmer, 1948; Marshall et al., 1955; Battan, 1973; Uijlenhoet, 2001*). This study uses the dataset of drop size distributions from *Wessels (1972)*, which allows power-law relations between Z and k as well as between Z and R to be established (see Fig. 5.7) using the theory discussed in Section 5.3.2. To estimate the coefficients of these relations $\ln(Z)$ - $\ln(R)$ and $\ln(Z)$ - $\ln(k)$ linear fits as well as a power-law non-linear fits have been established, both using least-squares regression methods. The fits found for both methods are quite different and illustrate the importance of choosing the appropriate fit. In addition, they show that there is a significant amount of uncertainty associated with any fitting procedure. For the purpose of this study, the non-linear power-law fits have been chosen, as they give larger values greater weights. The values found for this theoretical fit were $Z=171R^{1.73}$ and $k=1.04 \times 10^{-4} Z^{0.80}$.

Another way to derive Z - R relations is to directly compare measured radar reflectivities with rain gauge measurements at the ground. In order to do so we have chosen to estimate the average rain rates for both rain gauge and radar per time interval between subsequent tips of the bucket of a gauge. For this purpose the tips of the gauge nearest to the radar (at a distance of 3.75 km) have been compared with the radar pixel directly over the gauge, which yields instantaneous values of Z every 16 s. This gauge was selected as the effect of attenuation will be smallest. In Fig. 5.8 all data is plotted, where the reflectivity values are plotted in dBZ and R is plotted on a logarithmic scale to provide more detail for smaller reflectivity values. The Z - R relation for all data was found to be $Z=59R^{1.94}$ (see Fig. 5.8a). In Fig. 5.8b and c Z - R relations are also plotted for fits based only on convective and stratiform events, which have been selected from visual inspection of all events. This resulted in a Z -

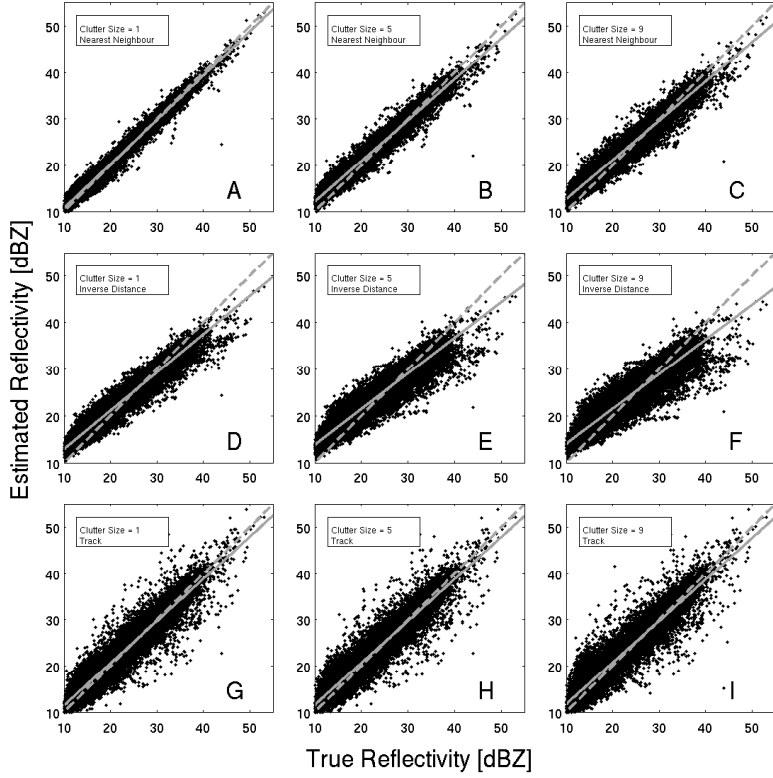


Figure 5.4: Scatter plots of measured reflectivity versus estimated reflectivity. The rows represent the nearest neighbor, inverse distance and tracking methods and the columns 1×1 , 3×3 , and 5×5 pixel clutter areas. The solid lines represent linear fits through the data and the dashed lines are the 1:1 lines.

R relation of $Z=120R^{1.57}$ for stratiform events and $Z=40R^{2.07}$ for convective events. The strongest outliers for the convective cases can be seen for low reflectivity values and high rain rates. This is in line what could be expected for strongly convective events, where signal saturation might occur as well as an attenuated signal due to a wet radome. Most of the low reflectivity outliers at rain rates above 20 mm h^{-1} in Fig. 5.8 can be traced back to a few events during the summer months of 1993, when several high intensity convective events occurred.

The theoretical fit (see Fig. 5.7) is quite different from the fits found based on the radar-gauge comparison and gives lower rain rates than found from the radar-gauge fit, as can be seen from the fitted lines in Fig. 5.8d. In this figure the dash-dotted line is the theoretical fit, the solid line the fit for all cases, the dotted line for convective cases and the dashed line for stratiform cases. The convective fit and the fit for all cases are very similar, as could be expected

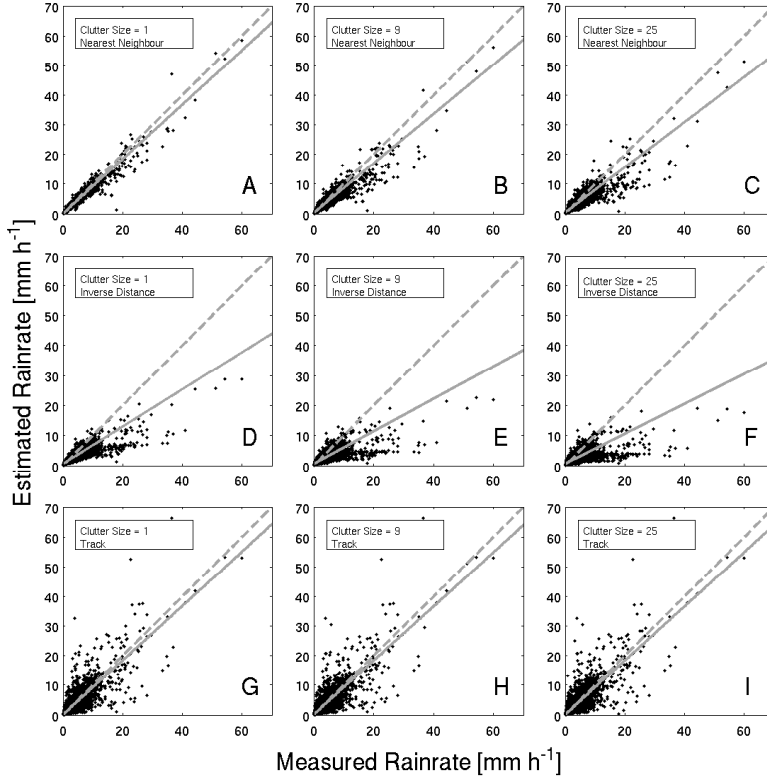


Figure 5.5: Same as Fig. 5.4, but in terms of rain rate.

when looking at the data. Most of the largest scatter occurs with convective events and therefore the most extreme values for all data points are those related to these convective events. The slope of the fitted stratiform relation is steeper than the slopes of the convective and all-event relations. At lower rainfall intensities it does lie closer to the theoretical fit, but beyond 6.5 mm h^{-1} the other fits lie closer to the theoretical fit.

The discrepancy between the raindrop size distribution based fit and the radar-gauge based fits can be attributed to several causes, such as: 1) errors in the collected drop size distribution dataset; 2) limitations in expressing the Z - R relation as a simple power-law function; 3) lack of consistency between point measurements of rainfall at the ground and reflectivities in volumes of the air; 4) radar calibration errors; 5) strong attenuation in convective events causing lower than average Z -values for gauge-measured rain rates. While none of the power-law relations will be universally applicable for every precipitation type, we have chosen to use the theoretical Z - R relation as the errors involved are expected to be smaller than those for the fit found using the radar-gauge comparison. Also, maybe even more importantly, the theoretical fit is independent

Table 5.2: Bias [mm] and RMSE [mm] of the presented clutter correction methods for different clutter area sizes.

Bias			
clutter area	nearest neighbour	inverse distance	tracking
1 pixel	0.16	0.69	0.37
9 pixels	0.64	0.92	0.43
25 pixels	0.80	0.92	0.50

RMSE			
clutter area	nearest neighbour	inverse distance	tracking
1 pixel	0.89	1.82	1.78
9 pixels	1.42	2.32	1.86
25 pixels	1.72	2.53	1.98

of the gauge data which we use for the validation of the radar data.

5.4.4 Attenuation correction

The most common way to correct for attenuation suffered by non-polarimetric radars is by estimating the corrected (unattenuated) rainfall rate R_C from the measured (attenuated) reflectivity Z_A using the equation originally proposed by *Hitschfeld and Bordan* (1954), assuming $Z = aR^b = ck^d$:

$$R_C(r) = \frac{(Z_A(r)/a)^{1/b}}{\left[1 - \frac{2 \ln(10)}{10d} \int_0^r \left(\frac{Z_A(s)}{c}\right)^{1/d} ds\right]^{d/b}}. \quad (5.8)$$

Using this equation the radar image can be corrected for attenuation. A major problem with the Hitschfeld-Bordan equation is the fact that it is numerically unstable, as the denominator in Eq. (8) may get close to zero or even become negative. Setting a constraint on the total correction is therefore necessary. As the radar calibration was uncertain this value was set to 10 dB, as suggested by *Delrieu et al.* (1999). The integral in the denominator goes from 0 to r and, as a result, the equation effectively corrects for the attenuation outwards from the radar. Therefore it is called a forward algorithm. An example is shown in Fig. 5.6b and d. In this figure the amount of correction along the path of the radar beam can be seen. Beyond the strong clutter areas shown in Fig. 5.6a the correction is fairly strong and after clutter removal this effect is greatly reduced.

Another method to correct for attenuation is to use a reference point at a distance r_0 from the radar to calculate the Path Integrated Attenuation (PIA) and from that point use a backward algorithm (*Marzoug and Amayenc*, 1994).

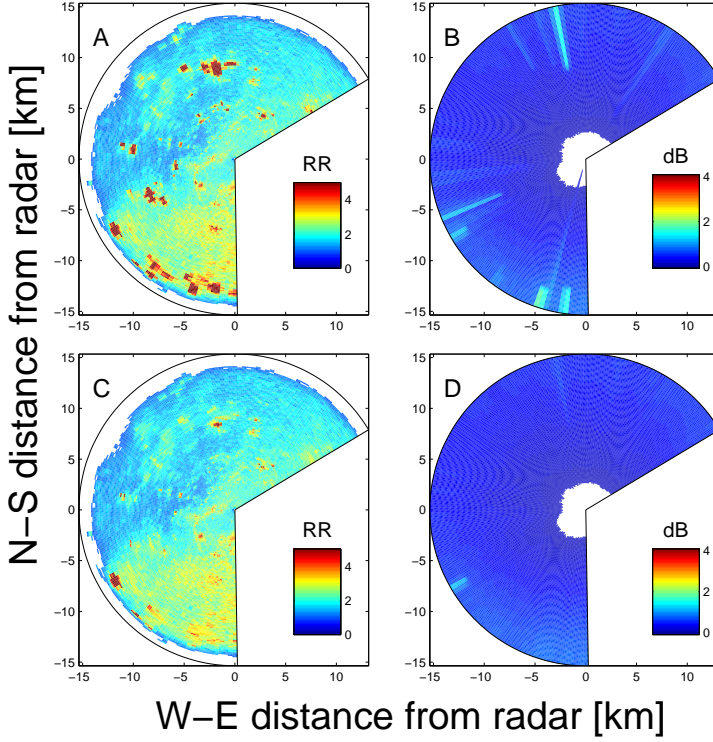


Figure 5.6: Illustration of clutter correction. **a)** shows the image before correction and **b)** the corresponding amount of attenuation correction applied using the Hitschfeld-Bordan forward method (Section 5.4.4). The lower two panels are similar to the upper panels, but with a nearest neighbor clutter correction applied to the image. The clutter area in the southwest that was not removed in this figure is a clutter region that appeared for the first time on 1 October 1993, and remained visible for the remainder of the measurements.

This algorithm has been designed to avoid the instability problem found with the forward algorithm. The equation to derive the corrected rain rate R_C from the measured reflectivity Z_A has a similar functional form as the forward algorithm:

$$R_C(r) = \frac{(Z_A(r)/a)^{1/b}}{\left[A_0^{1/d} + \frac{2 \ln(10)}{10d} \int_r^{r_0} \left(\frac{Z_A(s)}{c} \right)^{1/d} ds \right]^{d/b}} . \quad (5.9)$$

Although the equation basically looks the same as the forward equation, it requires the PIA and the integral goes from the reference range r_0 towards the

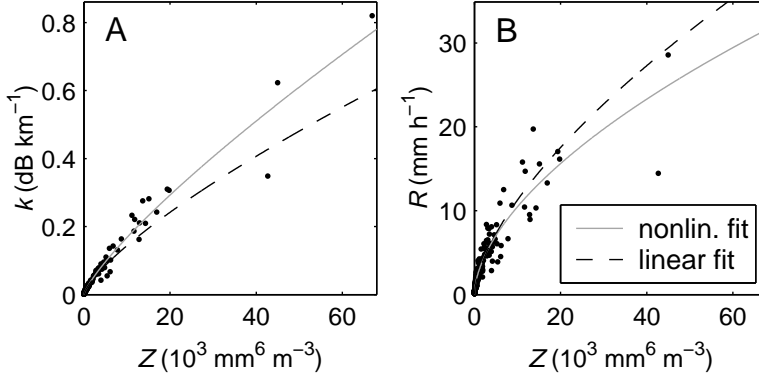


Figure 5.7: (Left) Z - k relation derived from raindrop size distribution data using both a linear and a non-linear power-law fit. (Right) Idem for Z - R relation (from *Leijnse et al.*, 2008).

radar instead of outward from the radar. Here $A_0=A(r_0)$ is the exponential factor in Eq. (2) evaluated at the range $r=r_0$, accounting for the (two-way) PIA between the radar antenna and the reference target. To find this value for a reference point a known clutter area, such as buildings or mountains, can be used but rain gauges as well. In The Netherlands the benefit of a backward algorithm is limited in general, as it is hard to find enough reference points in this mostly flat country. Fortunately, attenuation is generally not a major problem in a climate such as that of The Netherlands, where extreme rain rates over extended areas do not frequently occur. Even if there are not enough reference points to correct the entire image with a backward algorithm, it can be used for verification of the forward algorithm at a limited number of locations.

While both correction algorithms have been found to work fairly well, they have some limitations, mainly associated with the underlying assumptions:

1. The radar is calibrated perfectly.
2. The values of the coefficients and exponents of the Z - R and Z - k relations hold for the entire path over which the correction takes place.
3. The value for A_0 at the reference range employed in the backward algorithm is known accurately.

Due to a lack of reference points for correcting the entire radar image using the backward method, the forward method is used to correct all events in this chapter. To illustrate the accuracy of the backward method compared to the forward method both will be compared in more detail for a few selected events in Section 5.5. While it is not possible to correct the entire radar image it is

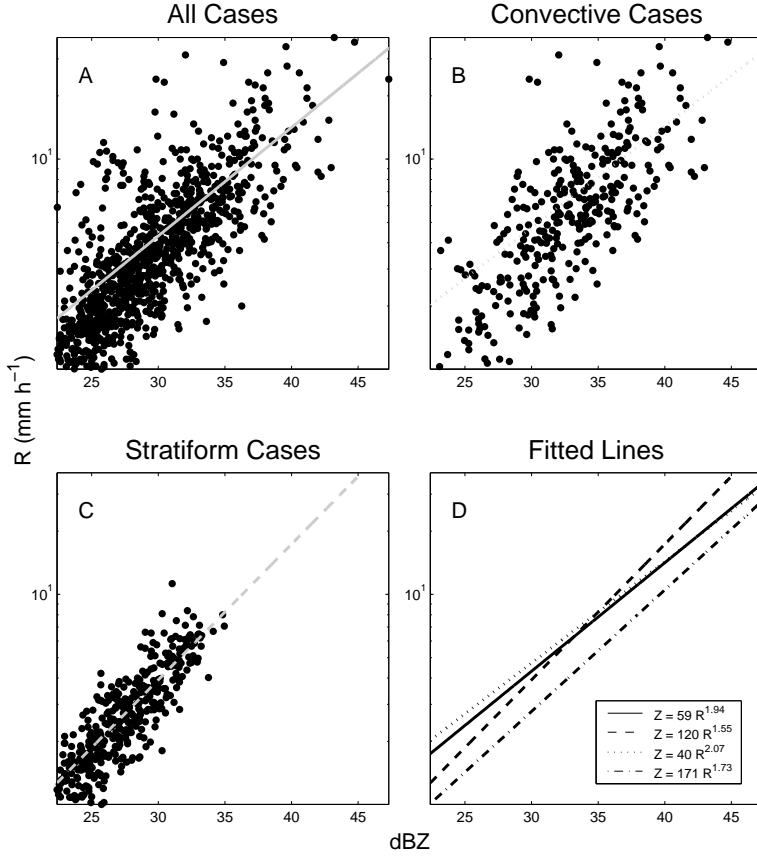


Figure 5.8: Z - R relations derived from nearest gauge data and measured radar reflectivities by applying a non-linear power-law fit. All cases are fitted in **a)**. Convective cases and stratiform cases are plotted in **b)** and **c)**. All fits are plotted together in **d)**, where the solid line indicates the estimated relation through all data, the dotted line the fit through the convective data, the dashed line the fit through the stratiform data and the dash-dotted line the fit through the theoretical data.

possible to use the gauge furthest along the line array as a reference point to estimate the PIA.

The amount of attenuation correction increases with distance from the radar. Figure 5.9 shows the average rain rate for all events as a function of the distance from the radar in the direction of the line array of gauges. As can be seen in Fig. 5.9a the attenuation correction only has a small influence on the average rain rate even after 6 km, where a clutter area is present due to the edge of a greenhouse area. In Fig. 5.9b the clutter has been removed, which results in a slightly reduced average attenuation correction. In Fig. 5.9c

this difference can be seen, where the dashed line indicates the difference of the non-clutter-corrected values and the solid line that of the clutter-corrected ones. At the furthest range this effect becomes around 10% of the inferred rain rate. While these figures do not suggest a huge impact of attenuation correction on average, it actually does have a significant impact on individual strongly convective cases. This will be shown in the case study in Section 5.5, where the correction reaches values of more than 80 mm h^{-1} .

The improvement of attenuation correction over uncorrected values is also illustrated in Fig. 5.10a, which shows the results of our analysis in a scatter plot. Not only does the scatter reduce slightly, but the slope of the linear fit increases from 0.57 to 0.65. As the slight positive offsets of the fitted functions suggest, the radar tends to overestimate for cases with event totals of less than 3 mm. For higher event totals the radar will mostly underestimate. When looking only at the strongly convective as well as the stratiform cases in Fig. 5.10b, results improve in both cases. The fit is closest to the 1:1-line for the convective cases with a slope of 0.77, but has a large amount of scatter. For the stratiform cases the scatter is very small, even though there is still an underestimation for higher rain rates, very similar to that of the fit through all cases. As mentioned before, this underestimation at higher rain rates can be explained partly by wet-radome attenuation and in some cases receiver saturation. As was shown in Section 5.4.3, the employed Z - R relation based on DSD data gives lower estimates than found using the gauge-radar fit. Therefore an underestimation as seen in these figures is not unexpected and suggests that a fit closer to the one found with the radar-gauge data should give better results for this radar. Figure 5.10c is the same plot as Fig. 5.10a, but now using the Z - R relation found from the comparison of the gauges with the reflectivities for all cases. As could be expected, this fit indeed provides a far better agreement between radar and gauge, with a slope of 0.87 for uncorrected and 0.96 for attenuation corrected events. As mentioned in Section 5.4.3, the theoretical fit is used for this study, even though the other gives better results, because the theoretical fit is independent of the gauge data.

5.5 Case studies

In this section five events are studied in greater detail to illustrate both the strengths and challenges of X-band radar, as well as the performance of the correction methods.

5.5.1 Event 1: light precipitation

This event illustrates precipitation observation below the radar threshold of 1 mm h^{-1} . On 15 May 1993, low intensity precipitation passed over or near the gauges in the early morning between 06:00 a.m. and 08:00 a.m. (see Fig. 5.11). From 06:15 a.m. the rain can be seen to move slowly from the southwest and to reach the radar around 06:30 a.m. after which a drop in reflectivity for both

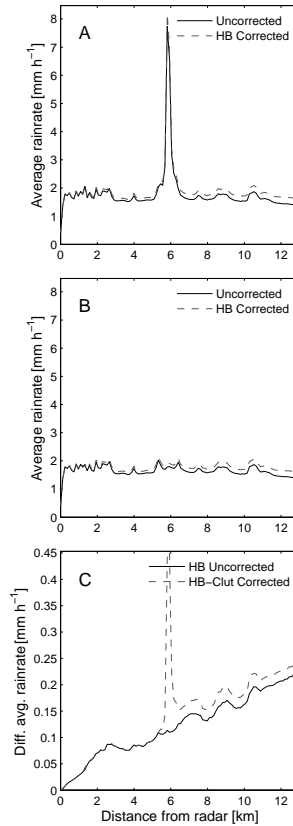


Figure 5.9: Effect of both clutter correction and attenuation correction along the radial in the direction of the line array of rain gauges, averaged over all cases. **a)** Shows the original data uncorrected for both clutter and attenuation (solid line) and only corrected for attenuation (dashed line). **b)** Is the same after correction for clutter, which effectively removes the peak at 6 km from the radar. **c)** Illustrates the difference between the attenuation correction of figures a) and b) and the effect of clutter on the attenuation correction past 6 km.

the major clutter location north of the radar, as well as the total measured reflectivity level of the map is apparent, as shown in Fig. 5.11k and l. This precipitation has a very low intensity of around 0.2 mm h^{-1} , until a small peak of 1 mm h^{-1} is seen at 07:30 a.m. at the gauge at 3.75 km from the radar.

As can be seen in Fig. 5.11a–d this event causes problems for SOLIDAR as this is very near to the minimum detectable reflectivity of 9.05 dBZ (\sim

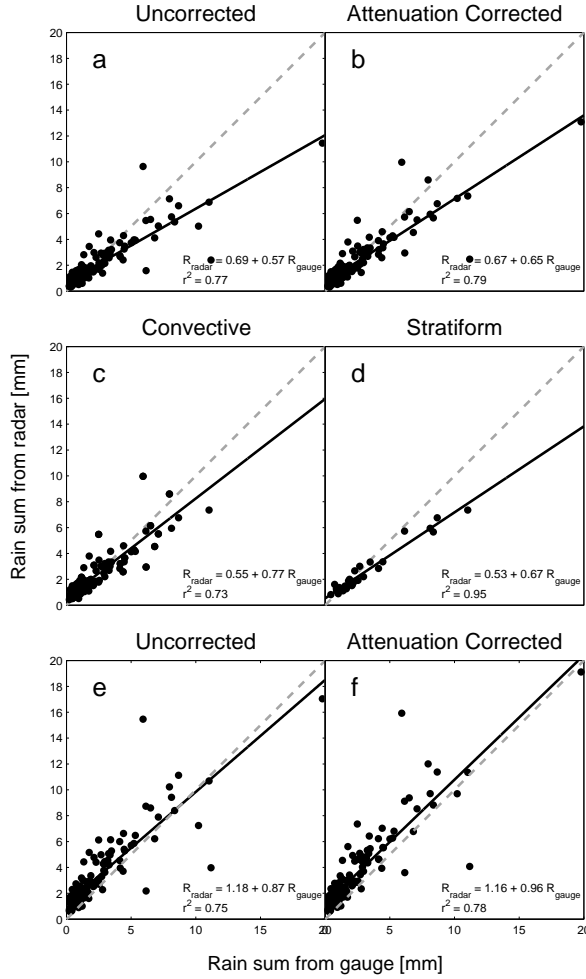


Figure 5.10: Scatter plots of rainfall accumulation from radar and rain gauge for each case. The uncorrected cases using the theoretical Z - R relation are shown in a) and the attenuation-corrected cases in b). Only strongly convective cases are shown in c) and only large-scale stratiform cases in d). e) and f) are the same as a) and b), but now using the Z - R relation found from the gauge-radar comparison for all data.

0.17 mm h^{-1}) and below the radar design minimum of 1 mm h^{-1} rain rates. Combined with the low intensity clutter that is always present in the radar map this makes tracking and quantifying the precipitation very difficult and illustrates the problem of detecting rainfall below 1 mm h^{-1} . As can be seen from the gauge measurements in Fig. 5.11i and j the rain intensity is lower than what would be estimated from the radar. It has to be kept in mind that

only ~ 0.3 mm of rainfall was measured, i.e. just enough for one tipping by the gauge, resulting in only very limited data for comparison.

Table 5.3 shows the results of both the HB-forward and MA-backward attenuation correction schemes. Using the gauge located the furthest away from the radar a PIA estimate is found and from there reflectivities are corrected for attenuation towards the radar. The results in Table 5.3 illustrate that the backward method gives rain rates close to the estimated rain rates of the forward method. This was to be expected as the backward correction scheme only works as long as there is underestimation of the radar compared to the gauge to estimate the attenuation. Where the PIA cannot be estimated the HB-forward scheme is applied. Of course the expected effect of the attenuation correction was very small either way at this low rain intensity. The discrepancy between gauge and radar was to be expected taking into account the lower level of detectable reflectivities and clutter from the radar and the low volumetric resolution of the gauge.

5.5.2 Event 2: stratiform rainfall

During this event on 27 May 1993, which illustrates an underestimation of rainfall by the radar during a stratiform event, rain rates up to 17 mm h^{-1} were measured at the gauge while the radar did not reach values higher than 10 mm h^{-1} . The general appearance of both hyetographs is nevertheless similar, suggesting that the rainfall variability was captured well by SOLIDAR (Fig. 5.12). At 07:00 a.m. the wind and associated precipitation came from the south, which reached the radar itself at 07:40 a.m. By that time the bulk of the precipitation began to move eastwards, even though some lighter precipitation can be seen to keep traveling northward as well. At around 07:50 a.m. the combined precipitation at the radar clearly caused a dip in the measured reflectivity, as shown in Fig. 5.12k and l.

This is a case of high-intensity stratiform rainfall at the radar where, due to wetting of the radar, the signal is more suppressed than is assumed by the HB-forward correction. Even though the shape of the gauge and radar hyetographs look very similar, the significant difference in measured rain intensity even after applying the forward attenuation correction method is a major problem. The results are far more promising when using the backward attenuation correction scheme, as shown in Table 5.4. The rain rate values found using this method are actually very similar to those measured by the gauges. This is an ideal case for a backward attenuation correction scheme as the rain intensity is well above the minimum detection threshold, but not so strong as to completely attenuate the signal, as well as mostly uniform along the path over which the PIA is estimated.

5.5.3 Event 3: convective cells

During this fairly complex event on 16 September 1993, a band of convective cells can be seen to rapidly grow just north and west of the gauge (Fig. 5.14a–d),

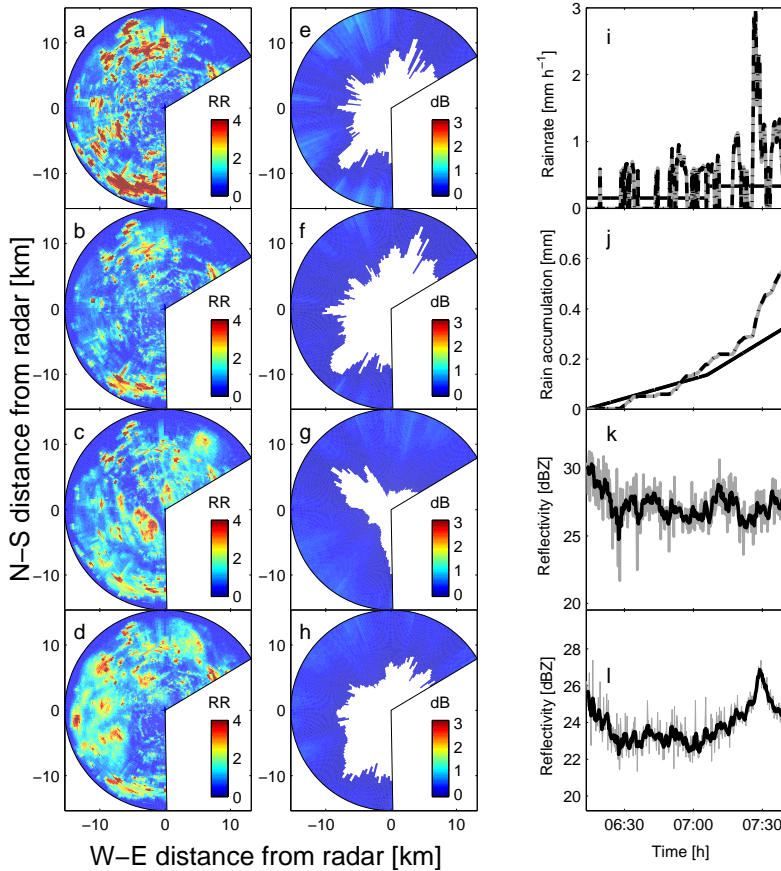


Figure 5.11: Low intensity rain event on 15 May 1993. **a)–d)** Rainfall map from top to bottom: 06:13:27 a.m.; 06:34:15 a.m.; 07:26:32 a.m.; 07:39:50 a.m. **e)–h)** Attenuation correction corresponding to the rainfall maps shown in a)–d). **i)** Rain rate measured by the radar and the gauge at 3.75 km. The black solid line indicates the gauge, the grey solid line the uncorrected radar and the dash-dotted line the HB-forward corrected radar estimate. **j)** same as i), but now accumulated rainfall. **k)** Reflectivity of the clutter area north of the radar, with the instantaneous values in grey and the 1 min moving average in black. **l)** same as k) but with reflectivity for entire image.

while moving slightly westward. This band soon dissolves and soon after several larger convective cells can be seen to form more to the north and south. These cells move in a cyclonal fashion towards the south, with the center of rotation moving from just west of the radar to the radar itself. The first peak can be seen around 11:50 a.m. when a small and short-lived cell grows and dissipates near the gauge at 8 km. Around 01:20 p.m. the center has moved so far from

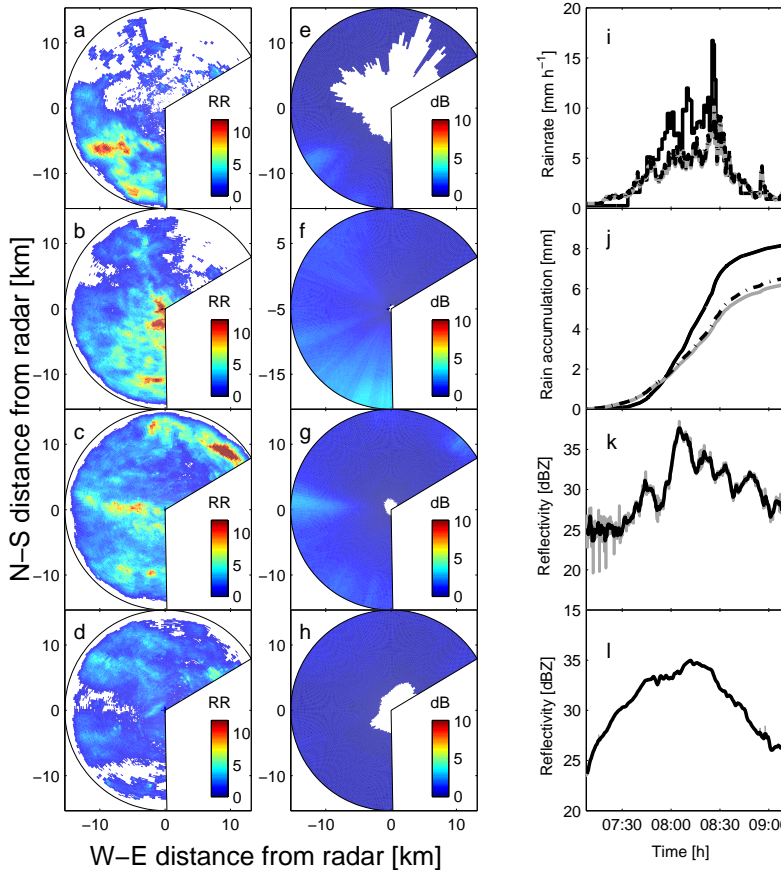


Figure 5.12: Stratiform rain event on 27 May 1993. **a)–d)** Rainfall map from top to bottom: 07:20:35 a.m.; 07:50:05 a.m.; 08:31:06 a.m.; 08:58:30 a.m. **e)–h)** Attenuation correction corresponding to the rainfall maps shown in a)–d). **i)** Rain rate measured by the radar and the gauge at 3.75 km. The black solid line indicates the gauge, the grey solid line the uncorrected radar and the dash-dotted line the HB-forward corrected radar estimate. **j)** same as i), but now accumulated rainfall. **k)** Reflectivity of the clutter area north of the radar, with the instantaneous values in grey and the 1 min moving average in black. **l)** same as k) but with reflectivity for entire image.

the radar that only a westerly wind is visible. At 01:40 p.m. the strongest peak measured at the gauge can be seen when the now fully northwesterly wind brings a somewhat larger convective cell over the gauge.

What makes this case especially interesting is that, while there is a fair amount of precipitation measured in the radar range, the radar itself remains dry for most of the event. As can be seen from Figs. 5.13 and 5.14i and j the

Table 5.3: Rain accumulation [mm] at gauge locations, estimated using different attenuation correction methods, on 15 May 1993.

Distance	Gauge	R_A	R_{HB}	R_{MA}
3750 m	0.3	0.6	0.6	0.6
8006 m	0.4	0.1	0.1	0.1
8006 m	0.4	0.1	0.1	0.1
8864 m	0.3	0.2	0.2	0.2

Table 5.4: Rain accumulation [mm] at gauge locations, estimated using different attenuation correction methods, on 27 May 1993.

Distance	Gauge	R_A	R_{HB}	R_{MA}
3750 m	8.2	6.3	6.6	9.1
8006 m	11.2	6.8	7.9	11.5
8006 m	12.3	6.8	7.9	11.4
8864 m	11.2	6.7	7.9	11.5

hyetograph both at the gauge and that estimated from the radar again have a similar shape, but for the gauge nearest to the radar the center peak is slightly shifted in time compared to the gauge. The accumulated rainfall estimated by the radar at 3.75 km seems reasonable, but still overestimates by 0.5 mm when compared with the gauge. For the gauge at 8 km this is even more pronounced, with nearly twice as much rainfall estimated by the radar.

The significant overestimation is not trivial to explain, but a reason could be found in the fact that in this special case no wet-radome attenuation occurs, as well as highly localized convective cells that may not have been present at the gauge but partially within the radar bin associated with the gauge. As there is overestimation of the radar for nearly the entire event, finding a PIA using the furthest gauge as reference is not possible in most cases. Therefore the MA-backward algorithm also reverts to using the HB-forward scheme and the results for both methods are thus similar (see Table 5.5).

5.5.4 Event 4: weak stratiform precipitation

On 14 October 1993, a 5 h period of stratiform precipitation was measured. In the radar image the precipitation can be seen to come from the southwest in bands of very light precipitation. Around 05:45 a.m. stronger stratiform precipitation can be seen to move in from the northeast, which slowly obscures the precipitation coming from the southwest. Around 07:20 a.m. the precipitation is at its maximum and the only rainfall visible is that from the northeast until at 09:50 a.m. precipitation moving in from the west can be seen (see

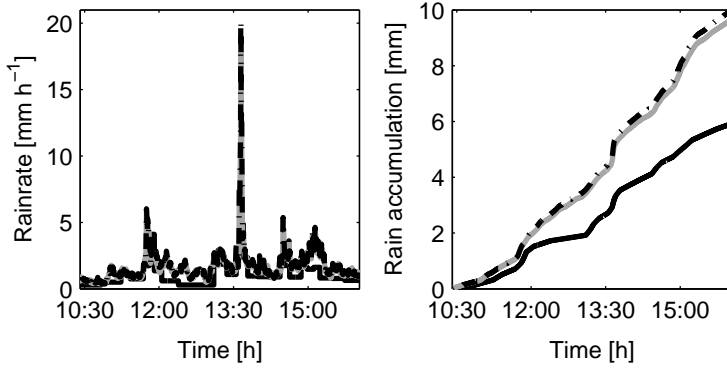


Figure 5.13: Rain rate (left) and rainfall accumulation (right) for an event on 16 September 1993, measured by the radar and the gauge at 8 km. The black solid line indicates the gauge, the grey solid line the uncorrected radar and the dash-dotted line the HB-forward corrected radar estimate.

Table 5.5: Rain accumulation [mm] at gauge locations, estimated using different attenuation correction methods, on 16 September 1993.

Distance	Gauge	R_A	R_{HB}	R_{MA}
3750 m	6.1	6.7	6.7	6.5
5450 m	8.6	12.9	13.4	12.6
8006 m	5.9	9.6	10.0	9.6

Fig. 5.15a–d).

Again the precipitation measured by both gauge and radar follow the same pattern, with the exception of the peak with gauge measurements above 2 mm h^{-1} , which are underestimated by the radar (Fig. 5.15i and j). Like the event of 27 May 1993, the wetting of the radome is the most likely cause of this un-

Table 5.6: Rain accumulation [mm] at gauge locations, estimated using different attenuation correction methods, on 14 October 1993.

Distance	Gauge	R_A	R_{HB}	R_{MA}
3750 m	9.3	7.0	7.1	7.4
5450 m	8.7	8.8	8.9	9.2
8006 m	8.7	6.6	6.8	7.0
8006 m	8.4	6.6	6.8	7.0
8864 m	6.5	7.4	7.6	8.2

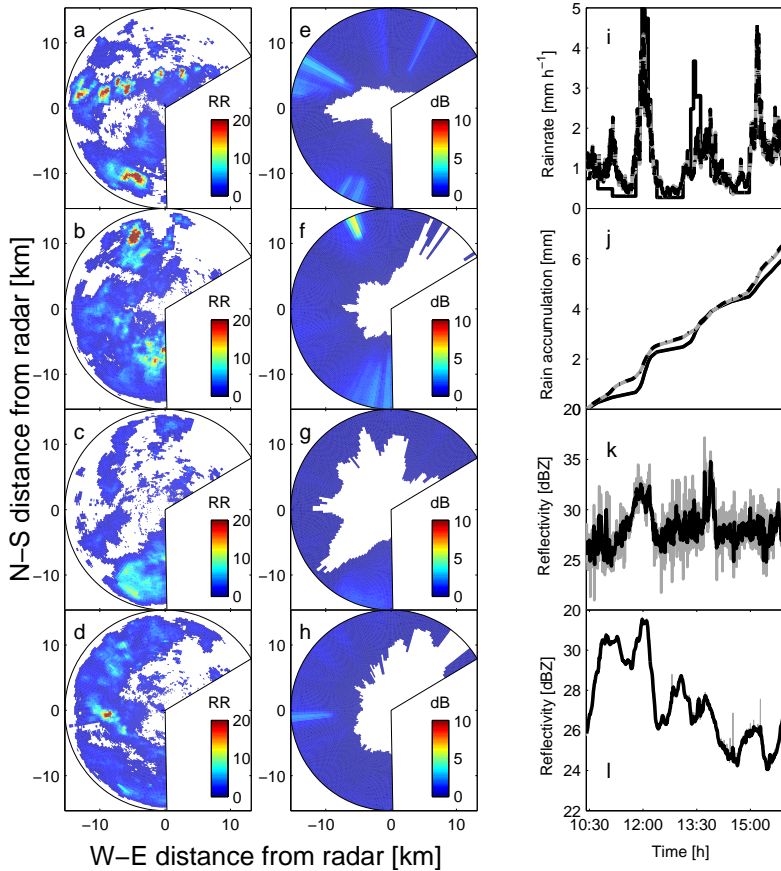


Figure 5.14: Convective rain event on 16 September 1993. **a–d)** Rainfall map from top to bottom: 10:51:04 a.m.; 11:48:04 a.m.; 00:29:15 p.m.; 01:37:49 p.m. **e)–h)** Attenuation correction corresponding to the rainfall maps shown in a)–d). **i)** Rain rate measured by the radar and the gauge at 3.75 km. The black solid line indicates the gauge, the grey solid line the uncorrected radar and the dash-dotted line the HB-forward corrected radar estimate. **j)** same as i), but now accumulated rainfall. **k)** Reflectivity of the clutter area north of the radar, with the instantaneous values in grey and the 1 min moving average in black. **l)** same as k) but with reflectivity for entire image.

derestimation. Indeed, exactly over this period the strongest precipitation is visible over SOLIDAR, even though the intensity of the rainfall is fairly low. The backward correction yields in this case fairly similar results to the forward correction, but lies slightly higher over the entire range. As the radar at some gauges overestimates and at others underestimates there is no clear correction scheme that outperforms the other.

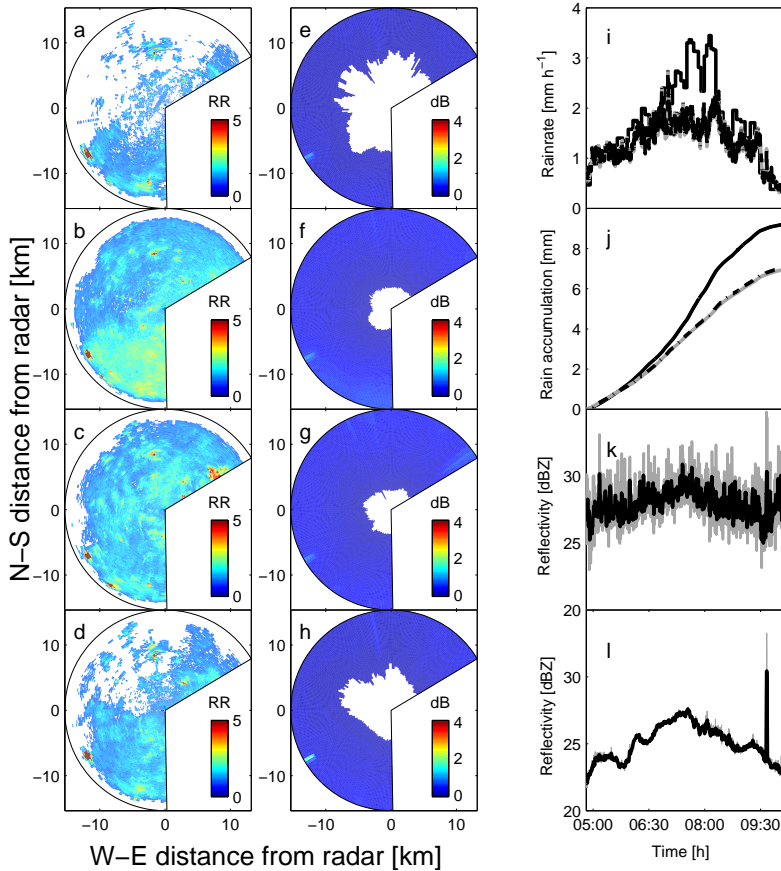


Figure 5.15: Weak stratiform precipitation event on 14 October 1993. **a)–d)** Rainfall map from top to bottom: 04:55:18 a.m.; 06:44:29 a.m.; 08:00:04 a.m.; 09:32:26 a.m. **e)–h)** Attenuation correction corresponding to the rainfall maps shown in (a–d). **i)** Rain rate measured by the radar and the gauge at 3.75 km. The black solid line indicates the gauge, the grey solid line the uncorrected radar and the dash-dotted line the HB-forward corrected radar estimate. **j)** same as i), but now accumulated rainfall. **k)** Reflectivity of the clutter area north of the radar, with the instantaneous values in grey and the 1 min moving average in black. **l)** same as k) but with reflectivity for entire image.

5.5.5 Event 5: squall line

In this event on 21 September, 1993, a strongly precipitating squall line passed over the line array of gauges and the radar, causing major attenuation. The squall line had a west-east orientation and moved from the south over the line array of rain gauges and radar, as can be seen in Figs. 5.16a-d. A rain rate of up

Table 5.7: Rain accumulation [mm] at gauge locations, estimated using different attenuation correction methods, on 21 September 1993.

Distance	Gauge	R_A	R_{HB}	R_{MA}
3750 m	6.0	1.5	3.0	3.8
5450 m	7.4	1.6	2.6	4.0
8006 m	6.2	1.6	3.0	4.0
8006 m	7.5	1.6	3.0	4.0
8864 m	7.8	1.9	3.8	4.8

to 120 mm h^{-1} was measured at the gauge closest to the radar (Fig. 5.16i and j). The rain rate that was measured at this point by SOLIDAR was far less at only 50 mm h^{-1} , which can largely be explained by the strong attenuation along the path, rain on the radar itself or even receiver saturation. After correction for rain-induced attenuation the problem was partly solved, with the maximum rain rate peak estimated from the radar reflectivity even slightly higher than that measured by the gauges. Using the backward correction scheme the estimated rain rate is still too low, although slightly better (see Table 5.7).

The total amount of rain accumulated by the gauges was considerably higher, as the duration of the peak measured by the radar is much shorter. This can be explained by looking at Fig. 5.16e–h, where the strong effect of wet radome attenuation and receiver saturation is clear from the attenuation correction at times 02:58 a.m. and 03:01 a.m. as well as the dip in the clutter reflectivity in Fig. 5.16k and l. In Fig. 5.16k the reflectivity of the clutter area is reduced by nearly 20 dB from the time the squall line is at the radar until it passes over the clutter area. Also the arrival of the strong precipitation at the radar itself is clear from the average reflectivity for the entire radar image, where a drop by an average of 5 dB can be seen. Due to the strong attenuation and possible receiver saturation when the squall line arrives at the radar, nearly the entire signal is lost and the radar does not detect the rain beyond the first few hundred meters anymore. Beyond this range the signal is nearly completely lost, making it impossible even to partially correct for it using an attenuation correction scheme.

Also apparent in such a strong squall line is the fact that the structure of the front of the squall line is well defined before reaching the radar, while after passing over the radar only the structure behind the squall line is visible, with no sharp front visible due to attenuation. To make the structure completely visible the attenuation-corrected image after passing over the radar could be combined with an extrapolated image from before arriving at and attenuating the radar. If the highest value would be selected, the merged image should contain the full dynamic range of the squall-line. This method is limited in scope as the spatial structure of the squall line can quickly change such that extrapolation of only a few images ahead is possible.

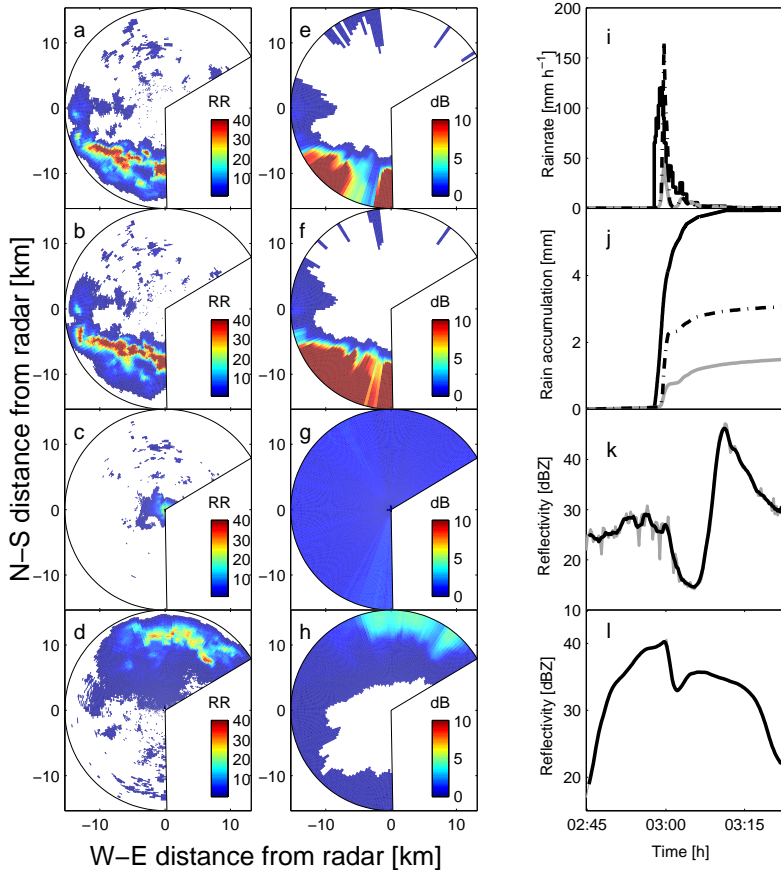


Figure 5.16: Squall line passing over the radar on 21 September 1993. **a)–d)** Rainfall map from top to bottom: 02:52:13 a.m.; 02:58:34 a.m.; 03:01:44 a.m.; 03:15:29 a.m. **e)–h)** Attenuation correction corresponding to the rainfall maps shown in (a–d). **i)** Rain rate measured by the radar and the gauge at 3.75 km. The black solid line indicates the gauge, the grey solid line the uncorrected radar and the dash-dotted line the HB-forward corrected radar estimate. **j)** same as i), but now accumulated rainfall. **k)** Reflectivity of the clutter area north of the radar, with the instantaneous values in grey and the 1 min moving average in black. **l)** same as k) but with reflectivity for entire image.

5.6 Summary and conclusions

We have presented an analysis of 195 rainfall events gathered with the X-band weather radar SOLIDAR and a tipping bucket rain gauge network near Delft, The Netherlands, between May 1993 and April 1994. The high spatial (120 m) and temporal (16 s) resolution of the radar (within a 15 km radius) combined

with the extent of the database make this study a climatological analysis of the potential for high-resolution rainfall measurement with non-polarimetric X-band radar over completely flat terrain.

While clutter and attenuation are generally a problem for X-band weather radars, the correction methods outlined in this article perform fairly well. The identification and removal of clutter using either a nearest neighbor or tracking method gives good results with low bias and root mean square error. For small clutter areas the nearest neighbor methods performs best, but with increasing size the tracking method becomes more accurate.

Some underestimation due to attenuation cannot be filtered out by only applying a Hitschfeld-Bordan forward algorithm, as this algorithm does not account for wet radome attenuation (both in convective and stratiform situations) and considering the 3 assumptions listed in Section 5.4.4. During very strong convective conditions complete signal loss can occur, in which case correction is not possible at all. In addition, a maximum correction constraint has to be set for the forward method to avoid numerical instabilities of the algorithm. Along radials where a reference point is available near the maximum radar range a path-integrated attenuation can be estimated, from which a backward attenuation correction can be performed. This method gives better results in strongly precipitating events as well as in cases where wet radome attenuation plays a role. Unlike the forward method, the backward algorithm is numerically stable.

A correction for wet radome attenuation may be partly achieved by using a clutter area as reference to find the amount of reduction in reflectivity and apply this to the entire image. However, this approach has its problems when rainfall is present on the radar or along the path to the clutter area. In addition, there is a tendency for underestimation of the radar rain rate at higher intensities using the Z - R relation derived from independently collected raindrop size distribution data. Therefore, using a Z - R relation more like that found from the radar-gauge comparison could yield slightly better results.

While some challenges remain to be tackled, this study has revealed that high-resolution X-band radar does offer a wealth of information on both the temporal and spatial structure of precipitation, in far greater detail than rain gauge networks would ever be able to offer. Therefore, such systems have the potential to provide an invaluable tool for (urban) hydrology, especially if combined with a few gauges for quality control of the radar data. We will continue our research concerning X-band radar estimation of the space-time variability of precipitation, in particular using the new high-resolution polarimetric X-band radar IDRA (*Figueras i Ventura and Russchenberg*, 2007, 2008) at the Cabauw Experimental Site for Atmospheric Research (CESAR) in The Netherlands (*Russchenberg et al.*, 2005; *Apituley et al.*, 2008).

CHAPTER 6

Synthesis

The objective of this thesis was to investigate the space-time variability of rainfall in the Netherlands. In Chapter 1 three questions were posed and in this concluding chapter an attempt will be made to answer these.

The three questions posed were:

- Is it possible to predict rainfall variability in the Netherlands, based on limited rain gauge data?
- Can errors in radar measurements of rainfall be reduced to measure precipitation accurately?
- Does high-resolution X-band radar offer additional insight in precipitation over more traditional rain gauge networks and c-band radars?

Section 6.1 goes into detail concerning these questions by providing the conclusions of the previous chapters. Finally in Section 6.2 some ideas are given for future research.

6.1 Conclusion

Chapter 2 studied the spatial variance of rainfall in the Netherlands at daily accumulations using rain gauge data. Using a 30-year dataset of 29 gauges at automatic weather stations and a one-year dataset of 10 rain gauges within a 5 km radius near the center of the Netherlands it was shown that it was possible to find climatological semi-variograms using a simple spherical semi-variogram. The semi-variogram was seen to change depending on the time of year. Because of this, the final results were simple cosine functions describing

the sill and range as well as the RMSE for each day of the year. It should be noted that these variograms represent the average semi-variance at a certain day over the 30-year period. In a given year this may of course be different. The RMSE can give an idea of the associated uncertainty associated with the semi-variance on a certain day.

Chapter 3 built upon the study presented in Chapter 2 by focussing on shorter accumulation intervals (24, 12, 8, 6, 4, 3, 2 and 1 hours). It was found that it was possible to fit a cosine function through the seasonal variation of the sill, range and RMSE at each accumulation interval. This enabled the fitting of a power-law function through each cosine parameter, resulting in a limited set of equations being able to characterize space-time variability of rainfall in the Netherlands for accumulation intervals between 1 and 24 hours as well as up to distances of over 200 km.

Chapter 4 continued the study of precipitation using the C-band radar from KNMI at de Bilt together with rain gauge and disdrometer measurements. It was found that by focussing on a bin near the radar it was possible to reduce errors in path-integrated attenuation and partial beam filling and thereby enabled a better study of wet-radome attenuation and clutter correction. Simple correction schemes based on clutter pixels near the radar made it possible to correct the radar estimate of precipitation partially. Also $Z - R$ relations were derived based on disdrometer measurements and compared to the standard Marshall-Palmer equation and rain gauge measurements. These derived $Z - R$ relations showed another improvement over the standard Marshall-Palmer equation, where the final results closely resembled the measurement by the rain gauge near the range bin studied.

Finally, Chapter 5 focussed on 195 rainfall events measured by a high-resolution X-band radar, SOLIDAR. The radar was compared with a tipping bucket array that was placed along one radar radial. The effectivity of such a high resolution radar in measuring precipitation was tested. Error sources in calibration, clutter and attenuation were reduced. Also a general $Z - R$ relation was derived from radar and gauge comparison as well as for convective and stratiform cases. It was shown that such a radar can be greatly beneficial as it is able to measure precipitation at a very high spatial and temporal resolution. Especially in urban hydrology, where rain gauge networks and operational C-band weather radars do not offer enough resolution, this could be very interesting as it is theoretically possible to retrieve precipitation differences between drainage areas within a city.

The questions posed in Chapter 1 have been tackled in the previous chapters and are discussed shortly below.

- *Is it possible to characterize rainfall variability in the Netherlands, based on limited rain gauge data?*

In Chapter 2 and 3 this question was studied. It was found that for 1 to 24-hour accumulation intervals it is possible to describe the climatological spatial variability of rainfall on a day-to-day basis. While the actual semi-variance at a specific day can vary strongly from this average climatology

the results found in these chapters enables the simulation of random fields and interpolation of rain gauge networks of limited density using kriging.

- *What is the best possible accuracy attainable with radar?*

As was shown in Chapter 4 it is possible to reduce errors due to calibration, clutter and wet-radome attenuation near the radar as long as reference clutter pixels are available. Using disdrometer data it is also possible to derive $Z - R$ relations based on the current drop size distribution. While these correction might have their limits at bins further from the radar it is shown that serious underestimations by the radar can be corrected. The strong underestimation of 54% compared to the rain gauge before correction improved to a small overestimation of only 8% after all corrections had been implemented.

- *Does high-resolution X-band radar offer additional insight in precipitation over more traditional rain gauge networks and operational radars?*

While X-band radar can suffer strongly from path-integrated attenuation it was shown in Chapter 5 that the high temporal and spatial resolution of the radar gives valuable information on the distribution of precipitation. Details in precipitation fields that cannot be identified with a gauge network or even with operational C-band weather radars were observed, showing the potential of X-band radar in (urban) hydrology and water management.

6.2 Discussion and recommendations

While the results presented in the previous chapters gave new insight into the strengths and weaknesses of rain gauges and radars some additional research to follow up these studies is recommended.

- *Chapters 2 & 3*

Problem: The semi-variance found in Chapters 2 and 3 was not applied to intervals shorter than one hour or longer 24-hours. While extrapolation of the derived equations might be valid this has not been tested. As the error in the nugget of the semi-variogram becomes more significant for shorter temporal accumulations it is unlikely the method would work for periods shorter than 1 hour. Additionally, the data set was fairly limited as only 29 gauges from automatic stations were considered for the Netherlands.

Solution: Using data from a dense gauge network with a high temporal resolution might offer the needed insight in how much the effect of the error in the measurements increases for accumulation intervals shorter than one hour. Also accumulating the data to periods longer than 24 hours would be relevant and is therefore recommended. This should be statistically relatively easy to perform.

Problem: The data were also assumed to be homogeneous in all directions (isotropy). While The Netherlands is a fairly flat country, there are regional differences.

Solution: Having a larger and more detailed data set, for example by including Belgium and Germany, might enable the study of the heterogeneity and anisotropy. This would most likely result in directional semi-variograms where the uncertainty beyond 200 km would also decrease.

- *Chapter 4*

Problem: Even though the results found in Chapter 4 are promising for correcting radar data, the study was limited. Only a pixel near the radar was studied and corrections based on average reflectivity and for wet-radome attenuation might not apply at larger distances.

Solution: Studying pixels at greater distance from the radar could prove additional insight even though effects of path-integrated attenuation and partial beam filling would become more pronounced.

Problem: Using a clutter pixel to correct for wet-radome attenuation gave good results, but its applicability in all directions of the radar is limited as wet-radome attenuation is strongly dependent on the wind direction.

Solution: A radar that has several pronounced clutter pixels near the antenna in different directions should be considered. The effect of wind and precipitation type on wet-radome attenuation might then be tested thoroughly. If more knowledge of wind effects for wet-radome attenuation were gained, Doppler or local wind-speed measurements might be used to correct for wet-radome attenuation in all directions even in the case of a single clutter pixel near the radar.

- *Chapter 5*

Problem: The X-band radar, SOLIDAR, studied in Chapter 5 showed great detail in both the spatial and temporal distribution of precipitation. As the dataset was old and calibration details were missing the data was lacking in quality and required much work to be useable.

Solution: It would be very interesting to look at data from its successor, IDRA. With its dual-pol properties an even greater understanding of precipitation might be found, especially as it is located close to the C-band radar at De Bilt and is placed at the measurement site CESAR. This allows comparison with many other instruments. As the site is well maintained the data set will grow over time and would allow the study of more events than were presented in Chapter 5.

Bibliography

- Andrieu, H., G. Delrieu, and J.-D. Creutin (1995), Identification of vertical profiles of radar reflectivity for hydrological applications using an inverse method. Part 2: Sensitivity analysis and case study, *J. Appl. Meteorol.*, *34*, 240–259.
- Andrieu, H., J.-D. Creutin, and D. Faure (1997), Use of a weather radar for the hydrology of a mountainous area. Part I: Radar measurement interpretation, *J. Hydrol.*, *193*, 1–25.
- Aoyagi, J. (1983), A study on the mti weather radar system for rejecting ground clutter, *Papers in Meteor. and Geophy.*, *33*, 187–243.
- Apituley, A., H. W. J. Russchenberg, H. van der Marel, F. Bosveld, R. Boers, H. ten Brink, G. de Leeuw, R. Uijlenhoet, B. Arbesser-Rastburg, and T. Röckmann (2008), Overview of research and networking with ground-based remote sensing for atmospheric profiling at the Cabauw Experimental Site for Atmospheric Research (CESAR) - The Netherlands, *IEEE Geoscience and Remote Sensing Symposium, IGARSS*, pp. 903–906.
- Arias-Hidalgo, M., B. Bhattacharya, A. E. Mynett, and A. van Griensven (2012), Experiences in using the TRMM data to complement rain gauge data in the Ecuadorian coastal foothills, *Hydrol. Earth Sys. Sci.*, *9*(11), 12,435–12,461, doi:10.5194/hessd-9-12435-2012.
- Arnaud, P., C. Bouvier, L. Cisner, and R. Dominguez (2002), Influence of rainfall spatial variability on flood prediction., *J. Hydrol.*, *260*, 216–230.
- Aronica, G., G. Freni, and E. Oliveri (2005), Uncertainty analysis of the influence of rainfall time resolution in the modeling of urban drainage systems, *Hydrol. Process.*, *19*, 1055–1071.
- Atlas, D. (2002), Radar calibration - some simple approaches, *Bull. Am. Meteorol. Soc.*, *83*, 1312–1316.
- Atlas, D., and H. Banks (1951), The interpretation of microwave reflections from rainfall, *J. Meteorol.*, *8*, 271–282.

- Austin, P. M. (1987), Relation between measured radar reflectivity and surface rainfall, *Mon. Weather Rev.*, *115*, 1053–1070.
- Battan, L. J. (1973), *Radar Observation of the Atmosphere*, University of Chicago Press, 324 pp.
- Beard, K. V. (1976), Terminal velocity and shape of cloud and precipitation drops aloft, *J. Atmos. Sci.*, *33*, 851–864.
- Beekhuis, H., and I. Holleman (2008), From pulse to product, highlights of the digital-IF upgrade of the Dutch national radar network, Proceedings of the 5th European Conference on Radar in Meteorology and Hydrology, Helsinki, Finland.
- van de Beek, C. Z., H. Leijnse, J. N. M. Stricker, R. Uijlenhoet, and H. W. J. Russchenberg (2010), Performance of high-resolution X-band radar for rainfall measurement in The Netherlands, *Hydrol. Earth Sys. Sci.*, *14*, 1–17.
- van de Beek, C. Z., H. Leijnse, P. J. J. F. Torfs, and R. Uijlenhoet (2011a), Climatology of daily rainfall semivariance in The Netherlands, *Hydrol. Earth Sys. Sci.*, *15*, 171–183.
- van de Beek, C. Z., H. Leijnse, P. J. J. F. Torfs, and R. Uijlenhoet (2011b), Seasonal semi-variance of Dutch rainfall at hourly to daily scales, *Adv. Water Resour.*, *15*, 171–183.
- Bell, V. A., and R. J. Moore (2000), The sensitivity of catchment runoff models to rainfall data at different spatial scales, *Hydrol. Earth Sys. Sci.*, *4*, 653–667.
- Berenguer, M., D. Sempere Torres, C. Corral, and R. Sánchez-Diezma (2005a), A fuzzy logic technique for identifying non-precipitating echoes in radar scans, *J. Atmos. Oceanic Technol.*, *23*, 1157–1180.
- Berenguer, M., D. Sempere Torres, C. Corral, and R. Sánchez-Diezma (2005b), A fuzzy logic technique for identifying non-precipitating echoes in radar scans, *J. Atmos. Oceanic Technol.*, *23*, 1157–1180.
- Berne, A., and R. Uijlenhoet (2005a), A stochastic model of range profiles of raindrop size distributions: Application to radar attenuation correction, *Geophys. Res. Lett.*, *32*(10), doi:10.1029/2004GL021899.
- Berne, A., and R. Uijlenhoet (2005b), A stochastic model of range profiles of raindrop size distributions: application to radar attenuation correction, *Geophys. Res. Lett.*, *32*(10), L10803, doi:10.1029/2004GL021899.
- Berne, A., and R. Uijlenhoet (2006), Quantitative analysis of X-band weather radar attenuation correction accuracy, *Nat. Hazards Earth Syst. Sci.*, *6*, 419–425.
- Berne, A., G. Delrieu, H. Andrieu, and J.-D. Creutin (2004a), Influence of the vertical profile of reflectivity on radar-estimated rain rates at short time steps, *J. Hydrometeorol.*, *5*(2), 296–310.
- Berne, A., G. Delrieu, J.-D. Creutin, and C. Obled (2004b), Temporal and spatial resolution of rainfall measurements required for urban hydrology, *J. Hydrol.*, *299*, 166–179.
- Berne, A., G. Delrieu, J.-D. Creutin, and C. Obled (2004c), Temporal and

- spatial resolution of rainfall measurements required for urban hydrology, *J. Hydrol.*, 299, 166–179.
- Bidwell, S. W., J. F. Durning, D. F. Everett, M. R. Schwaller, E. A. Smith, and D. B. Wolff (2004), Preparations for Global Precipitation Measurement (GPM) ground validation, *Proceedings of Geoscience and Remote Sensing Symposium, 2004. IGARSS '04*, 2, 921–924.
- Brauer, C. C., A. J. Teuling, A. Overeem, Y. van der Velde, P. Hazenberg, P. M. M. Warmerdam, and R. Uijlenhoet (2011), Anatomy of extraordinary rainfall and flash flood in a Dutch lowland catchment, *Hydrol. Earth Sys. Sci.*, 15, 1991–2005, doi:10.5194/hess-15-1991-2011.
- Bringi, V. N., and V. Chandrasekar (2001), *Polarimetric Doppler Weather Radar: Principles and Applications*, Cambridge University Press.
- Buishand, T. A. (1977), Stochastic modelling of daily rainfall sequences, Ph.D. thesis, Wageningen University.
- Buishand, T. A., and C. A. Velds (1980), Klimaat van Nederland 1: Neerslag en Verdamping, *Tech. rep.*, Royal Netherlands Meteorological Institute, in Dutch.
- Buishand, T. A., L. de Haan, and C. Zhou (2008), On spatial extremes: With application to a rainfall problem, *Ann. Appl. Stat.*, 2(2), 624–642, doi:10.1214/08-AOAS159.
- Buishand, T. A., R. Jilderda, and J. B. Wijngaard (2009), Regionale verschillen in extreme neerslag, *Tech. rep.*, Royal Netherlands Meteorological Institute, in Dutch.
- Calder, I. R., and C. H. R. Kidd (1978), A note on the dynamic calibration of the tipping-bucket gauges, *J. Hydrol.*, 39(3-4), 383–386, doi:10.1016/0022-1694(78)90013-6.
- Chadwick, R. S., D. I. F. Grimes, R. W. Saunders, P. N. Francis, and T. A. Blackmore (2010), The TAMORA algorithm: satellite rainfall estimates over West Africa using multi-spectral SEVIRI data, *Adv. Geosci.*, 25, 3–9, doi: 10.5194/adgeo-25-3-2010.
- Chandrasekar, V., and S. Lim (2008), Retrieval of reflectivity in a networked radar environment, *J. Atmos. Oceanic Technol.*, 25, 1755–1767.
- Chaubey, I., C. T. Haan, S. Grunwald, and J. M. Salisbury (1999), Uncertainty in the model parameters due to spatial variability of rainfall, *J. Hydrol.*, 220, 48–61.
- Cheng, K.-S., Y.-C. Lin, and J.-J. Liou (2008), Rain-gauge network evaluation and augmentation using geostatistics, *Hydrol. Process.*, 22, 2554–2564.
- Ciach, G. J. (2003), Local random errors in tipping-bucket rain gauge measurements, *J. Atmos. Oceanic Technol.*, 20(5), 752–759.
- Ciach, G. J., and W. F. Krajewski (2006), Analysis and modeling of spatial correlation structure of small-scale rainfall in Central Oklahoma, *Adv. Water Resour.*, 29, 1450–1463.

- Cressie, N. A. (1993), *Statistics for spatial data*, revised ed., 900 pp., Wiley, NY.
- Creutin, J.-D., G. Delrieu, and T. Lebel (1986), Rain measurement by raingauge-radar combination: a geostatistical approach, *J. Atmos. Oceanic Technol.*, *5*, 102–115.
- Creutin, J.-D., H. Andrieu, and D. Faure (1997), Use of a weather radar for the hydrology of a mountainous area. Part II: Radar measurement validation, *J. Hydrol.*, *193*, 26–44.
- Daly, C., W. P. Gibson, G. H. Taylor, M. K. Dogget, and J. I. Smith (2007), Observer bias in daily precipitation measurements at United States cooperative network stations, *Bull. Am. Meteorol. Soc.*, pp. 899–912, doi:10.1175/BAMS-88-6-899.
- Delrieu, G., S. Caoudal, and J.-D. Creutin (1997), Feasibility of using mountain return for the correction of ground-based X-band weather radar, *J. Atmos. Oceanic Technol.*, *14*, 368–385.
- Delrieu, G., L. Huc, and J.-D. Creutin (1999), Attenuation in rain for X- and C-band weather radar systems: sensitivity with respect to the drop size distribution, *J. Appl. Meteorol.*, *38*(1), 57–68, doi:10.1175/1520-0450.
- Delrieu, G., B. Boudevillain, J. Nicol, B. Chapon, P. E. Kirstetter, H. Andrieu, and D. Faure (2009), Bollène-2002 experiment: Radar quantitative precipitation estimation in the Cévennes-Vivarais region (France), *J. Appl. Meteorol. Clim.*, *48*, 1422–1447, doi:10.1175/2008JAMC1987.1.
- Diggle, P. J., and P. J. Ribeiro Jr. (2007), *Model-based geostatistics*, 228 pp., Springer, NY.
- Ensor, L. A., and M. R. Scott (2008), Statistical characteristics of daily precipitation: comparison of gridded and point datasets, *J. Appl. Meteorol. Clim.*, *47*, 2468–2476, doi: 10.1175/2008JAMC1757.1.
- Fabry, F., G. Austin, and D. Tees (1992), The accuracy of rainfall estimates by radar as a function of range, *Q. J. R. Meteorol. Soc.*, *118*, 435–453.
- Figueras i Ventura, J., and H. W. J. Russchenberg (2007), Idra: A new instrument for drizzle monitoring, *IEEE Geoscience and Remote Sensing Symposium, IGARSS*, pp. 3301–3304, doi:10.1109/igarss.2007.4423 550.
- Figueras i Ventura, J., and H. W. J. Russchenberg (2008), Idra, a high resolution meteorological radar, *5th European Conference on Meteorology and Radar, ERAD*.
- Figueras i Ventura, J., and H. W. J. Russchenberg (2009), Towards a better understanding of the impact of anthropogenic aerosols in the hydrological cycle: IDRA, IRCR drizzle radar, *Phys. Chem. Earth*, *34*, 88–92.
- Fulton, R., J. Breidenbach, D.-J. Seo, D. Miller, and T. O'Bannon (1998), The WSR-88D rainfall algorithm, *Weather and Forecasting*, *13*, 377–395.
- Gage, K. S., C. R. Williams, P. E. Johnston, W. L. Ecklund, R. Cifelli, A. Tokay, and D. A. Carter (2000), Doppler radar profilers as calibration tools for scanner radars, *J. Appl. Meteorol.*, *39*(12), 2209–2222.

- Germann, U. (1999), Radome attenuation—a serious limiting factor for quantitative radar measurements?, *Meteorol. Z.*, 8, 85–90.
- Gorgucci, E., G. Scarchilli, and V. Chandrasekar (1992), Calibration of radars using polarimetric techniques, *IEEE Trans. Geosci. Remote Sens.*, 30(5), 853–858.
- Gosset, M., and I. Zawadzki (2001), Effect of nonuniform beam filling on the propagation of the radar signal at X-band frequencies. Part I: Changes in the $k(Z)$ relationship, *J. Atmos. Oceanic Technol.*, 18(7), 1113–1126.
- Guillot, G., and T. Lebel (1999), Approximation of sahelian rainfall fields with meta-gaussian random functions - Part 2: parameters estimation and comparison to data, *Stoch. Env. Res. Risk Assess.*, 13, 113–130.
- Haberlandt, U. (2007), Geostatistical interpolation of hourly precipitation from rain gauges and radar for a large-scale extreme rainfall event, *J. Hydrol.*, 332(1-2), 144–157, doi:10.1016/j.jhydrol.2006.06.028.
- Habib, E., W. F. Krajewski, and A. Kruger (2001), Sampling errors of tipping bucket rain gauge measurements, *J. Hydrol. Eng.*, 6(2), 159–166, doi:10.1061/(ASCE)1084-0699(2001)6:2(159).
- Habib, E., F. L. Boone, and J. Grachel (2009), Validation of NEXRAD multisensor precipitation estimates using an experimental dense rain gauge network in South Louisiana, *J. Hydrol.*, 373, 463–478.
- de Haij, M., and W. F. Wauben (2010), Investigations into the improvement of automated precipitation type observations at KNMI, in *Proceedings of the WMO Technical Conference on Meteorological and Environmental Instruments and Methods of Observation*, p. Paper 3(2), Helsinki, Finland.
- Hartwig, F., and B. E. Dearing (1979), *Exploratory data analysis*, 88 pp., Sage Publications, Newberry Park, CA.
- Hazenbergh, P., H. Leijnse, and R. Uijlenhoet (2011a), Radar rainfall estimation of stratiform winter precipitation in the Belgian Ardennes, *Water Resour. Res.*, 47, 1–15.
- Hazenbergh, P., N. Ya, B. Boudevillain, and R. Uijlenhoet (2011b), Scaling of raindrop size distributions and classification of radar reflectivity-rain rate relations in intense Mediterranean precipitation, *J. Hydrol.*, 402, 179–192.
- Heijnen, S. H., L. P. Ligthart, and H. W. J. Russchenberg (2000), First measurements with tara: An s-band transportable atmospheric radar, *Phys. Chem. Earth*, 25, 995–998.
- Hitschfeld, W., and J. Bordan (1954), Errors inherent in the radar measurement of rainfall at attenuating wavelengths, *J. Meteorol.*, 11, 58–67.
- Holleman, I., and H. Beekhuis (2004), Weather radar monitoring using the sun, Technical Report, KNMI TR-272, 2004.
- Holleman, I., and H. Beekhuis (2005), Review of the KNMI clutter removal scheme, Technical Report, KNMI TR-284, 2005.
- Hubbert, J. C., M. Dixon, and S. M. Ellis (2009), Weather radar ground clutter.

- Part II: Real-time identification and filtering, *J. Atmos. Oceanic Technol.*, *26*, 1182–1197.
- Huffman, G. J., D. T. Bolvin, E. J. Nelkin, and D. B. Wolff (2007), The TRMM multisatellite precipitation analysis (TMPA): Quasi-global, multi-year, combined-sensor precipitation estimates at fine scales, *J. Hydrometeorol.*, *8*, 38–55.
- van de Hulst, H. C. (1957), *Light Scattering by Small Particles*, John Wiley & Sons, Inc., 470 pp.
- Humphrey, K. D., J. D. Istok, J. Y. Lee, J. A. Hevesi, and A. L. Flint (1997), A new method for automated dynamic calibration of tipping-bucket rain gauges, *J. Atmos. Oceanic Technol.*, *14*(6), 1513–1519, doi:10.1175/1520-0426.
- Iguchi, T., T. Kozu, R. Meneghini, J. Awaka, and K. Okamoto (2000), Rain-profiling algorithm for the TRMM precipitation radar, *J. Appl. Meteorol.*, *39*, 2038–2052.
- Joss, J., and R. Lee (1995), The application of radar-gauge comparisons to operational precipitating profile corrections, *J. Appl. Meteorol.*, *34*, 2612–2630.
- Joss, J., and A. Waldvogel (1969), Raindrop size distribution and sampling size errors, *J. Atmos. Sci.*, *26*, 566–569.
- Joss, J., and A. Waldvogel (1977), Comments on “some observations on the Joss-Waldvogel rainfall disdrometer”, *J. Appl. Meteorol.*, *16*(1), 112–113.
- Kirstetter, P. E., G. Delrieu, B. Boudevillain, and C. Obled (2010), Toward an error model for radar quantitative precipitation estimation in the Cévennes-Vivarais region, France, *J. Hydrol.*, *394*, 28–41, doi:10.1016/j.jhydrol.2010.01.009.
- Klaasen, W. (1989), Determination of rain intensity from Doppler spectra of vertically scanning radar, *J. Atmos. Oceanic Technol.*, *6*(4), 552–562.
- Knox, R., and E. N. Anagnostou (2009), Scale interactions in radar rainfall estimation uncertainty, *J. Hydrol. Eng.*, *9*, 944–953.
- Kobayashi, S., and T. Iguchi (2003), Variable pulse repetition frequency for the global precipitation measurement project (GPM), *IEEE Transactions on Geoscience and Remote Sensing*, *41*, 1714–1718.
- Krajewski, W. F. (1987), Co-kriging of radar and rain gage data, *J. Geophys. Res.*, *92D8*, 9571–9580.
- Krajewski, W. F., and J. A. Smith (2002), Radar hydrology: rainfall estimation, *Adv. Water Resour.*, *25*(8-12), 1387–1394, doi:10.1016/S0309-1708(02)00062-3.
- Krajewski, W. F., G. J. Ciach, J. R. McCollum, and C. Bacotiu (2000), Initial validation of the global precipitation climatology project monthly rainfall over the United States, *J. Appl. Meteorol.*, *39*, 1071–1086.
- Kuhnlein, M., B. Thies, T. Nauss, and J. Bendix (2010), Rainfall-rate assignment using MSG SEVIRI data—A promising approach to spaceborne rainfall-

- rate retrieval for midlatitudes, *J. Appl. Meteorol. Clim.*, *49*, 1477–1495, doi: <http://dx.doi.org/10.1175/2010JAMC2284.1>.
- Kurri, M., and A. Huuskonen (2008), Measurements of the transmission loss of a radome at different rain intensities, *J. Atmos. Oceanic Technol.*, *25*, 1590–1599.
- Lebel, T., G. Bastin, and J. D. Obled, C. Creutin (1987), On the accuracy of areal rainfall estimation: a case study, *Water Resour. Res.*, *23*(11), 2123–2134.
- Leijnse, H. (2007), Hydrometeorological application of microwave links : measurement of evaporation and precipitation, Ph.D. thesis, Wageningen University.
- Leijnse, H., R. Uijlenhoet, and J. N. M. Stricker (2007a), Rainfall measurement using radio links from cellular communication networks, *Water Resour. Res.*, *43*, W03,201, doi:10.1029/2006WR005631.
- Leijnse, H., R. Uijlenhoet, and J. N. M. Stricker (2007b), Hydrometeorological application of a microwave link: 2. Precipitation, *Water Resour. Res.*, *43*, W04,417, doi:10.1029/2006WR004989.
- Leijnse, H., R. Uijlenhoet, and J. N. M. Stricker (2008), Microwave link rainfall estimation: Effects of link length and frequency, temporal sampling, power resolution, and wet antenna attenuation, *Adv. Water Resour.*, *31*(11), 1481–1493, doi:10.1016/j.advwatres.2008.03.004.
- Leijnse, H., R. Uijlenhoet, C. Z. van de Beek, A. Overeem, T. Otto, C. M. H. Unal, Y. Dufournet, H. W. J. Russchenberg, J. Figueras i Ventura, H. Klein Baltink, and I. Holleman (2010), Precipitation measurement at CESAR, The Netherlands, *J. Hydrometeorol.*, *11*, 1322–1329, doi:10.1175/2010JHM1245.1.
- Li, B., M. Eriksson, R. Srinivasan, and M. Sherman (2008), A geostatistical method for texas NexRad data calibration, *Environmetrics*, *19*, 1–19.
- Ligthart, L. P., and L. R. Nieuwkerk (1990), An X-band solid-state FM-CW weather radar, *IEEE Proc.-F Radar Signal Proces.*, *137*(6), 418–426.
- de Lima, M. I. P. (1998), Multifractals and the temporal structure of rainfall, Ph.D. thesis, Wageningen University.
- Löffler-Mang, M., and J. Joss (2000), An optical disdrometer for measuring size and velocity of hydrometeors, *J. Atmos. Oceanic Technol.*, *17*, 130–139.
- Lovejoy, S., and D. Schertzer (1990), Fractals, raindrops and resolution dependence of rain measurements, *J. Appl. Meteorol.*, *29*(11), 1167–1170.
- Marsalek, J. (1981), Calibration of the tipping-bucket raingage, *J. Hydrol.*, *53*(3-4), 343–354.
- Marshall, J. S., and W. M. Palmer (1948), The distribution of raindrops with size, *J. Meteorol.*, *5*, 165–166.
- Marshall, J. S., W. Hitschfeld, and K. L. S. Gunn (1955), Advances in radar weather, *Adv. Geophys.*, *2*, 1–56.
- Marzoug, M., and P. Amayenc (1994), A class of single- and dual-frequency

- algorithms for rain-rate profiling from a spaceborne radar. Part I: Principle and test from numerical simulations, *J. Atmos. Oceanic Technol.*, 11(6), 1480–1506.
- Meischner, P. (2004), *Weather Radar: Principles and Advanced Applications*, Springer, Berlin.
- Messer, H. A., A. Zinevich, and P. Alpert (2006), Environmental monitoring by wireless communication networks, *Science*, 312, 713.
- Minda, H., and N. Tsuda (2012), Low-cost laser disdrometer with the capability of hydrometeor imaging, *IEEEJ Trans. Elec. Electron Eng.*, 7, S132S138, doi:10.1002/tee.21827.
- Nour, M. H., D. W. Smith, and M. Gamal El-Din (2006), Geostatistical mapping of precipitation: implications for rain gauge network design, *Water Sci. Tech.*, 53(10), 101–110.
- Olsson, J., K. Berggen, M. Olofsson, and M. Viklander (2009), Applying climate model precipitation scenarios for urban hydrological assessment: A case study in Kalmar City, Sweden, *Atmos. Res.*, 92, 364–375.
- Overeem, A. (2009), Climatology of extreme rainfall from rain gauges and weather radar, Ph.D. thesis, Wageningen University.
- Overeem, A., A. Buishand, and I. Holleman (2009), Extreme rainfall analysis and estimation of depth-duration-frequency curves using weather radar, *Water Resour. Res.*, doi:10.1029/2009WR007869.
- Papamichail, D. M., and I. G. Metaxa (1996), Geostatistical analysis of spatial variability of rainfall and optimal design of a rain gauge network, *Water Res. Manag.*, 10, 107–127.
- Roebeling, R. A., and I. Holleman (2009), SEVIRI rainfall retrieval and validation using weather radar observations, *J. Geophys. Res.*, 114, d21202, doi:10.1029/2009JD012102.
- Rose, C. R., and V. Chandrasekar (2006), A GPM dual-frequency retrieval algorithm: DSD profile-optimization method, *J. Atmos. Oceanic Technol.*, 23, 1372–1383, doi: <http://dx.doi.org/10.1175/JTECH1921.1>.
- Russchenberg, H. W. J. (1992), Ground-based remote sensing of precipitation using a multi-polarized FM-CW doppler radar, Ph.D. thesis, Delft University of Technology.
- Russchenberg, H. W. J., F. Bosveld, D. Swart, H. ten Brink, G. de Leeuw, R. Uijlenhoet, B. Arbesser-Rastburg, H. van der Marel, L. Ligthart, R. Boers, and A. Apituley (2005), Groundbased atmospheric remote sensing in The Netherlands: European outlook, in *IEICE Trans. Commun.*, E88-B, pp. 2252–2258, doi:10.1093/ietcom/e88-b.6.2252.
- Ryde, J. W. (1946), *The attenuation and radar echoes produced at centimeter wavelengths by various meteorological phenomena*, in: *Meteorological Factors in Radio Wave Propagation*, 169–188 pp., Physical Society, London.
- Sánchez-Diezma, R., D. Sempere Torres, J.-D. Creutin, I. Zawadzki, and G. Delrieu (2001), Factors affecting the precision of radar measurement of

- rain: Assessment from an hydrological perspective, in *Preprints of the 30th International Conference on Radar Meteorology*, pp. 573–575, American Meteorological Society, Boston.
- Schleiss, M. A., A. Berne, and R. Uijlenhoet (2009), Geostatistical simulation of two-dimensional fields of raindrop size distributions at the meso-gamma scale, *Water Resour. Res.*, *45*, 1–10, doi:10.1029/2008WR007545.
- Schuurmans, J. M. (), Hydrological now- and forecasting, Ph.D. thesis, Utrecht University.
- Schuurmans, J. M., M. F. P. Bierkens, E. J. Pebesma, and R. Uijlenhoet (2007), Automatic prediction of high resolution daily rainfall fields for multiple extents: the potential of operational radar, *J. Hydrometeorol.*, *8*(6), 1204–1224, doi:10.1175/2007JHM792.1.
- Serrar, S., G. Delrieu, J. Creutin, and R. Uijlenhoet (2000), Mountain reference technique: Use of mountain returns to calibrate weather radars operating at attenuating wavelengths, *J. Geophys. Res.*, *105*(D2), 2281–2290, doi:10.1029/1999JD901025.
- Sevruk, B., and V. Nešpor (1998), Empirical and theoretical assessment of the wind induced error of rain measurements, *Water Sci. Tech.*, *37*, 171.
- Sevruk, B., and L. Zahlavova (1994), Classification system of precipitation gauge site exposure: Evaluation and application, *Int. J. Climatol.*, *14*, 681.
- Shumway, R. H., and D. S. Stoffer (2006), *Time series analysis and its applications - with R examples*, 2nd ed., 575 pp., Springer, NY.
- Sieck, L. C., S. J. Burges, and M. Steiner (2007), Challenges in obtaining reliable measurements of point rainfall, *Water Resour. Res.*, *43*, W01420, doi:10.1029/2005WR004519.
- Siggia, A. D., and R. E. Passarelli (2004), Gaussian model adaptive processing (GMAP) for improved ground clutter cancellation and moment calculation, *Proc. ERAD 2004*, *2*, 421–424.
- Simpson, J., R. Adler, and G. North (1988), A proposed Tropical Rainfall Measuring Mission (TRMM), *Bull. Am. Meteorol. Soc.*, *69*, 278–295.
- Smith, J. A., M. L. Baeck, J. E. Morrison, P. Sturdevant-Rees, D. F. Turner-Gillespie, and P. D. Bates (2002), The regional hydrology of extreme floods in an urbanizing drainage basin, *J. Hydrometeorol.*, *3*(3), 267–282.
- Smith, J. A., M. L. Baeck, K. L. Meierdiercks, P. A. Nelson, A. J. Miller, and E. J. Holland (2005), Field studies of the storm event hydrologic response in an urbanizing watershed, *Water Resour. Res.*, *41*, W10413, doi:10.1029/2004WR003712.
- Steiner, M., and J. A. Smith (2002), Use of three-dimensional reflectivity structure for automated detection and removal of non-precipitating echoes in radar data, *J. Atmos. Oceanic Technol.*, *19*, 673–686.
- Stephens, G. L., and C. D. Kummerov (2007), The remote sensing of clouds and precipitation from space, *J. Atmos. Sci.*, *64*, 3742–3765.
- Stratmann, E., D. Atlas, J. H. Richter, and D. R. Jensen (1971), Sensitiv-

- ity calibration of a dual-beam vertically pointing FM-CW radar, *J. Appl. Meteorol.*, *10*, 1260–1265.
- Tetzlaff, D., and S. Uhlenbrook (2005), Significance of spatial variability in precipitation for process-oriented modelling: results from two nested catchments using radar and ground station data, *Hydrol. Earth Sys. Sci.*, *9*, 29–41.
- Thurai, M., and V. N. Bringi (2005), Drop axis ratios from a 2D Video Disdrometer, *J. Atmos. Oceanic Technol.*, *22*, 966–978.
- Tokay, A., P. G. Bashor, and K. R. Wolff (2005), Error characteristics of rainfall measurements by collocated Joss-Waldvogel disdrometers, *J. Atmos. Oceanic Technol.*, *22*, 513–527.
- Uijlenhoet, R. (1999), Parameterization of rainfall microstructure for radar meteorology and hydrology, Ph.D. thesis, Wageningen University.
- Uijlenhoet, R. (2001), Raindrop size distributions and radar reflectivity-rain rate relationships for radar hydrology, *Hydrol. Earth Sys. Sci.*, *5*, 615–627.
- Uijlenhoet, R. (2008), *Precipitation physics and rainfall observation. Chapter 4*, in: *Climate and the Hydrological Cycle* (Marc Bierkens, Peter Troch, and Han Dolman, editors), *IAHS Special Publications 8*, 59–97 pp., IAHS Press, Wallingford.
- Uijlenhoet, R., and A. Berne (2008), Stochastic simulation experiment to assess radar rainfall retrieval uncertainties associated with attenuation and its correction, *Hydrol. Earth Sys. Sci.*, *12*, 587–601.
- Uijlenhoet, R., J. N. M. Stricker, and H. W. J. Russchenberg (1997), Application of X- and S-band radars for rain rate estimation over an urban area, *Phys. Chem. Earth*, *22*, 259–264.
- Uijlenhoet, R., M. Steiner, and J. A. Smith (2003), Variability of raindrop size distributions in a squall line and implications for radar rainfall estimation, *J. Hydrometeorol.*, *4*(1), 43–61.
- Ulbrich, C. W., and L. G. Lee (1999), Rainfall measurement error by WSR-88D radars due to variations in $z - r$ law parameters and the radar constant, *J. Atmos. Oceanic Technol.*, *16*, 1017–1024.
- Unal, C. (2009), Spectral polarimetric radar clutter suppression to enhance atmospheric echoes, *J. Atmos. Oceanic Technol.*, *26*(9), 1781–1797, doi:10.1175/2009JTECHA1170.1).
- Vaes, G., P. Willems, and J. Berlamont (2005), Areal rainfall correction coefficients for small urban catchments, *Atmos. Res.*, *77*, 48–59.
- van Montfort, A. (1966), *Statistische Beschouwingen over Neerslag en Afvoer*, H. Veenman.
- Velasco-Forero, C. A., D. Sempere-Torres, E. F. Cassiraga, and J. J. Gomez-Hernandez (2009), A non-parametric automatic blinding methodology to estimate rainfall fields from rain gauge and radar data, *Adv. Water Resour.*, *32*, 986–1002.
- Vignal, B., G. Galli, J. Joss, and U. Germann (2000), Three methods to deter-

- mine profiles of reflectivity from volumetric radar data to correct precipitation estimates, *J. Appl. Meteorol.*, *39*, 1715–1726.
- Villarini, G., and W. F. Krajewski (2008), Empirically-based modeling of spatial sampling uncertainties associated with rainfall measurements by rain gauges, *Adv. Water Resour.*, *31*(7), 1015–1023, doi:10.1016/j.advwatres.2008.04.007.
- Villarini, G., and W. F. Krajewski (2010), Review of the different sources of uncertainty in single-polarization radar-based estimates of rainfall, *Surv. Geophys.*, *31*, 107–129.
- Villarini, G., P. V. Mandapaka, W. F. Krajewski, and R. J. Moore (2008), Rainfall and sampling uncertainties: a rain gauge perspective, *J. Geophys. Res.*, *113*, D11,102, doi:10.1029/2007JD009214.
- Villarini, G., J. A. Smith, M. L. Baeck, P. Sturdevant-Rees, and W. F. Krajewski (2010), Radar analyses of extreme rainfall and flooding in urban drainage basins, *J. Hydrol.*, *381*, 266–286.
- Wauben, W. (2004), Precipitation amount and intensity measurements using a windscreen, *Tech. Rep. TR-262*, R. Neth. Meteorol. Inst., De Bilt, the Netherlands.
- Wauben, W. (2006), KNMI contribution to the WMO laboratory intercomparison of rainfall intensity gauges, (TR-287).
- Wessels, H. R. A. (1972), Metingen van regendruppels in De Bilt, *Tech. Rep. W. R. 72-6*, R. Neth. Meteorol. Inst., De Bilt, 41 pp. (in Dutch).
- Witter, J. V. (1984), Heterogeneity of Dutch rainfall, Ph.D. thesis, Wageningen University, 204 pp.
- WMO (1996), Guide to meteorological instruments and methods of observation, sixth edition, WMO-No. 8, WMO, Geneva.
- Yuter, S. E., D. Kingsmill, L. B. Nance, and M. Löffler-Mang (2006), Observations of precipitation size and fall speed characteristics within coexisting rain and wet snow, *J. Appl. Meteorol.*, *45*(10), 1450–1464, doi:10.1175/JAM2406.1.
- Zawadzki, I. (1984), Factors affecting the precision of radar measurements of rain, in *Preprints of the 22nd conference on Radar Meteorology*, pp. 251–256, American Meteorological Society, Boston.
- Zimmerman, D. L., and M. B. Zimmerman (1991), A comparison of spatial semivariogram estimators and corresponding ordinary kriging predictors, *Technometrics*, *33*, 77–91.

Curriculum Vitae

Remco van de Beek, 12 January 1978, Vriezenveen, The Netherlands

1990-1996

Secondary School, Visser 't Hoofd Lyceum, Leiden

1998-2004

Ir. Soil, Water, Atmosphere - Specialization Meteorology,
Wageningen University, The Netherlands

MSc. research subjects:

1. Derivation of the radiation and energy balance from NOAA-14 data using Surface Energy Balance ALgorithm (SEBAL)
2. Setting up a verification system for On Screen Field Modification (OSFM) at KNMI
3. Influence of Madagascar on the weather of southern Africa using the Conformal Cubic Atmospheric Model (CCAM)

2004-2009

Doctoral research on Rainfall variability in the Netherlands from radars, rain gauges, and disdrometers,
Hydrology and Quantitative Water Management group,
Wageningen University

2010-2011

Remote sensing specialist and agro-meteorologist,
EARS, Delft, The Netherlands

2012-present

Meteorological researcher,
Meteo Consult, Wageningen, The Netherlands



Netherlands Research School for the
Socio-Economic and Natural Sciences of the Environment

C E R T I F I C A T E

The Netherlands Research School for the
Socio-Economic and Natural Sciences of the Environment
(SENSE), declares that

***Cornelis Zacharja
van de Beek***

born on 12 January 1978 in Vriezenveen, The Netherlands

has successfully fulfilled all requirements of the
Educational Programme of SENSE.

Wageningen, 12 June 2013

the Chairman of the SENSE board

Prof. dr. Rik Leemans

the SENSE Director of Education

Dr. Ad van Dommelen

The SENSE Research School has been accredited by the Royal Netherlands Academy of Arts and Sciences (KNAW)



KONINKLIJKE NEDERLANDSE
AKADEMIE VAN WETENSCHAPPEN



The SENSE Research School declares that **Mr. Cornelis Zacharja van de Beek** has successfully fulfilled all requirements of the Educational PhD Programme of SENSE with a work load of 45 ECTS, including the following activities:

SENSE PhD Courses

- o Environmental Research in Context
- o Research Context Activity: Co-organizing SENSE Summer Symposium 2005: Kyoto and Beyond, Ede, 21 June 2005

Other PhD and Advanced MSc Courses

- o Basic and Advanced Statistics
- o Uncertainty Analysis
- o Climate and the Hydrological Cycle
- o Propagation of Uncertainty in Advanced Meteo-Hydrological Forecast Systems
- o Spatial Statistics
- o Scientific Writing

Oral Presentations

- o *Rainfall estimation using a high-resolution X-band radar*. Klimaat voor Ruimte: Second Workshop "Synergy in climate changes spatial planning research", 16 May 2007, Driebergen, The Netherlands
- o *Climatology of daily rainfall semivariance in The Netherlands*. ERAD 5, 30 June - 4 July 2008, Helsinki, Finland
- o *Seasonal semi-variance of Dutch rainfall at hourly to daily scales*. ERAD 6, 25-29 June 2012, Toulouse, France

SENSE Coordinator PhD Education

Drs. Serge Stalpers

Financial support for this thesis was provided by The Netherlands Organization for Scientific Research (NWO) through grant EO-058